Vanadium Dioxide Nanowires and Thin Films: Applications of the Structural and Electronic Phase Transition

By

Kevin Xia-hui Wang

A dissertation submitted in partial satisfaction of the
requirements for the degree of
Doctor of Philosophy
in
Engineering – Materials Science and Engineering
in the
Graduate Division
of the
University of California, Berkeley

Committee in charge:

Professor Junqiao Wu, Chair
Professor Oscar Dubon
Professor Peter Hosemann

Fall 2016

Vanadium Dioxide Nanowires and Thin Films: Applications of the Structural and Electronic Phase Transition

Abstract

Vanadium Dioxide Nanowires and Thin Films: Applications of the Structural and Electronic Phase Transition

by

Kevin Xia-hui Wang

Doctor of Philosophy in Materials Science and Engineering

University of California, Berkeley

Professor Junqiao Wu, Chair

The simultaneous metal-insulator and structural phase transitions of vanadium dioxide (VO_2) makes this material attractive for a variety of applications. Heating VO_2 above 67 °C, the electronic conductivity increases by a factor of 10^5, and the lattice shrinks along the c-axis by 1%, a very large spontaneous strain. As a strongly correlated electron material, VO_2 is extremely interesting from a condensed matter physics perspective, with ongoing research into the nature of the metal-insulator transition (MIT). Vanadium dioxide began drawing significant interest as early as the 1950s, but studies were often hindered by the tendency of bulk samples to crack upon passage across the phase transition. Recent advances in sample synthesis allow us to study VO_2 nanobeams and thin films, which are extremely high quality and mechanically robust. This dissertation focuses on applications of VO_2 in actuation and sensing, tuning the phase transition behavior by doping, and understanding the behavior of point defects in response to the structural phase change.

First, we develop bimorph actuators with VO_2 nanobeams utilizing the phase transition as solid engine converting heat into motion. Microscale mechanical motion is typically actuated by mechanisms including electrostatic interaction, thermal expansion, and piezoelectricity, as well as more exotic types like shape memory, electrochemical reactions, and thermal responsivity of polymers. These mechanisms typically offer either large-amplitude or high-speed actuation, but not both. We demonstrate a microscale solid engine (μSE) based on the phase transition of VO_2 at 67 °C with large transformation strain (up to 2%), analogous to the steam engine imparting large volume change in a liquid-vapor phase transition. Compared to poly-crystal thin films, single-crystal VO_2 nanobeam-based bimorphs deliver higher performance of actuation both

with high amplitude (> bimorph length) and at high speed (> 4 kHz in air and > 60 Hz in water). The energy efficiency of the devices is calculated to be equivalent to thermoelectrics with figure of merit *ZT* = 2 at the working temperatures, and much higher than other bimorph actuators. The bimorph μSE can be easily scaled down to the nanoscale, and operates with high stability in near-room-temperature, ambient or aqueous conditions. Based on the μSE, we demonstrate a macroscopic smart composite of VO_2 bimorphs embedded in a polymer, producing high-amplitude actuation at the millimeter scale.

To implement this powerful phase-transition actuation technology in a more controllable and reliable manner, we next develop patternable bimorph actuators using VO_2 thin films and photolithography. Existing actuator materials cannot simultatneously deliver high amplitude, work output, and speed, but we show that our microactuators excel in all of these metrics. Our VO_2 bimorph actuators are driven by the structural phase transition structural in response to heat, electric current, or light and bend with exceedingly high displacement-to-length ratios up to 1 in the sub-100 μm length scale, work densities over 0.63 J/cm^3, and at frequencies up to 6 kHz. These devices operate in ambient and aqueous environments, and their microfabrication process enables integrated designs of planar as well as three-dimensional geometries using common process steps for Si-based MEMS. Combining the superior performance, high durability, diversity in responsive stimuli, versatile working environments, and microscale manufacturability, these actuators offer potential applications in micro-electromechanical systems, microfluidics, robotics, drug delivery, and artificial muscles.

Adapting VO_2 to a wider range of applications and environments requires control of the MIT behavior, which can be controlled by doping the material with transition metals. Often, lower operating temperature is desired for achieving the desired functionality with less thermal or other energy input. We study the effect of tungsten doping in VO_2 films, which lowers the MIT temperature by 23 K / % W, but increases the electron concentration and dramatically reduces the carrier mobility in the material. This characterization of the electronic properties will assist future design of electronic devices utilizing doped VO_2. Within nanobeams, we incorporate tungsten with a spatially varying profile to broaden the MIT behavior and increase the range of applications. At room temperature, the graded doped nanowires show metal phase on the tips and insulator phase near the center of the nanowire, and the metal phase grows progressively toward the center when temperature rises. As such, each individual nanowire acts as a micro-thermometer that can be simply read out with an optical microscope. The nanowire resistance decreases gradually with the temperature rise eventually reaching two orders of magnitude drop, in stark contrast to abrupt resistance change in un-doped VO_2 wires. This novel phase transition yields an extremely high temperature coefficient of resistivity ~ 10 %/K, simultaneously with a very low resistivity

down to 0.001 Ω·cm, making them a promising infrared sensing material for un-cooled micro-bolometers. Lastly, they form bimorph thermal actuators that bend with an unusually high curvature, ~900 $m^{-1} \cdot K^{-1}$ over a wide temperature range (35 – 80°C), significantly broadening the responding temperature range of previous VO_2 bimorph actuators.

Finally, we study point defects in VO_2 and their interaction with the structural phase transition. Several potential mechanisms are discussed for enhanced point defect motion in a material undergoing a significant structural distortion (like the 1% expansion VO_2 experiences in the MIT). From this structural viewpoint, strain fields and anelasticity may encourage point defects to migrate near the phase transition boundary, regions of large strain. Additionally, local energy supplied by the domain wall between phases or by the latent heat may also activate point defect motion. We investigate the potential for a MIT-based anneal in VO_2 by introducing point defects into thin films by ion irradiation. By monitoring the crystal quality of the film via Hall effect and RBS channeling, we compare two different anneals: a cyclic anneal (thousands of times across the phase transition) and a conventional single-step anneal, holding the VO_2 film just above the MIT temperature. The results suggest that there is no enhanced point defect motion with the phase change, as the defective thin films recover similarly whether cycled thousands of times across the MIT or held at a constant T above T_C for an equivalent amount of time.

Table of Contents

List of Figures

Acknowledgements

My parents Yi-Xin Wang and Wei Xia led me to where I am today and helped me pursue my dreams here at Berkeley. I cannot thank you enough. Giulia Fanti, thank you for being so smart and caring and helping me get through the toughest of times. Eicke Weber, Tonio Buonassisi, and Ron Gronsky, you were excellent instructors for a 2nd year undergrad and helped sparked my interest in Materials Science.

There have been so many wonderful people at Berkeley who have helped me grow as a scientist throughout the years. I'd like to acknowledge Prof. Kin Man Yu for his guidance and insight at the RBS accelerator. Jeffrey Beeman has been completely critical for keeping LBL's Bldg 2 facilities safe and running smoothly. I had a great time in the classroom of Profs. Daryl Chrzan and Oscar Dubon, not just learning about science but also enjoying their playful personalities. I am grateful they served on my qualifying exam committee, along with Profs. Peter Hosemann and Andrew Minor.

I'd next like to thank all the dedicated, friendly, and sharp scientists in my research group for making the lab and office an enjoyable place: Drs. Jinbo Cao, Joonki Suh, Changhyun Ko, Hwan Sung Choe, Deyi Fu, Alex Luce, Jian Zhou, Alejandro Levander, Ty Matthews, Greg Brown, Devesh Khanal, Joanne Yim, Wen Fan, and Profs. Kai Liu, Sangwook Lee, Chun Cheng, Chenglun Hsin, and Bin Xiang.

Other key members of the Wu Group have been the undergrad researchers working with me. I'm very grateful to Erica Sheu, Zelin Yang, Billy Guan, Jimmy Nguyen, Tu Nguyen, George Li, and Rui Wang (MS student) for their dedication and contribution to science. I especially thank Edy Cardona for his spirit and creativity as an undergrad researcher, and I wish him the best of luck in his PhD studies here at Berkeley. I also appreciate Thomas Chan spending his summer at Berkeley patiently probing nanowires and know he will do great in his ChemE studies at Berkeley.

The rest of the MSE community has been really wonderful too. First, I'd like to thank the MSE office for being really on top of things and helping make sure I'm funded. Catalina Estrada, Wanda Capece, Mei Griebenow, Janene Martinez, Ariana Castro, and Margo MacDonald have been truly professional and a pleasure to work with. I thank Dr. Franklin Wong for being a weird and fun fellow student, but also for helping me better understand oxide bonding. Dr. Rohini Sankaran has been a great friend and source of positivity in trying times. Other students who have helped me grow include Dr. Christopher Bartlow, Dr. Hannah Ray, Dr. Elizabeth Boatman, Dr. Jodi Iwata, Dr. Hua

Guo, and Prof. John Heron. I next want to give a shout-out to the fun students of Prof. Ting Xu's lab, Drs. Kari Thorkelsson, Peter Bai, Nikhil Dube, and Shawn Darnall, for not only being awesome officemates but for being kind and very sharing of their lab resources. I thank Drs. Yifan Jiang and Isaac Markus for being key members of the MSE Graduate Student Council, and helping with department socials and seminars.

From outside the MSE department, I'd like to thank Steven Volkman, Drs. Lakshmi Jagannathan, Donovan Lee, Jake Sadie and Prof. Vivek Subramanian for their guidance during my MS, and for discussions during my PhD. I thank Prof. Ana Arias for the opportunity to serve as GSI for an awesome course on photovoltaics. Prof. Lee Fleming and Dr. Alexandre Beliaev at the Fung Institute were a wonderful team to work with, and I appreciate the opportunity to teach Engineering Leadership for the Masters in Engineering.

Lastly, I greatly thank my advisor, Prof. Junqiao Wu for his scientific insight and support for my curiosity. I have been very fortunate to learn and work with his exceptional understanding of physics, academic rigor and engineering instincts.

Chapter 1

Introduction

Vanadium dioxide (VO_2) is a material with a dramatic metal-insulator transition (MIT) and simultaneous structural phase transition. Heating VO_2 above 67 °C, the electronic conductivity increases by a factor of 10^5, and the lattice shrinks along the c-axis by 1%, a very large spontaneous strain [1,2]. As a strongly correlated electron material, VO_2 is of great interest for fundamental studies in condensed matter physics, and its drastic changes between phases lead to many potential applications, including electronic memory [3], memristor [4], Mott transistor [5], optical switch [6], smart window coating [7], strain sensor [8], gas sensor [9], temperature sensor [10], and thermal actuator [11]. The phase change is primarily triggered thermally, but it is also possible to be activated electrically, optically (via photothermal absorption), and by strain. We explore in depth the design and operation of actuators based on VO_2 nanobeams and thin films, with potential applications in microrobotics, biomedical therapy, and microfluidics. We also investigate the doping of VO_2 with tungsten to lower the MIT temperature and improve device control and functionality, with potential applications in actuation and infrared bolometry. Lastly, we study the interplay between native point defects and the metal-insulator transition, to assess the hypothetical increase in defect mobility through a structural phase change.

1.1 VO_2 Crystal Structure

The primary phases investigated in this work are the monoclinic M1 phase, existing below the transition temperature T_C, ~67 °C and the rutile (tetragonal) phase, existing at high temperature, shown below in Fig 1-1. A second monoclinic phase, M2, is sometimes observed as an intermediate between M1 and R, and most commonly arises due to Al or Cr doping [12,13]. The M2 phase looks very similar to M1, but with a distortion of oxygen atoms that lengthens the crystal along the c-axis by 1% compared to M1 (and 2% longer than R phase). The large spontaneous strain that occurs when changing from phase to another forms the basis for the high-speed and large-displacement actuators we develop.

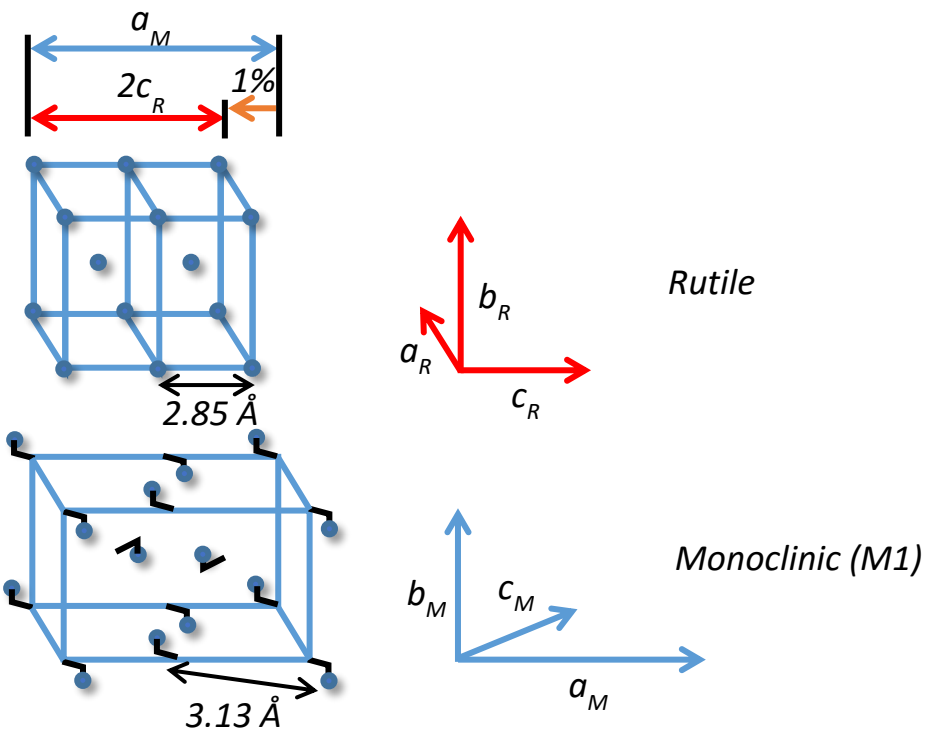

Figure 1-1. Crystal structure of VO_2. Above: rutile, high T phase, Below: monoclinic (M1) low T phase. Only oxygen atoms are depicted; vanadium atoms sit on the faces of the rutile unit cell and form tetrahedrons. Adapted from Ref. [13].

1.2 Motivation and Methods

The primary goals of this work are: 1) build and characterize new forms of VO_2 actuators, 2) engineer increased functionalities to VO_2-based devices through doping, and 3) explore the effect the structural phase transition on point defects within a material. For the first goal, we fabricate bimorph actuators using Cr coatings on VO_2 in two forms: nanobeams and thin film cantilevers. Nanobeams are grown by physical vapor deposition (PVD) and fabrication of bimorphs with evaporated Cr follows on randomly-positioned as-grown wires or those manually positioned by a micromanipulator. While the nanobeams offer superior performance due to their small size and single-crystallinity, a reliable actuator patterning and placement is desired. Thus, we develop a fabrication process using conventional photolithography, a single mask, metallization, and wet and dry-etching to realize VO_2 thin film actuators with controllable shape and position. High quality VO_2 thin films are grown by pulsed laser deposition (PLD), but we note that sputtering can also be used to achieve good results.

We characterize the operating speed and actuator displacement through activation by a chopped laser as well as by electrical Joule heating. We utilize Raman microscopy to detect the phases responsible for an enhanced actuation amplitude at intermediate input powers and frequencies.

Towards the second goal, we investigate tungsten doping of VO_2 thin films and nanobeams, owing to tungsten's very large effect towards decreasing the MIT temperature. Films are again grown by PLD, and their compositions are determined by Rutherford backscattering spectrometry (RBS). To properly design electronic devices with doped VO_2, we characterize the electrical transport properties of W-doped films via Hall effect. This allows us to understand the effect of doping not just on the electrical conductivity, but also carrier concentration and mobility. In order to understand the structural effect of tungsten doping, we perform RBS channeling, which presents a rough picture of the dopants and whether they are substitutional within the lattice. In doped nanobeams, we again utilize PVD, but we realize a novel doping scheme with a graded W doping profile along the axis of the nanowire length. We demonstrate that this design is superior to that of uniform doping, by spreading the MIT across a range of temperatures and positions along the material, allowing us to improve the functionality of VO_2 devices across a wider range of temperature.

For the final goal of studying the effect of the structural phase transition on point defects, we examine VO_2 nanobeams and thin films exposed to alpha-particle irradiation and varying thermal anneal treatments. The alpha particles are energetic He^{2+} ions that create point defects throughout the thin films and nanobeams. We characterize the defects in thin films by assessing their transport behavior, with carrier concentration and mobility giving a rough quantification of point defects. In nanowires, we analyze the MIT hysteresis behavior through thermal stage microscopy also as a rough quantification of defects. We note several possible scenarios where the strain and phase boundary motion of the MIT may cause increased point defect motion relative to a material without such a phase transition. To gauge this possible effect, we compare the effect of cyclically annealing the VO_2 thousands to millions of times across the phase transition, to a single-cycle anneal, where we hold the material above the MIT temperature for an equivalent time.

1.3 Dissertation Outline

We first discuss bimorph actuators based on VO_2 nanobeams in Chapter 2. We show that the operating speeds are limited by heat sinking to the environment through conducting and convective channels. The observed operating speeds match well with

those predicted by a simple model based upon the bimorph geometry. In this work, we also calculate the energy efficiency for actuating the VO_2 bimorphs to be nearly 3.6%, corresponding to thermoelectrics with figure of merit ZT = 2, operating in a temperature range ΔT of 40K (between room temperature and 67 °C). Here, we also show demonstrate the bimorphs to operate in water, as well as embedded in a polymer to form a millimeter scale actuator.

In Chapter 3, we demonstrate bimorph actuators made with VO_2 thin films through a conventional photolithography process. This enables the reliable placement of actuators and design of new shapes and functionalities, bringing these phase transition-activated actuators into the realm of MEMS devices. We compare VO_2-based actuators to other technologies and find that this technology offers exceptional speed, displacement (actuator stroke), and work density. We also investigate the effect of anneals and thermal processing on actuator behavior, to improve the development of fabrication processes suitable for multiple technologies.

Next, we discuss tungsten doping of thin films and nanobeams in Chapter 4. The electrical transport properties of VO_2 thin films are analyzed as W-doping is increased. The second half of this chapter details the study of nanobeams with a V-shaped W profile along their length. The graded distribution of W throughout the nanowire imparts different amounts of MIT temperature suppression, which results in the overall behavior of a much broadened phase transition across the device. This contrasts greatly with the pure VO_2 or WVO_2 doped at a constant composition, which transition at a precisely-defined temperature. The broadened response is useful for better control as a thermal actuator or reading of input temperature values. These axially graded-doped nanowires are characterized in terms of their thermal coefficient of resistance (TCR) and may be useful as a measurement material for infrared bolometry.

Chapter 5 details the study of point defects in VO_2 and their behavior in response to the MIT. We discuss several potential mechanisms where point defects may show increased mobility in response to the strain or phase boundary motion of the MIT. By comparing the quality of VO_2 thin films in their pristine state, after irradiation by ions (to introduce point defects), and after different anneal treatments, we assess the efficacy of a cyclic MIT-based anneal. The results suggest that there is no enhanced point defect motion from such an anneal, as the defective thin films recover similarly whether cycled thousands of times across the MIT or held at a constant T above T_C for an equivalent amount of time.

Finally, we summarize all the studies in Chapter 6, the conclusion, with discussion for future work. We further discuss applications of bimorph actuators and doped VO_2, as well as the implications of our study on point defects within VO_2.

Chapter 2

Nanobeam Bimorph Actuators

2.1 Background

Bilayer structures based on vanadium dioxide (VO_2) have demonstrated very large, reversible curvature changes when heated slightly above room temperature [14–16]. VO_2 undergoes a first-order metal-insulator transition (MIT) at 67 °C, accompanied by a structural transition from a monoclinic phase (M1, $T < 67$ °C) to a tetragonal rutile phase (R, $T > 67$ °C) with a large transformation strain of ~1% along the rutile c-axis (c_R). Coupling VO_2 with an inactive material to form a bilayer structure enables actuation with giant amplitudes [15]. The transformation strain is several orders of magnitude higher than that of conventional bimorph actuators that rely on a difference in linear thermal expansion coefficient between two materials [17]. Indeed, bimorphs incorporating poly-crystal thin films of VO_2 on Si micro-cantilevers have achieved large curvature changes [14,18] over 2500 m^{-1}, while bimorphs utilizing single-crystal VO_2 nano/microbeams coupled with Cr have produced curvature changes [16] over 23000 m^{-1}. Here, the single-crystalline nature of VO_2 nanobeams enhances the curvature change by aggregating the structural transformation strain along the bimorph length direction (nanobeam axis), in contrast to the case of poly-crystal VO_2/Si where the strain is partially cancelled and averaged along the bimorph length. This benefit results from the fact that single-crystal VO_2 nano/microbeams support single-domain MIT where the entire nano/microbeam cross section is a single structural phase, as opposed to spatially inhomogeneous MIT in the case of poly-crystal VO_2 thin films [11]. In addition to the large amplitude and high speed in actuation, the fact that the MIT in VO_2 can be triggered with a wide range of external stimuli (thermal, mechanical, optical as well as electrical) [9,14,19,20] greatly enriches the functionalities of such devices. However, the mechanism and fundamental limits of this VO_2-based actuation technology have not been evaluated in terms of practical performance metrics such as energy efficiency, speed, and actuation amplitude.

In this work, we theoretically analyze and experimentally demonstrate these limits by investigating single-crystal VO_2 nanobeams side-coated with Cr as bimorph

actuators in response to wind cooling as well as optical (laser) excitation. Here Cr is chosen for its high Young's modulus [15]. The devices actuate not only with larger amplitudes than those based on poly-crystal VO_2 films, but also respond to optical activation deep into the kHz range, which is half an order of magnitude faster [21]. A relatively high energy efficiency (equivalent to thermoelectrics of ZT = 2.1) is also predicted. By varying the frequency and location of the laser excitation, we analyze the heat transfer dynamics in these structures. The bending state of the thermally actuated device depends on the phase composition and domain structure of VO_2, which is dictated by the temperature profile along the bimorph. Thus, the ability of the cantilevered bimorph to accumulate and dissipate heat determines the maximum frequency at which such an actuator can be operated. Bimorph cantilevers with sub-micron cross sections exhibit enhanced rates of heat dissipation to ambient air benefiting from their large surface to volume ratio [22], and thus deliver actuation at higher speed compared to their thin-film based counterparts with bimorph widths far above microns.

2.2 Experimental Methods

Ultra-long VO_2 nanobeams were synthesized in a horizontal tube furnace from V_2O_5 powder (99%, Sigma-Aldrich), following physical vapor deposition (PVD) method recently reported by our research group. Unpolished quartz substrates were placed downstream from the source powder, resulting in long, freestanding nanobeams. The growth conditions were: temperature ≈ 880 °C, Ar carrier gas pressure ≈ 5 torr, flow rate ≈ 7 sccm, and time ≈ 3 hours. The growth products were analyzed by Raman and heated optical microscopy to confirm the identity and phase transition properties.

Nanobeams were manually transferred into the edge of Si substrates (Si substrate was pre-coated with 10 nm Cr and then 300nm Au to enhance thermal conductivity). Next, the nanobeams were clamped onto these substrates through ion-beam induced Pt deposition, with Pt thickness roughly matching the nanobeam thickness to ensure sufficient clamping and thermal conductivity. Next, a layer of Cr was deposited onto the side of the VO_2 cantilevers by electron-beam evaporation. Here Cr is chosen for its high Young's modulus. A Cr/VO_2 thickness ratio of ~ 0.4 was used to maximize the bending curvature, calculated from beam bending theory. Finally, the bilayer cantilevers were annealed in Ar at 250 °C to improve the clamping between Cr and VO_2.

Long and free-standing nanobeams grown on unpolished quartz were brushed several times with a Si chip to flatten and roughly align in the desired actuation direction. Next, bimorphs were formed by e-beam evaporation of Cr. PDMS (10:1 monomer ratio)

was dropcast onto a heated bimorph chip (85 °C) so that the bimorphs are all straight. The chip was spun at 7000 rpm for 45 sec and quickly returned to the hotplate for curing at 85 °C for 4 hours. Finally, the film was cut with a scalpel and peeled with a probe tip.

A continuous-wave argon ion laser (514.5nm) provided local heating to nanobeam cantilevers at room temperature. A low-jitter optical chopper pulsed the laser up to 4 kHz. A CCD video camera captured the fast oscillation of the cantilevers, and the tip moving amplitudes were extracted from individual video frames. We note that our camera is not fast enough to resolve each position of the bimorph oscillating at high frequencies, but the oscillation amplitude can be clearly determined from the video frames.

Micro-Raman spectroscopy was conducted at room temperature using a Renishaw 2600 system, with excitation provided by a 488nm Ar-ion laser. An Olympus 50× objective was used and the Raman signal was collected for several minutes, with laser intensities tuned to produce desired amounts of bending.

2.3 High energy efficiency of actuation

Figure 2-1a and b show the analogy between the proposed microscale solid engine (μSE) and the steam engine. It is known that the size change from a solid-solid structural transition is much smaller than the volume expansion in the liquid-vapor transition. However, solids offer much stronger force, which compensates for the small displacement. VO_2 is such a solid and undergoes the transition at 67 °C. Compared to the M1 structure, the R structure shrinks along the c_R-axis by ~1% and expands along the other two directions [23]. A second monoclinic, insulating phase (M2) can be stabilized by doping [24–26] or tensile stress [27–29] along c_R, as shown in the phase diagram [30] in Fig. 2-1c. The M2 phase, on the other hand, elongates by about 1% along c_R compared to M1 [13]. The strain is thus ~ 2% between the M2 and R phases.

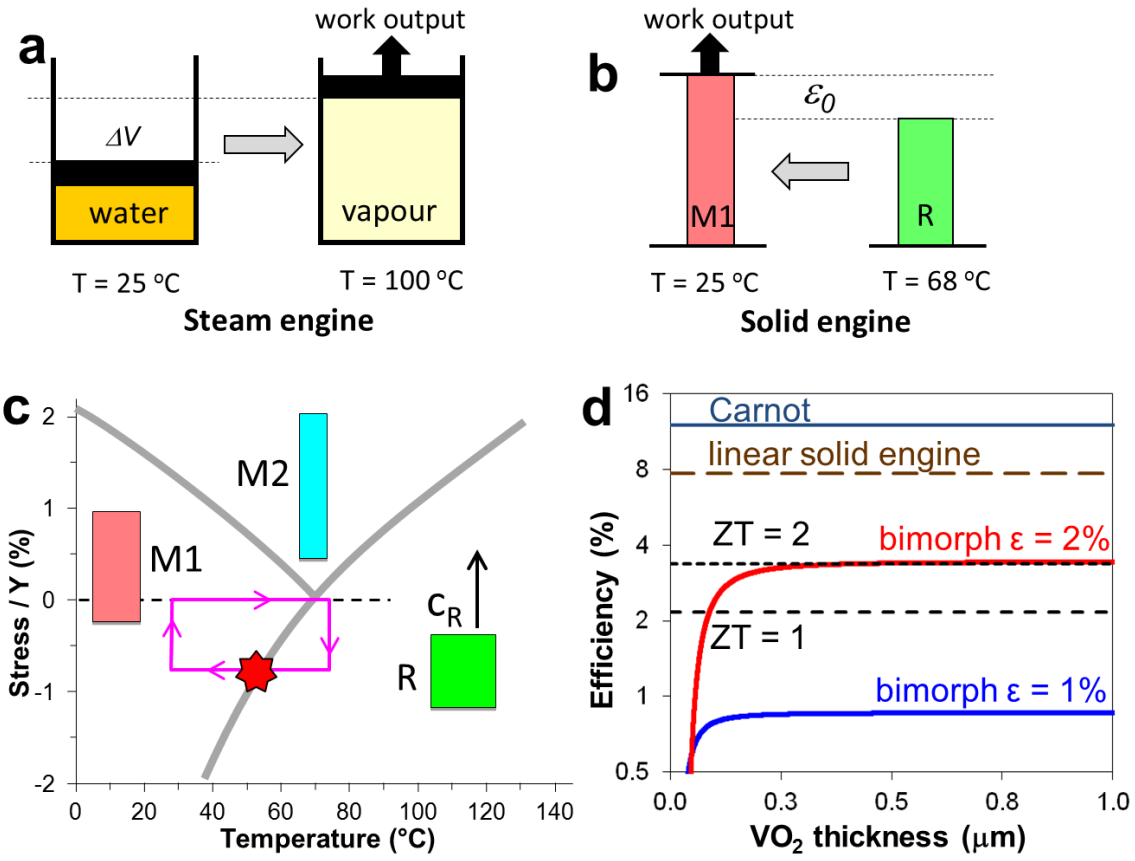

Figure 2-1. Operation Mechanism of VO_2 Solid Engine. ***(a)*** *Steam engine based on the liquid-vapor transition.* ***(b)*** *The micro solid engine based on a solid-solid phase transition.* ***(c)*** *The phase diagram (c_R stress vs. temperature) of VO_2. Here the stress is normalized by the Young's modulus (140GPa), and positive (negative) means tension (compression). The three rectangular boxes show schematically the length of a VO_2 nanobeam in the three phases, where the length direction (c_R) is vertical. The rectangular loop shows a possible cycle of the solid engine, and the red star is the point where the work is done.* ***(d)*** *Calculated energy efficiency of a VO_2-based linear solid engine and bimorph solid engines for transformation strain of ε = 1% (M1-R) and 2% (M2-R). Also shown is the energy efficiency of thermoelectrics with ZT = 1 and 2, and the Carnot efficiency between 68 °C and 27 °C. Conventional bimorphs based on differential thermal expansion would have a negligibly low (0.002%) efficiency.*

In micro-actuation, high amplitude and high force tend to be mutually exclusive due to the limited output work density of the working material that drives the actuation. The volumetric work density describes maximum mechanical work output per unit volume of the working material. It is given by $Y\varepsilon^2/2$, where Y is the Young's modulus of the material, which determines the strength of force, and ε is its maximum strain, which limits the actuation amplitude. The work density of VO_2 was estimated to be 0.63 J/cm^3

for poly-crystal films [15]. This value is calculated to be 7 J/cm^3 for single-crystal VO_2 beams, which is comparable to shape memory alloys, more than ten times higher than that of most organic materials and electrostrictive polymers, hundreds of times higher than piezoresistive materials [31], and three orders of magnitude higher than human muscles. The theoretical energy efficiency of a single-crystal VO_2 nano/microbeam oriented along c_R as a linear μSE can be calculated by dividing the maximum work output from the axial elongation by the total heat needed to drive the MIT. The former is calculated from the critical stress across the MIT, which is related to the latent heat (*H*) through the Clapeyron equation [11]. The latter is the sum of the latent heat and the energy needed to heat the VO_2 from T_{low} = 27 °C to T_{high} = 68 °C. The efficiency is given below in Equation 2.1 and derived in section ,

$$\eta_{linear} = \frac{T_{high} - T_{low}}{T_{high}} \cdot \frac{1}{1 + c\rho \cdot (T_{high} - T_{low})/H} \qquad (2.1)$$

where *c* is the specific heat and ρ is the density of VO_2. Figure 2-1d shows a high efficiency of 7.7%, equal to 64% of the Carnot efficiency (12%) for such a linear μSE operating between 27 °C and 68 °C. However, the displacement needs to be magnified for practical use. We couple the VO_2 nanobeam with a clamping layer (Cr in this case) forming a bimorph μSE to offer large microscale actuation transverse to the nanobeam axis (Fig. 2-3a and b).

By treating the bimorph as an elastic bilayer beam with a spring constant, we can calculate its energy efficiency as a function of VO_2 thickness for ε = 1% (M1-R) and 2% (M2-R). An efficiency of ~ 3.4 % is predicted for VO_2/Cr nanobeam bimorphs involving the M2-R transition (see Supporting Information). Impressively, this is equivalent in efficiency to thermoelectrics with figure-of-merit *ZT* = 2.1 operating between these two temperatures. As another comparison, conventional bimorphs based on differential thermal expansion between the two layers over this temperature range are estimated to have a much lower energy efficiency of ~ 0.002%.

The transformation strain, 1% for M1-R and 2% for the M2-R transition, is not only several orders of magnitude higher than that of conventional inorganic bimorph actuators relying on differential thermal expansion [17], but also much higher than the saturation strain in piezoelectric materials. Finally, shape memory alloys [32] and organics-based actuators [33] may provide strains greater than 5%, but VO_2 maintains the advantage of much higher force (due to higher Young's modulus) and speed (due mostly to lower temperature change needed).

2.3.1 Energy efficiency calculation for linear solid engine

For a linear micro solid engine (μSE) based on a VO_2 beam oriented along c_R with length *L*, width *a*, and thickness *b*, the maximum energy efficiency given by Equation (2.1) can be derived by the definition of efficiency, a ratio of output to input energy:

$$\eta_{linear} = \frac{E_{out}}{E_{in}} = \frac{L \cdot \varepsilon_0 \cdot \sigma_C \cdot a \cdot b}{Lab\rho c\Delta T + LabH} \tag{2.2}$$

where ε_0 is the transformation strain (analogous to volume change in the liquid-vapor transition, ≈ 1% for M1-R and 2% for M2-R), σ_C is the critical stress that would drive the phase transition at a given *T* (analogous to pressure in the liquid-vapor transition, and is the stress at the phase boundary in Fig. 2-1a), ρ represents density, c the specific heat, and H the latent heat. $\Delta T = T_{MIT} - T_0 = 68\ °C - 27\ °C$. The numerator in Equation (2.2) is the work output from a complete engine cycle as shown in Fig. 2-1a. The Clapeyron equation links σ_C to H,

$$\frac{d\sigma_C}{dT} = \frac{H}{\varepsilon_0 \cdot T_{MIT}} \tag{2.3}$$

Assuming a linear phase boundary [16], we have

$$\sigma_C = \frac{d\sigma_C}{dT} \cdot \Delta T = \frac{H \cdot \Delta T}{\varepsilon_0 \cdot T_{MIT}}. \tag{2.4}$$

Substituting into Equation (2.2), we obtain

$$\eta_{linear} = \frac{\Delta T}{T_{MIT}} = \frac{1}{1 + \rho c\Delta T/H} \tag{2.5}$$

which is Equation (2.1) for the generalized efficiency. We note that

$$\eta_{Carnot} = \frac{\Delta T}{T_{MIT}}. \tag{2.6}$$

As predicted by Equation (2.5), although the engine efficiency decreases as T_{low} moves toward $T_{high} = T_{MIT}$, its relative value would approach the Carnot efficiency if the engine is operated near the phase boundary ($\Delta T \to 0$).

2.3.2 Energy efficiency calculation for bimorph cantilever

We next turn to calculating the efficiency of work done by the bimorph μSE coupling a VO_2 and a Cr layer, which is more complicated than the linear structure. By treating the bimorph as a bilayer elastic beam with a spring constant, we can estimate the efficiency by dividing the mechanical work output at maximum displacement with the total heat absorbed (global heating). The spring constant is estimated from basic elastic beam theory [34],

$$k_{eff} = \frac{3a}{L^3} \cdot \frac{Y_1^2 b_1^4 + Y_2^2 b_2^4 + 2Y_1 b_1 Y_2 b_2 \cdot (2b_1^2 + 2b_2^2 + 3b_1 b_2)}{12(Y_1 b_1 + Y_2 b_2)} \tag{2.7}$$

where Y is the Young's modulus ($Y_{VO_2} \approx 140$ GPa and $Y_{Cr} \approx 280$ GPa), L the length, a the width and b the thickness of the beam, and subscript "1" and "2" denote the VO_2 layer and the Cr layer, respectively. Defining the total curved path of the tip motion as displacement D (green arc in Fig. 2-2), the work output for a full bending cycle is then

$$E_{out} \approx 2 \cdot \frac{1}{2} k_{eff} D^2 \tag{2.8}$$

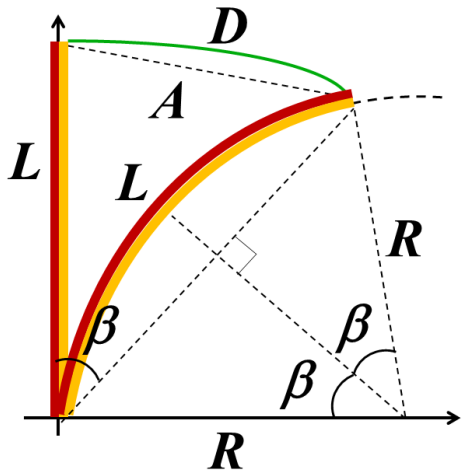

Figure 2-2. Geometry of the bimorph for bending and energy efficiency calculation. L is the length of the bimorph, D is the total displacement or path traveled by the tip, R the radius of curvature, and β the angle between the bent cantilever tip, cantilever root, and unbent cantilever tip.

Our system typically operates beyond the "small beam bending" limit, as the displacement is large, $D/L \approx A/L \approx 1$. However, we note that a simple scaling argument predicts the energy efficiency to be an intensive rather than extensive quantity, and be independent of the bimorph length *L*: a bimorph with length *L* outputs the same amount of work as two bimorphs each with length *L*/2 connected in series. Therefore, for the efficiency calculation, we only need to calculate for bimorphs with maximum bending still within the linear deformation regime $D/L << 1$. This is the case for bimorphs with small L. This is because the bending curvature $1/R$ is generally independent of the beam length L and is given solely by the thicknesses and Young's moduli of the two layers [16,35],

$$\frac{1}{\mathrm{R}} = \frac{6Y_1 b_1 Y_2 b_2 (b_1 + b_2)}{Y_1^2 b_1^4 + Y_2^2 b_2^4 + 2Y_1 b_1 Y_2 b_2 \cdot (2b_1^2 + 2b_2^2 + 3b_1 b_2)} \cdot \varepsilon_0 \tag{2.9}$$

where ε_0 is the transformation strain. For the Y_1/Y_2 ratio in our case, the largest $1/R$ is given by $b_2/b_1 \approx 0.4$. Comparing bimorphs with the same b_1 and b_2 thicknesses and thus the same $1/R$, those with smaller L give not only smaller D, but also smaller D/L. In fact, it can be proved from the geometry in Fig. 2-2 that generally,

$$D/L = \int_0^{\frac{L}{2R}} \left| \frac{\sin\beta}{\beta} \right| d\beta \tag{2.10}$$

At small deflection angles (*i.e.*, smaller $L/2R$), we have $D \approx L^2/2R$. Thus we can utilize the bimorph spring constant k_{eff} in the low-deflection Hooke's law behavior given by Equation (2.8) to predict a work output linearly proportional to L. Since the energy input E_{in} is also proportional to L, the energy efficiency ($\eta = E_{out}/E_{in}$) is therefore independent of L. As in the case of linear μSE, the energy input is given by:

$$E_{in} \approx La(b_1\rho_1 c_1 + b_2\rho_2 c_2)\Delta T + Lab_1 H \tag{2.11}$$

where c_1 is the specific heat of VO_2 (≈ 690 J/kgK) [1], c_2 the specific heat of Cr (≈444 J/kgK) [36], and *H* the latent heat of the MIT of VO_2 (≈ 1000 Cal/mol = 250 J/cm^3) [11]. A VO_2 density ρ_1 of 4.66 g/cm^3 was used [37], along with a Cr density [36] ρ_2 of 7.19 g/cm^3.

The calculated energy efficiencies are shown in Fig. 1d in the main text, for bimorphs with L = 5 μm while varying the thickness. These efficiencies are compared to those of thermoelectrics operating between $T_{high} = T_{MIT}$ = 68 °C and $T_{low} = T_0$ = 27 °C. Assuming the thermoelectric figure-of-merit to be *ZT*, the thermoelectric engine efficiency is given by:

$$\eta_{TE} = \frac{T_{high} - T_{low}}{T_{high}} \cdot \frac{\sqrt{1+ZT} - 1}{\sqrt{1+ZT} + T_{low}/T_{high}} \tag{2.12}$$

2.3.3 Calculation of cantilever resonant frequency

From beam theory, we know the spring constant for a simple beam in transverse oscillation [38] is given by:

$$k = \frac{F}{\delta} = \frac{3EI}{L^3} \tag{2.13}$$

forming the general case of equation (S7), where the bending modulus (stiffness) EI is replaced by the expression for a bimorph. We find the resonant frequency f_n with the relation

$$f_n = \frac{1}{2\pi}\sqrt{\frac{k}{m_{eff}}} \tag{2.14}$$

where $m_{eff} = \frac{33}{140}m = \frac{33}{140}\rho abL$ is used since the beam mass is distributed (resulting in varying velocities) along the oscillation length. For a beam sharing the dimensions in our experiment and the frequency calculations of thermal transport in the main text (L = 150 µm, a = 700nm, b_1 = 700nm, b_2 = 200nm), the resonant frequency is calculated to be 1.29 MHz, significantly higher than the frequencies examined by pulsed optical excitation. Thus the rise in deflection amplitudes at intermediate frequencies is not attributed to resonance, but rather the M2-R transition.

2.4 Characterization of device performance

2.4.1 High-amplitude actuation activated by global heating / cooling

Single-crystal VO_2 nanobeams grown by vapor transport are always oriented along the c_R direction with a rectangular cross section [39]. In a cantilevered bimorph of a VO_2 nanobeam coupled with Cr (Fig. 2-3a), the VO_2 near the interface is typically under compressive stress at room temperature, and the bimorph bends into a high curvature

state toward the Cr side (Fig. 2-3c). In heating the device above 68 °C, the VO_2 contracts into the R phase and the bimorph straightens, as shown in Fig. 2-3e. We define the actuation amplitude, *A*, to be the linear tip displacement between these two bimorph configurations. The normalized amplitude between these two states, *A* divided by the bimorph length *L*, is typically *A/L* ~ 0.8 or higher. This amplitude is extraordinarily large compared to inorganic bimorphs based on other mechanisms, and is also greater by nearly a factor of 3 than that achieved in poly-crystal VO_2/Si bimorphs [14,18]. The actuation can be induced by global (*i.e.*, substrate) heating as in this case, but it can be also activated by environmental temperature fluctuation (*e.g*. wind), as well as by local heating (*e.g*. a focused laser).

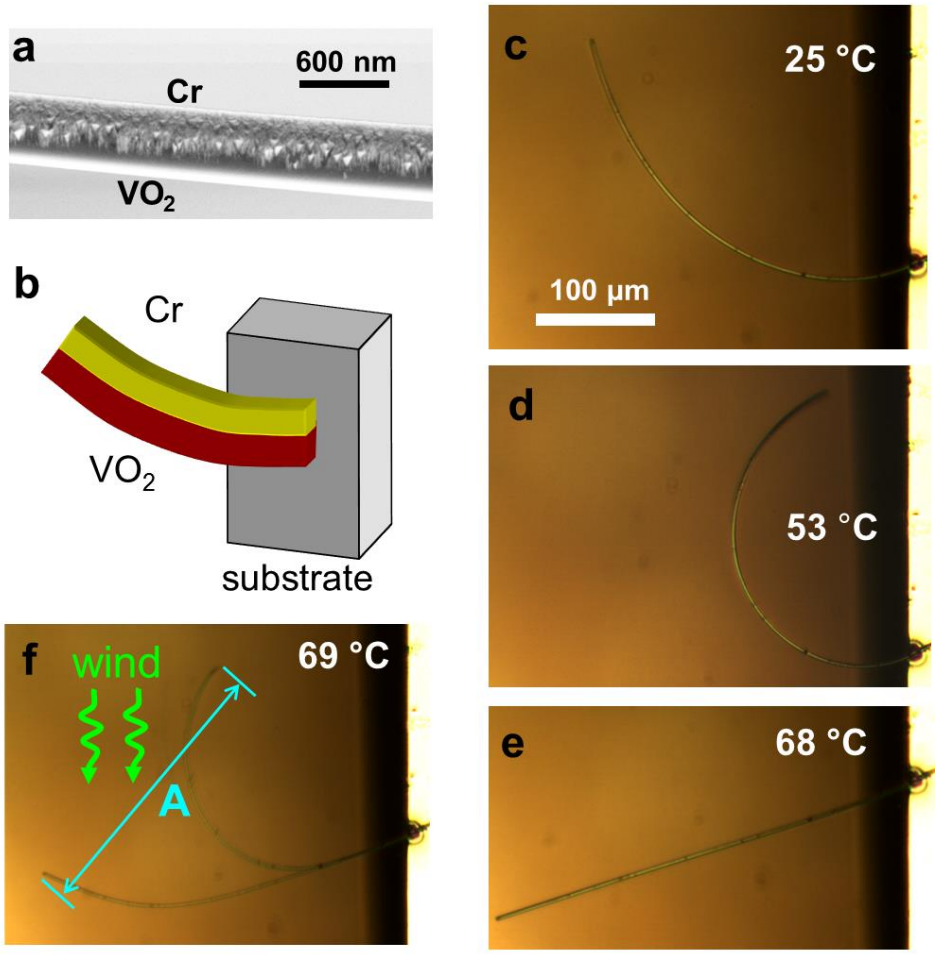

Figure 2-3. Nanobeam Bimorph Actuator. ***(a)*** *A close-up scanning electron microscopy image of the VO_2/Cr bimorph.* ***(b)*** *Schematic of a VO_2/Cr bimorph cantilevered from the substrate.* ***(c, d, e)*** *Optical image of a cantilevered VO_2(1 µm)/Cr(0.3 µm) bimorph at substrate temperature of 25*

°C, 53 °C and 68 °C. Length L = 217 µm and width a = 1 µm. ***(f)*** *Fast and high-amplitude oscillation of the bimorph under room-temperature wind cooling where the substrate is at 69 °C.*

When heating the Si substrate to above 68 °C and simultaneously blowing gentle, room-temperature wind toward the device, the VO_2/Cr bimorph cantilevers rapidly and irregularly oscillate (Fig. 2-3f and video in Supporting Information). The oscillation arises from turbulent air convection that cools the bimorph cantilever across the MIT, rather than any mechanical pushing force imposed by the wind. To confirm this, we performed the same experiment without heating the Si substrate, and the VO_2/Cr cantilever did not oscillate with any volume or direction of wind. This is expected because the kinetic force from the wind onto objects with sub-micron cross section is negligible.

Upon global heating, the bimorphs bend outward (straightening) at T > 68 °C as expected for the M1-R transition; interestingly, before that, at intermediate temperatures, the VO_2 bimorphs bend inwards (increasing curvature, Fig. 2-3d). Due to the ~1% elongation of the VO_2 nanobeam upon the M1-M2 phase transition, the VO_2/Cr bimorph bends further toward the Cr side resulting in an increase in curvature. This strain is more than an order of magnitude higher than the contribution of linear thermal expansion difference [23,40] between Cr and VO_2, which produces a strain of only 0.028% between room temperature and 68 °C. This M2 strain also significantly increases the actuation amplitudes, with A/L rising to > 1.2 in most bimorphs. This is analyzed below in more detail using local laser heating.

2.4.2 Spatially resolved activation by local heating with a focused laser

A laser focused on the VO_2/Cr bimorph thermally actuates the device by locally driving the phase transition at the hot spot along the VO_2 nanobeam. The dynamics of heat transfer for our quasi-1D system are governed by [22,41]:

$$\rho c \frac{\partial T(x,t)}{\partial t} = \kappa \frac{\partial^2 T(x,t)}{\partial x^2} - 2h \frac{a+b}{ab}[T(x,t) - T_0] \qquad (2.15)$$

where κ is the effective thermal conductivity of the nanobeam bimorph. T_0 is the environment temperature (27 °C). h is the total heat transfer coefficient from the bimorph surface to air. a and b are the bimorph width and thickness, respectively. In the case of continuous local laser heating at a fixed location, varying laser power produces different bending curvatures as shown in Fig. 2-4. We attribute the inward (outward) bending to the laser activated local transition of M1 to M2 (R). This is further confirmed by micro-Raman spectroscopy carried out at different laser intensities. The Raman spectrum recorded at the intermediate (high) laser intensities clearly proves the local

emergence of the M2 (R) phase. We note that in bimorphs based on poly-crystal VO_2 thin films, due to their spatially inhomogeneous phase transition, such clear M1-M2-R transition and the resultant amplitude enhancement are not resolved [14,18].

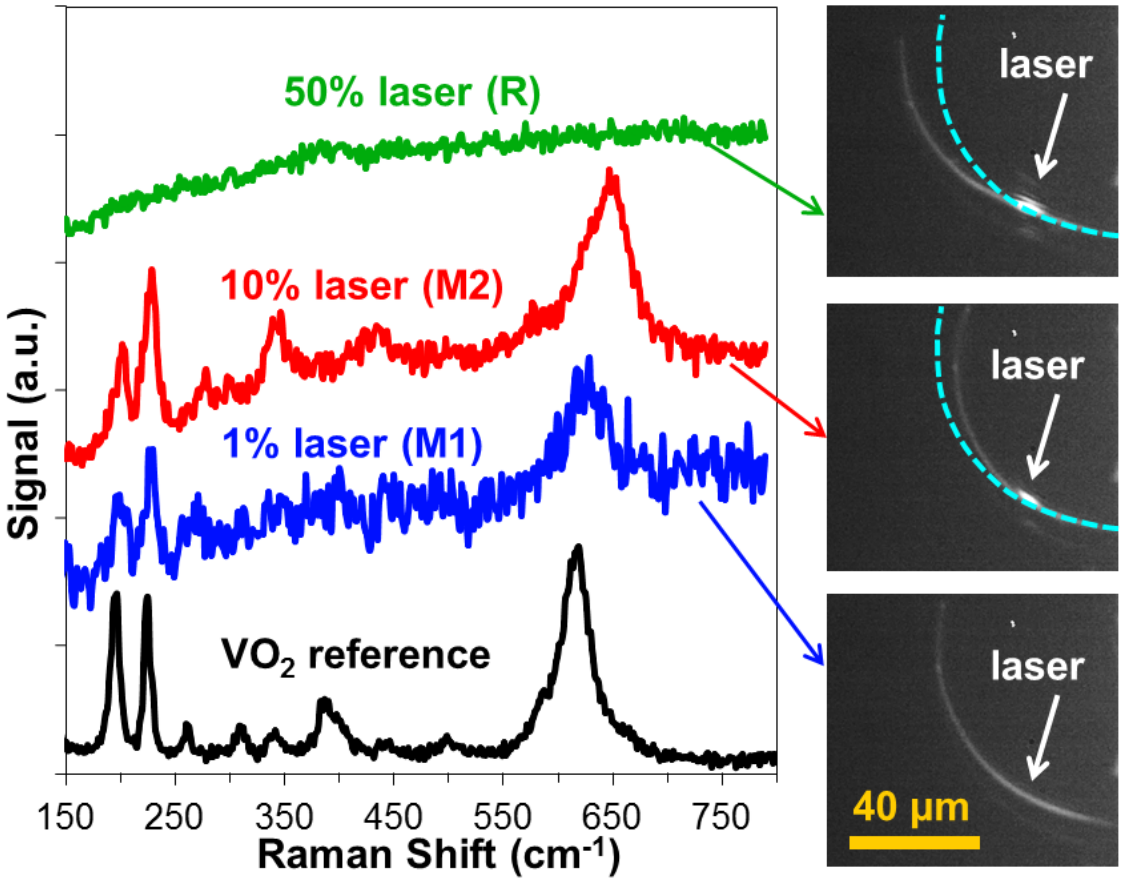

Figure 2-4. Bending and Raman at Various Laser Powers. Three bending states of a VO_2/Cr bimorph activated by a continuous laser heating at increasing laser intensities (1%, 10% and 50%), corresponding to M1, M2 and R local phase at the laser spot as identified by the Raman spectra. It is known that the 615 cm^{-1} peak in the M1 phase shifts to 650 cm^{-1} in M2 phase [42,43], and R phase exhibits no Raman due to its metallicity. The dashed curve in two of the images represents the original bimorph configuration to show the bending. The experiments were performed in ambient and the substrate is at room temperature. Here 100% laser power corresponds to 1 mW.

2.4.3 High-speed operation and dependence on frequency and power

By investigating the bimorph bending as a function of continuous laser power and focusing position, we obtain a clear picture of the actuation behavior. As shown in

Fig. 2-5a, for a fixed laser position, low to intermediate laser powers cause the bimorph to deflect in the negative direction (bending inward) due to the M1-M2 transition, while high laser powers produce deflection in the positive, outward direction due to the M1-R transition. The temperature distribution depends primarily on heat dissipation through two channels: i) "sub", conduction along the bimorph to the Au/Si substrate, and ii) "air", dissipation to the ambient *via* air convection and conduction, as shown in the first and second terms on the right hand side in Equation (2.15). The characteristic time constants for these two heat dissipation channels [41] are $\tau_{sub} = \frac{x^2 \rho c}{4\kappa}$ and $\tau_{air} = \frac{\rho c}{h} \cdot \frac{ab}{a+b}$. Clearly, τ_{sub} depends only upon the distance (*x*) for heat to diffuse from the laser spot to the substrate, while τ_{air} relies only on the bimorph surface area, *a*·*b*, in contact with air. For typical devices with laser position at *x* ≈ 150 μm, we estimate the characteristic maximum response frequencies to be $f_{sub} = 1/\tau_{sub}$ ≈ 0.4 kHz, and $f_{air} = 1/\tau_{air}$ ≈ 3 kHz. We also note that bimorphs with smaller cross section would perform well up to higher frequencies, owing simply to the higher surface-to-volume ratio which reduces τ_{air}. Figure 2-5b displays the *x*-dependence of bimorph bending angle between laser on and off (in the low-frequency limit), calculated from $\theta \approx A/(L-x)$. Approaching the root (*x* = 0), the rapid drop in θ is due to the increasing "sub" effect. Far from the root and the substrate, the *x*-independent "air" effect dominates as expected.

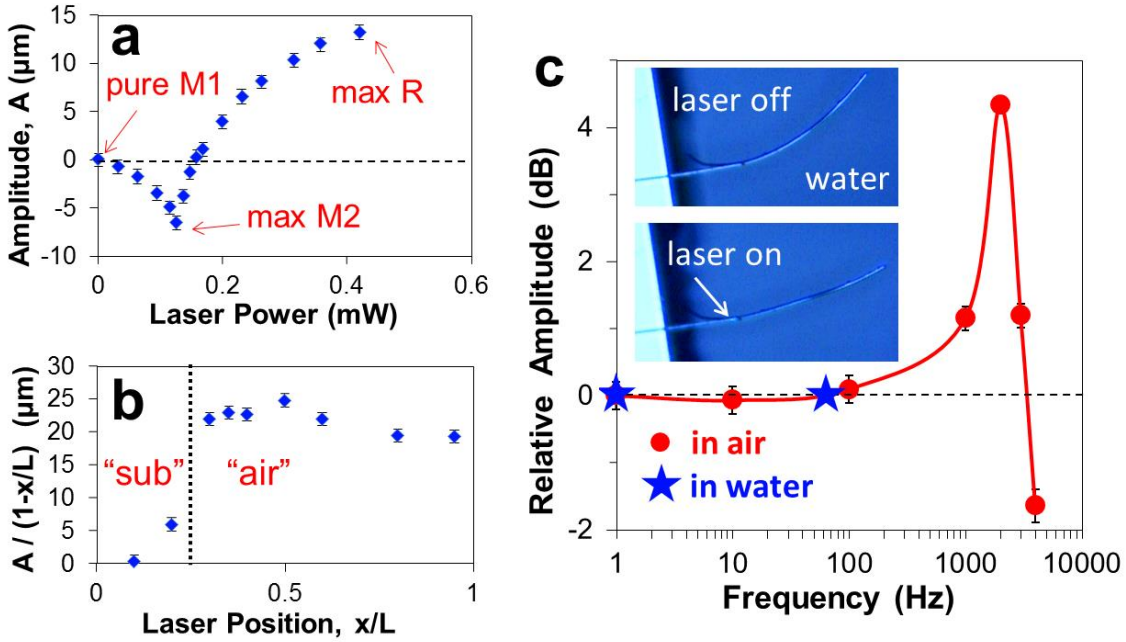

Figure 2-5. Cantilever Response to Laser. ***(a)*** *Actuation amplitude as a function of continuous laser power at fixed laser position x/L = 0.3. Negative amplitude indicates inwards bending due to the activation of M2 phase.* ***(b)*** *$L \cdot \theta$ as a function of laser position at fixed laser power of 0.4 mW, where $\theta \approx A/(L-x)$ is the bending angle. Here the bimorph is VO_2(700nm)/Cr(200nm), length L = 100 μm, width a = 700 nm, and the substrate is at room temperature.* ***(c)*** *Amplitude of actuation operated in room air and water activated with a chopped laser. Here the bimorph is VO_2(900nm)/Cr(300nm), length L =115 μm, width a = 900nm. Incident laser power is 0.5 mW and relative position is fixed at x/L = 0.5. Inset shows actuation in de-ionized water with a continuous laser.*

For many applications, it is critically important for the actuator to operate at high speed. We now activate the actuation with pulsed localized heating by chopping the incident laser beam at frequency *f*. At very high frequencies, the actuation amplitude *A* is expected to rapidly decrease, due to inability of the bimorph to dissipate heat and return to its original un-heated state within the period of time 1/*f*. From bimorphs based on poly-crystal VO_2 films, Merced *et al.* [21] observed the attenuation of *A* to -3dB ($1/\sqrt{2}$ amplitude) at a laser chopping frequency f_{-3dB} ~ 1kHz. Figure 2-5c shows measured *A versus f* from a typical nanobeam VO_2/Cr bimorph. Here we plot $A(f)$ in decibels by $20 \cdot log[A(f)/A_{DC}]$, where $A_{DC} = A(f = 0)$ is the linear displacement of the bimorph tip between its unperturbed position and its state under continuous laser activation (with the same laser intensity). It can be seen that indeed for very high frequencies (*f* > ~ 3 kHz), *A* starts to decrease; but at intermediate frequencies, *A* actually increases. This is

because the VO_2 nanobeam at the laser spot is no longer just switching between M1 and R phases with 1% axial strain, but is instead transitioning between M2 and R phases with higher (~2%) axial strain.

The phase diagram in Fig. 2-1c helps clarify the behavior at intermediate frequencies, where the bimorph loop is instead raised upwards and right into the M2/R region. Now, the useful work could be collected at the M2/R phase boundary, while cooling limitations prevent the VO_2 from switching back to the M1 state. To ensure that the rise in amplitude is not due to mechanical resonance, the cantilever's resonant frequency was calculated in section 2.3.3 to be 1.29 MHz, significantly higher than the optical actuation frequencies. At the maximum laser chopping frequency of 4 kHz, *A* has dropped to only ~ -2 dB. Extrapolating the data points beyond here, we estimate the 3dB-attenuation frequency of $f_{\text{-3dB}}$ is ~ 4.5 kHz, nearly five times faster than values reported for bimorphs with poly-crystal VO_2 films [18]. This is expected from the much smaller cross section of our bimorphs, and is consistent with the f_{air} estimated above.

2.4.4 Effect of bimorph geometry on operation speed

The bimorph actuation can be analyzed by decomposing the total oscillation amplitude into inward bending amplitude A^{M2} (from the unperturbed position towards the max M2 position) and outward bending amplitude A^{R} (from the unperturbed position towards the max R position), so that the total amplitude $A(f) = A^{M2}(f) + A^{R}(f)$. By plotting the two oscillation amplitudes separately, we see that the rise in $A(f)$ at intermediate f results from an increase in $A^{M2}(f)$, as shown in Fig. 2-6. This is explained by the limited cooling as the frequency rises. The peaking and eventual decrease of $A^{M2}(f)$ at higher f also occur due to the cooling limitations – the VO_2 is unable to cool to a sufficiently low temperature, not even able to reach the M2 phase, and therefore stays in the heated R phase during the entire time of laser pulsing. The results with varying frequency at 3 positions along this bimorph are shown in Fig. 2-6. A sustained outward bending behavior can be seen for x/L = 0.3, producing considerable bending up to high frequencies. The high performance may represent an optimal excitation position on this bimorph, maximizing both "sub" and "air" modes of heat transfer and increasing the operating speed of the device.

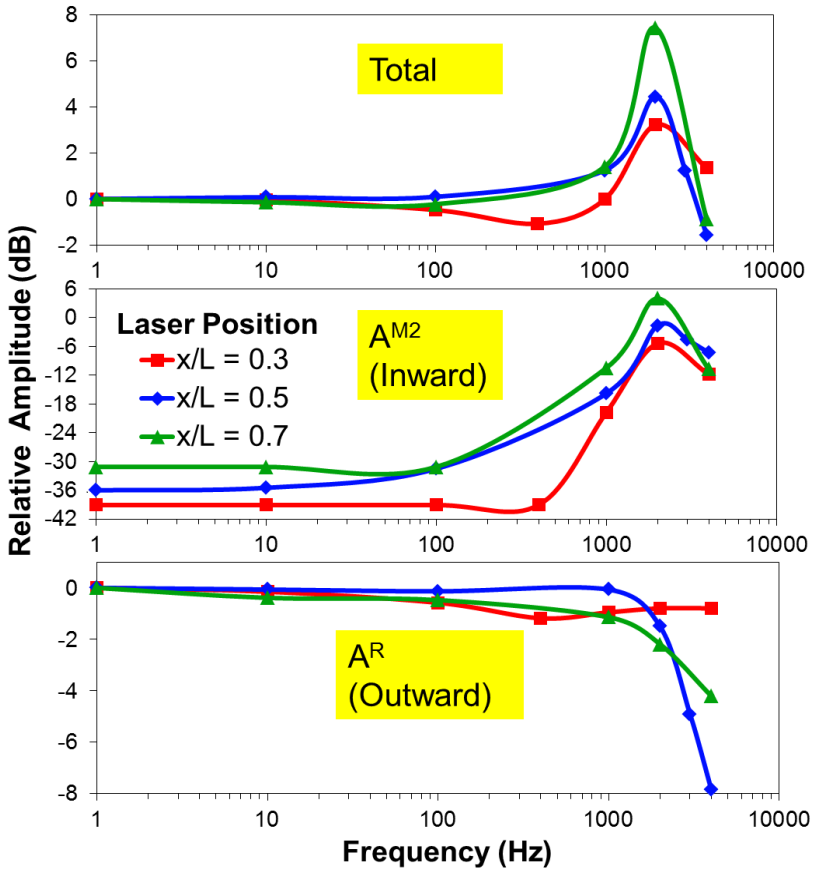

Figure 2-6. Decomposition of the total amplitude into M2 amplitude and R amplitude shows the different frequency behavior of the actuation driven by the M1-M2 and M1-R transition. Colored lines are provided as a visual aid. Three laser positions are shown.

By comparing the $A(f)$ dependence between bimorphs of various cross section areas, we can better understand the "air" term of heat dissipation. Figure S2 plots $A(f)$ for 3 bimorphs and reveals an improving high-frequency performance as the VO_2 thickness decreases. The peak displacements occur at frequencies of ~ 1, 2, and 3 kHz for bimorphs with VO_2 nanobeam thickness of 1, 0.9 and 0.7 µm respectively. This agrees with the predicted behavior, since the thinner bimorph has a greater surface to volume ratio, which increases the efficacy of the heat dissipation to air. Referring to the time constant τ_{air} in section 2.4.3, the characteristic frequency is inversely proportional to the "effective bimorph diameter", $ab/(a+b)$a. This qualitatively agrees with our observation of higher f_{-3dB} at smaller bimorph thickness.

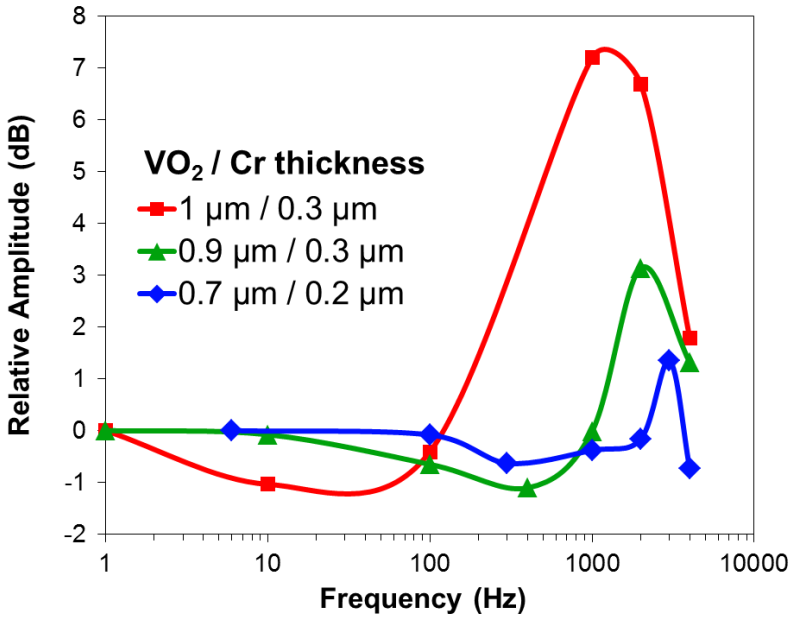

Figure 2-7. Frequency response of actuation of 3 cantilevers with different VO_2 thickness. Bimorphs have similar width. Lengths are 100, 115, and 217 μm, respectively. The laser power is fixed for the experiments, and the focal position along the bimorph is fixed at x/L ~ 0.4 for all three curves.

Due to the fixed laser intensity, the outward oscillation towards R phase ($A^R(f)$), shown in Fig. S1, cannot increase with f. The eventual decline in $A^R(f)$ may be attributed to a negative feedback effect inherent in the sideways deflection of the experiment. The laser is directed at a point to heat the bimorph in its straight state, and the bimorph absorbs most of the incident laser energy under continuous and low frequency laser operation. At higher frequency operation, the nanobeam spends more time away from the initial state, settling instead in the inward or M2 bending region when the laser is chopped to be off. Consequently, when the laser pulse switches back on, less of the bimorph is in the pathway and less incident energy is absorbed, which reduces the total displacement and heating back towards the R position. It is possible that an alternate experimental setup, with nanobeam oscillation in the plane of the laser beam, could yield high tip displacement performance at even higher frequencies. In this hypothetical setup, the inward (M2) bending is expected first to decline to zero with further inability to cool, followed by the decrease of R-phase bending at high frequencies. Here, the displacement would saturate into the maximum R position. In this regime, the bimorph is unable to cool even to M2 temperatures and retains the laser-induced R-phase, producing the same displacement that occurs at a continuous laser irradiation. Nonetheless, even given these limitations, the nanobeam bimorphs

respond with outward R phase displacements at very high frequencies. From Fig. 2-5(c), the 3dB-attenuation frequency is 2.5kHz, solely considering outward bending.

Videos of actuation by laser are shown for a 217 µm long bimorph with thickness VO_2(1 µm)/Cr(0.3 µm), and width 1 µm. A low-frequency (10 Hz) chopped laser results in M1-R switching, while high-frequency (2kHz) results in primarily M1-M2, as shown in Movies 3 and 4, respectively in the online supplementary info to the ACS Nano article.

2.5 Alternative operating environments

2.5.1 Operation in aqueous condition

In addition to working in air, the nanobeam device also delivers high-amplitude and high-speed actuation in aqueous conditions. The inset of Fig. 2-5c shows the bimorph deflected by a laser in water. From the recorded video (Supporting Information), the actuation is stable and the response time in water is faster than 17 msec, the time resolution of our camera. This is faster by several orders of magnitude than other aqueous actuation mechanisms such as polymer swelling. Compared to polymeric materials, the higher speed arises fundamentally from the much higher thermal conductivity and lower specific heat of VO_2, as well as the fast speed of the MIT and the small temperature rise needed to drive the MIT.

A video recording hosted in our ACS Nano publication shows the bending of a bimorph soaked in de-ionized water and activated with a laser beam turned repeatedly on and off. By analyzing individual video frames, it is found that the bimorph completes bending within the time lapse between two consecutive frames. The video frame rate is 60/sec, giving an upper limit of the response time of ~17 msec and lower frequency limit of 60Hz. The actual speed should be much faster.

The amplitude response of the device shown is much lower than that shown in Fig. 2-5c, due to the illumination point far from the base, exciting a reduced region to phase transition. Additionally, the Cr has started delaminating, visibly peeling from the base of the bimorph and causing discontinuities along the bimorph length. The loss of bonding between the two layers dramatically reduces the net strain difference in the bimorph, reducing the amplitude change. Physical degradation like this can be prevented by a more careful Cr deposition, followed by a post-deposition anneal.

2.5.2 Demonstration of a hybrid smart composite

By aligning VO_2/Cr bimorphs and incorporating them into a polymer matrix, we can extend the large-amplitude actuation to the macro-scale, and form a hybrid smart composite film, useful for fluidic valves and smart shape-programmable structures. Figure 5 shows the large-amplitude actuation (A/L = 0.9) by global heating such a millimeter-scale smart composite. The composite is a dense assembly of aligned VO_2/Cr bimorphs embedded into a thin film of polydimethylsiloxane (PDMS) measuring 2 mm $\times$1 mm in size. A slight inward bending was also observed between 25 °C and 37 °C, consistent with the M2 phase formation in VO_2. It can be envisioned that by depositing Cr onto only patterned regions of aligned VO_2 nanobeams, followed by PDMS molding, one can program the location, direction and amplitude of actuation in the smart composite.

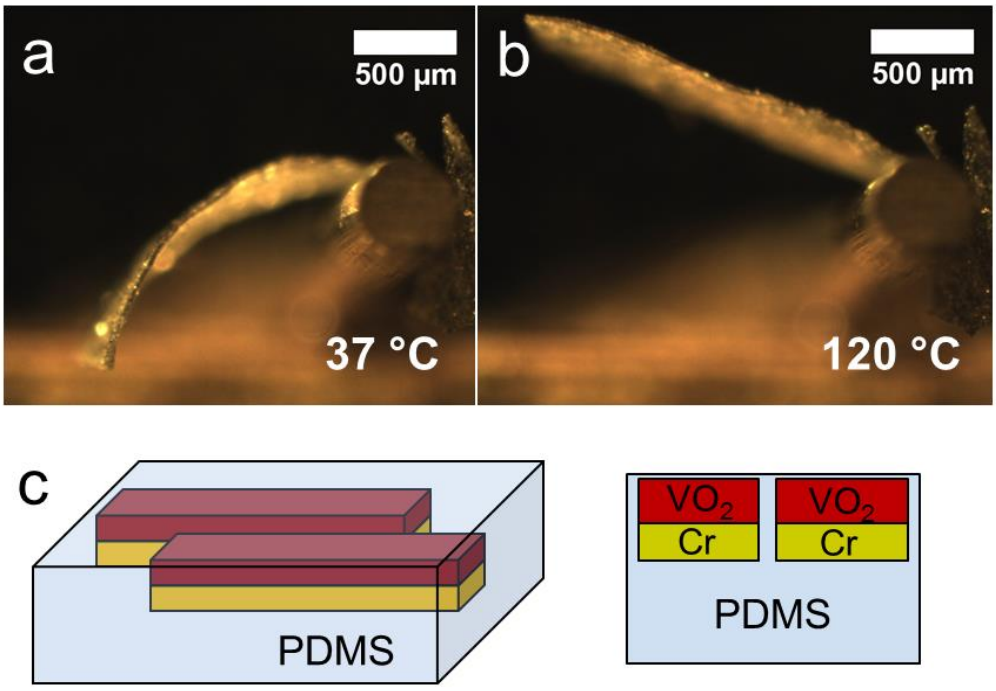

Figure 2-8. Hybrid VO_2 Actuator in PDMS. ***a)*** *Low-temperature curved state of the hybrid smart composite film.* ***b)*** *High-temperature straightened state. Global heating is provided through the metal base at the right. The film is 2mm long, 1mm wide, and 20 µm thick.* ***c)*** *Schematic 3D view and cross section view of the hybrid composite film.*

2.6 Conclusion

We report a bimorph actuator composed of a single-crystal VO_2 nanobeam coupled with a Cr layer. Unlike traditional bimorph actuators based on differential thermal expansion, the actuation of this device is activated upon the structural phase transition in VO_2 at a temperature slightly above room temperature. The actuation can be driven thermally, optically or electrically. We investigate time-independent and time-dependent actuation behavior of the actuators using focused pulsed laser heating. Compared to previously reported bimorph actuators based on poly-crystal VO_2 thin films with much larger width, these single-crystal VO_2 nanobeam based bimorphs exhibit superior performance in terms of i) much higher actuation amplitude (by a factor of ~ 3), and ii) much faster response speed (by half an order of magnitude). The former is explained by the single-crystallinity of the VO_2 nanobeam used, such that the VO_2 undergoes the phase transition *via* a single domain to maximize the use of transformation strain, as opposed to random, multiple domains in the case of thin films. The latter is explained by the smaller width and thus higher surface-to-volume ratio of a nanobeam-based bimorph, which facilitates heat dissipation to ambient air. Moreover, due to the single-domain nature of the phase transition, an otherwise hidden phase (M2) plays an important role; a complicated and non-monotonic actuation behavior is observed and explained on the basis of the phase diagram of VO_2. The energy efficiency of our devices is calculated to be equivalent to thermoelectrics with $ZT = 2.1$.

The bimorph as a μSE can be easily fabricated and integrated at the nanoscale and up to the milliscale. The device functions may be further broadened and efficiency further enhanced by reducing the MIT temperature of VO_2 from 68 °C toward room temperature with a small concentration of tungsten doping [44]. As heat slightly above room temperature is ubiquitous and much more abundant than those at higher temperatures, the bimorph μSE demonstrated here may be used as sensors, actuators and energy harvesters operating in near-room-temperature, ambient or aqueous conditions, including physiological and microfluidic environments.

Chapter 3

Thin Film Actuators

3.1 Motivation

In order to increase the versatility of phase transition-based microactuators, we next develop VO_2 thin film-based bimorph actuators which are patternable by photolithography, allowing us to control their shape and functionality. To re-emphasize the importance of microactuation technology, we note that direct conversion of external stimuli to mechanical motion at the micro to nanoscale is of vital importance in micro- and nano-electromechanical systems, micro-robotics, and biomimetics [45–47]. A wide range of materials featuring different stimuli-responsive properties are used for the actuation. On the inorganic side, differential thermal expansion [48–50], piezoelectric ceramics [51–54], and shape memory alloys (SMAs) [55,56] are typically utilized. The relative size change (strain) in these systems is usually low (except for SMAs), on the order of 10^{-4} ~ 10^{-3} even at strong stimuli such as high operating voltage or large temperature change. Consequently, they typically output small displacements far shorter than the actuator length, even with magnification mechanisms such as assembled in a bimorph structure. Actuators based on polymers or carbon nanotubes exhibit high flexibility and huge size change [45,57–61], but their intrinsically low response speed, weak force output, and incompatibility with current microfabrication processes present severe limitations. Therefore, it is much desired to develop microactuators that can deliver simultaneously high amplitude and strong force at high speed by using conventional microfabrication techniques.

The fundamental reason that high amplitude and high force tend to be mutually exclusive is related to the limited output work density. The volumetric work density describes maximum mechanical work output per unit volume of active material that drives the actuation. It is given by $\mathrm{E} \cdot \varepsilon^2/2$, where E is the Young's modulus of the active material, which determines the strength of force, and ε is the maximum strain, which limits the actuation amplitude [45]. Figure 3-1a shows the E versus ε plot of a range of active materials for actuation [45,62,63], in comparison to vanadium dioxide (VO_2), the material we used in this work. It can be seen that owing to its simultaneously high E

(~140 GPa) and high ε (~ 1% in single crystals), a work density as high as 7 J/cm^3 is theoretically possible by using VO_2 as the driving material. This is comparable to SMAs, over an order of magnitude higher than that of inorganic materials and electrostrictive polymers, and three orders of magnitude higher than human muscles (~ 0.008 J/cm^3) [45]. On the other hand, although being able to deliver high work densities, SMAs need a wide temperature variation for reactivation in cyclic actuation; moreover, when thickness is reduced to the sub-micron scale, SMAs tend to lose the memory function owing to martensite-austenite phase compatibility issues. As a result, SMA actuators are currently limited to low operating frequencies and low displacement to length ratios [55,62].

VO_2 undergoes a thermally driven metal-insulator phase transition (MIT) accompanied by a structural transition slightly above room temperature (67 °C) [11,39,64]. As its lattice changes from monoclinic (insulating, I) to rutile (metallic, M) structure upon heating across the MIT, VO_2 shrinks by a transformation strain of ε ~ 1% along the *c* axis of the rutile phase (c_R) (Fig. 3-1b), while expanding along the other two directions [11]. Combining the high *E* which is expected for a transition metal oxide, the high ε , the low stimulating temperature needed, the intrinsically fast MIT process (~ pico-second) [65], VO_2 arises as an ideal driving material for microscale actuation. Indeed, bimorphs of Cr on VO_2 nanowires [16] and VO_2 film on Si cantilevers [14,18] have been reported showing high bending amplitudes under direct heating; however, devices in these approaches cannot be lithographically fabricated to achieve different geometries and functionalities for fitting various microactuation needs, and the observed speeds (~ 300Hz) and amplitudes were far from the theoretical limits.

In this work, we demonstrate a set of Cr/VO_2 bimorph microactuators with layers in nanoscale thicknesses using batch microfabrication, and the devices exhibit superior performance by nearly all metrics. In addition to the high work density output and high response speed expected, they offer the highest displacement-to-length ratio in the sub-100 μm length scale. They respond with high sensitivities to various thermal, electrothermal and photothermal stimuli, and work with high durability in both ambient and aqueous conditions.

3.2 Device fabrication and theory

The microactuators were fabricated by patterning and etching Cr/VO_2 double-layer thin films deposited on Si substrates with a 1.1-μm-thick thermal oxide (SiO_2). VO_2 films with different thicknesses varying from 100 to 300 nm were prepared by pulsed laser deposition (PLD) (Fig. 3-1c), and the majority of data shown in this work are based

on an optimal VO_2 thickness of 118 $\pm$ 5 nm. Across the MIT, the as-deposited VO_2 film exhibits a drastic change in resistivity by over two orders of magnitude (Fig. 3-1b), as well as a change in optical reflectivity under white light illumination. The Raman spectrum (Fig. 3-1d) at room temperature shows strong peaks identified as the I phase of VO_2. These peaks decrease in intensity with increasing temperature, and finally disappear due to metallicity of the high-temperature M phase.

The specific PLD growth recipe for VO_2 on SiO_2/Si substrates is as follows. Si substrates with 1.1-μm-thick thermal SiO_2 were thoroughly cleaned by solvent and oxygen plasma and placed in a PLD chamber. The chamber was pumped to a base pressure of ~ 10^{-3} mtorr, and then oxygen was introduced in with the pressure stabilized at 10 mtorr. After that, the substrates were heated to 520 °C at a rate of 20 °C/min, and then a KrF laser beam (wavelength 248 nm) was focused onto a VO_2 target (99% purity) with an intensity of ~ 25 mJ/mm^2 to deposit the film with a rate of about 2.6 nm/min. Afterwards the substrates were naturally cooled down at a rate of 10 °C/min under the same oxygen pressure.

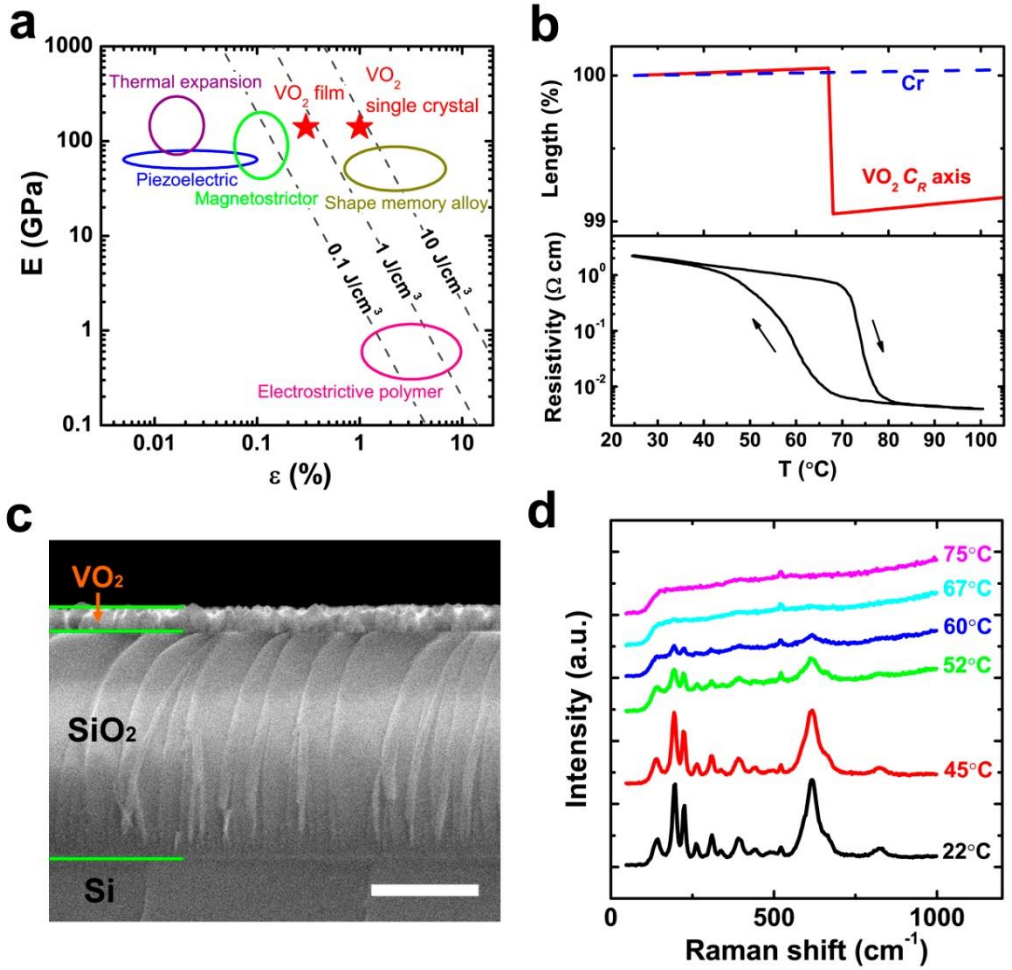

Figure 3-1. Properties of VO_2 thin films. (a) Young's modulus (E) versus strain (ε) plot of various actuation materials. Data for high-strain piezoelectric ceramics, thermal expansion (⊿T=10K), magnetostrictor, shape memory alloys, and electrostrictive polymers are summarized from Refs. [45,62,63]. Also plotted are the contours of equal volumetric work density calculated using $E \cdot \varepsilon^2/2$. (b) Upper panel: Schematic plot of the transformation strain and thermal expansion of VO_2 and Cr. Lower panel: Temperature-dependent resistivity of a VO_2 film measured by four-probe method, showing the metal-insulator phase transition. (c) Cross-sectional SEM image of a VO_2 film deposited on SiO_2/Si substrate. Scale bar is 500 nm. (d) Raman spectra of a VO_2 thin film at different temperatures. Note that the small peak at 520 cm^{-1} is from the Si substrate.

SiO_2/Si is chosen as the substrate because VO_2 films PLD deposited on the surface of amorphous SiO_2 are textured with the c_R axis lying in the plane of the substrate [66]. The structural texturing is the key that enables bimorph actuation based on VO_2; otherwise, a completely random orientation of micro-grains in the VO_2 film would cause the c_R-axis shrinkage to be fully cancelled by the expansion in a_R and b_R axes. In addition,

the SiO_2 layer underneath VO_2 can be selectively removed with wet etch without damaging the VO_2 layer, thereby releasing the VO_2 film layer as a cantilever. Figure 3-2 shows schematics of the microactuator fabrication process. Prior to the etching, Cr was lithographically patterned and deposited onto the VO_2 film by e-beam evaporation, and then rapid thermal annealed at 150-300 °C for 120 sec (Fig. 3-2a and b). Cr is selected here because it wets VO_2 and has a high Young's modulus. Then a photoresist pattern was defined by photolithography to cover part of the substrate (Fig. 3-2c) which would be the base part supporting the finally released structures (Fig. 3-3).

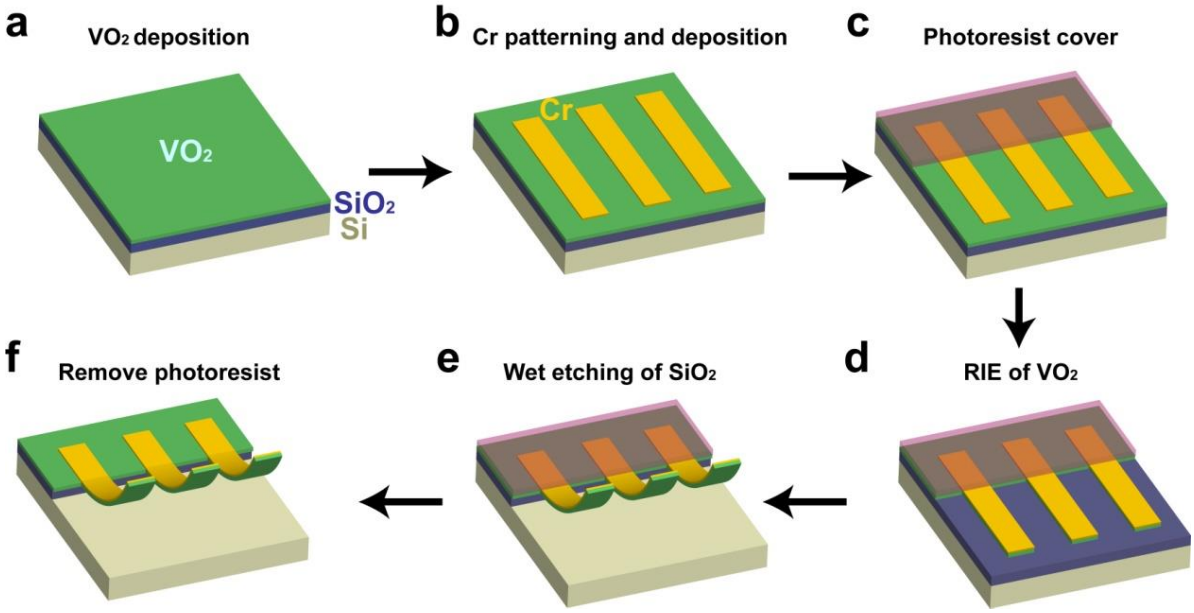

Figure 3-2. Schematic of microfabrication process. (a) Pulsed laser depositing VO_2 thin film on SiO_2/Si substrate. (b) Defining, depositing and annealing the Cr pattern. (c) Partially covering the pattern with photoresist. (d) Dry etching the exposed VO_2 film. (e) BOE etching SiO_2 layer exposed and under the Cr/VO_2 pattern. (f) Dissolving the photoresist by replacing BOE gradually with water and then acetone.

Reactive ion etching (RIE) was used to etch the exposed parts of VO_2 without significant lateral etching (Fig. 3-2d), and the parts of VO_2 protected by either Cr or photoresist remained un-etched. Afterwards, the substrate was immersed into buffered oxide etchant (BOE 5:1) for a period of time depending on the width of the pattern, so as to under-etch the SiO_2 layer beneath the Cr/VO_2 pattern. As a result, the Cr/VO_2 bimorph structures not protected by the photoresist were released from the substrate and became free-standing (Fig. 3-2e). Finally, the BOE solution was gradually replaced

by water and then acetone to dissolve the photoresist, followed by natural drying in air (Fig. 3-2f). The fabrication process allows us to make microactuator structures in batch with a wide variety of sizes and arbitrary geometries, as shown in Figs. 3-3 and 3-4. The released Cr/VO_2 bimorph curves toward the Cr side at room temperature. This is because the Cr was deposited onto VO_2 at a temperature higher than its MIT temperature when it was in the M phase with smaller in-plane lattice constants; as a result, when the Cr/VO_2 bimorph became free-standing at room temperature, release of the built-in stress caused the bimorph to bend away from the VO_2 side.

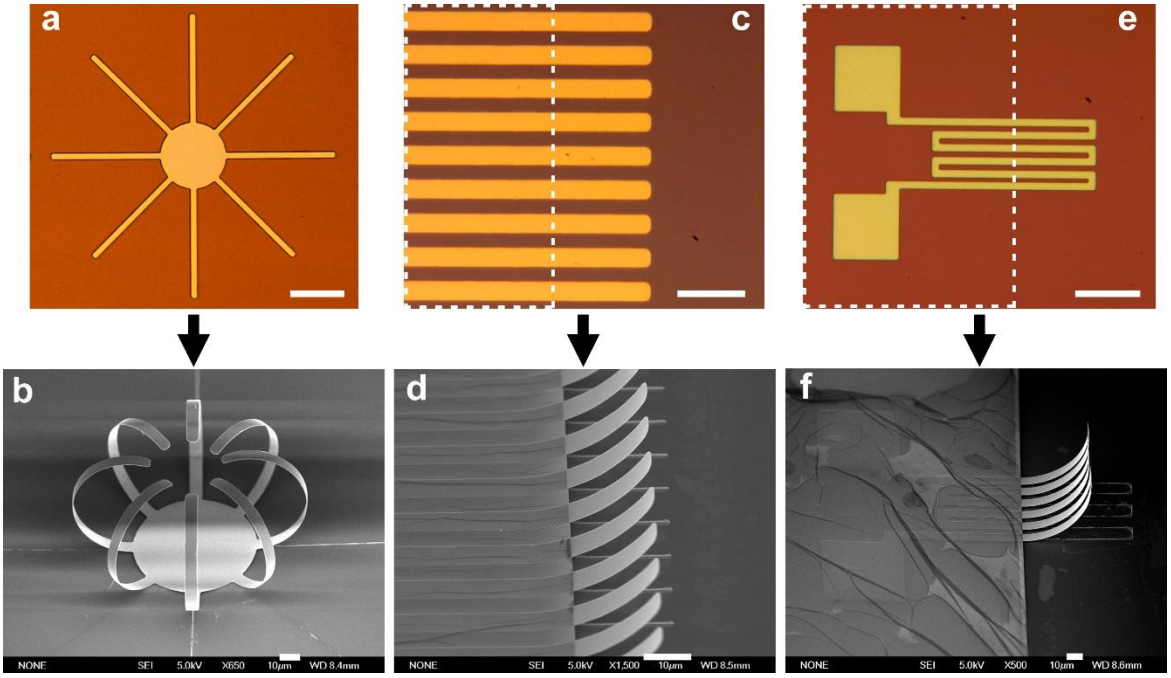

*Figure 3-3. Two-dimension pattern designs (**a, c, e**, optical images after Cr deposition) and final three-dimension microactuator structures (**b, d, f**, SEM images after etching, at room temperature). **(a)** and **(b)**, Palm structure with eight fingers. **(c)** and **(d)**, Comb structure with parallel aligned cantilevers. **(e)** and **(f)**, Micro-heater structure for electrical actuation. The rectangular areas in dashed boxes in c and e indicate the parts covered by photoresist, as shown in the step c of Fig. 3-2. Scale bars: a, 50 µm; b, 10 µm; c, 20 µm; d, 10 µm; e, 50 µm; f, 10 µm.*

The specific process after photolithography is given next. First, Cr layers were deposited onto the VO_2 thin film by e-beam evaporation at a rate of 2 Å/s. Annealing was carried out in a rapid thermal annealing furnace under Ar environment, for a ramp-up time of 30 s followed by an annealing time of 120 s at the target temperature. Reactive ion etch (RIE) was carried out in a mixed gas of SF_6 (90%) and O_2 (10%) with a flow rate of 60 sccm, under a pressure of ~ 89 mTorr, and at a working power of 100 W;

the etching time was 12 s for the films used in this work. The wet etching used 5:1 BOE solution with an etching time depending on the width of the Cr/VO_2 structure, which is 25 ~ 28 min for the 5 μm width and 45 ~ 50 min for the 10 μm width. Build-in stress between the Cr and VO_2 causes the bimorph to bend towards Cr when released, detaching the Cr/VO_2 bimorph from the clamping substrate prior to the underlying SiO_2 being completely etched.

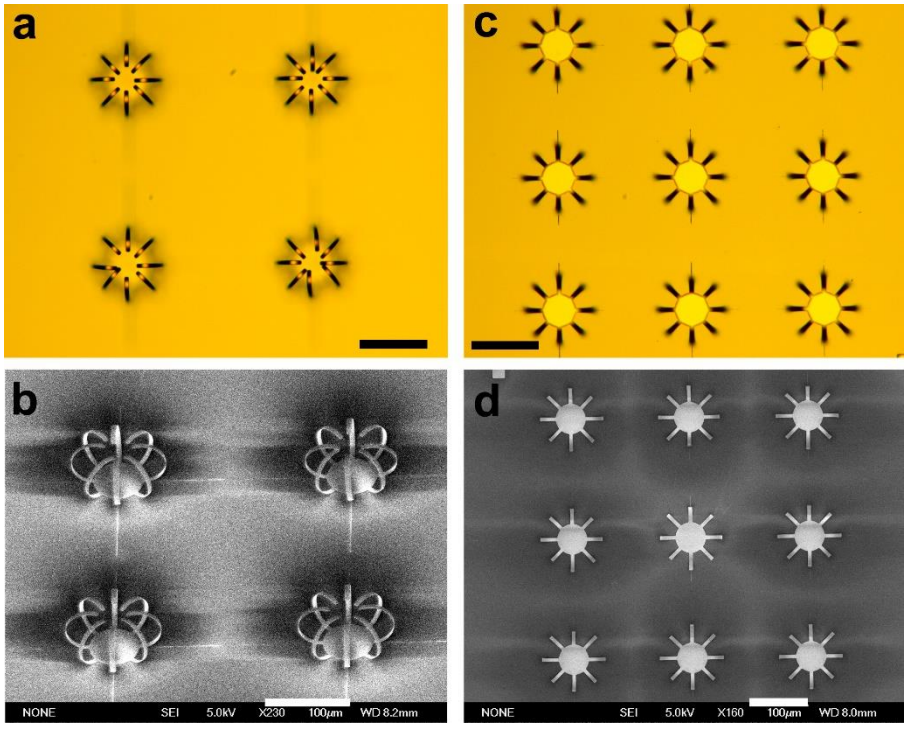

Figure 3-4. Batch fabrication of palm structures. ***(a)*** *and* ***(b)****, four palm structures with fingers 100 μm long, optical image in top view and SEM image in tilted side view, respectively.* ***(c)*** *and* ***(d)****, nine palm structures with fingers 50 μm long, in top-view optical image and SEM image, respectively. Scale bars: a-d, 100 μm.*

3.2.1 Calculation of curvature

The Cr/VO_2 bimorph exhibits a large change in curvature upon the MIT of the VO_2, acting as a thermally driven microactuator offering giant actuation amplitudes. Figure 3-5a shows side-view optical image of a cantilevered Cr/VO_2 bimorph at two temperatures merely 15 ˚C apart from each other across the MIT. The tip displacement for this 60-μm-long bimorph is 36 μm, giving a displacement (*D*) - to - length (*L*) ratio of *D*/*L* = 0.6. With longer bimorph, *D*/*L* exceeding 0.9 has been achieved (Fig. 3-6). The high *D*/*L* is attributed to a giant change of ~ 22,000 m^{-1} in bimorph curvature across the MIT, as shown in Fig. 3-5b, which mimics the MIT-induced resistivity change in Fig. 3-1b. The curvature change is much higher than bimorphs based on other mechanisms such as differential thermal expansion and piezoelectricity; it is also higher than VO_2 film-coated Si cantilevers [14,18]. For such a bimorph with a rectangular cross section, the curvature change $\Delta\kappa = \Delta(1/\mathrm{R})$ is proportional to the relative length change (strain change $\Delta\varepsilon$) of the active layer (VO_2) in the bimorph [35],

$$\Delta\kappa = \frac{6E_{Cr}E_{VO_2}t_{Cr}t_{VO_2}(t_{Cr}+t_{VO_2})}{E_{Cr}^2t_{Cr}^4 + 2E_{Cr}E_{VO_2}t_{Cr}t_{VO_2}\left(2t_{Cr}^2+3t_{Cr}t_{VO_2}+2t_{VO_2}^2\right)+E_{VO_2}^2t_{VO_2}^4}\Delta\varepsilon \qquad (3.1)$$

where E_{Cr} = 280 GPa and E_{VO_2} = 140 GPa are the Young's modulus of Cr and VO_2 layers, respectively, and t_{Cr} and t_{VO_2} are their thicknesses. Using this equation, an effective strain change of $\Delta\varepsilon$ ~ 0.3% in the polycrystalline VO_2 is estimated across the MIT. Although this is lower than the c_R-axis transformation strain (1%) in single-crystal VO_2, it is orders of magnitude higher than the strain deployed in existing bimorph actuators, namely, the strain caused by differential thermal expansion (estimated to be ~ 0.03% between VO_2 and Cr from 25 ˚C to 67 ˚C), and the strain accumulated in piezoelectric materials (typical ~ 0.01% at an applied field of 100 V/mm).

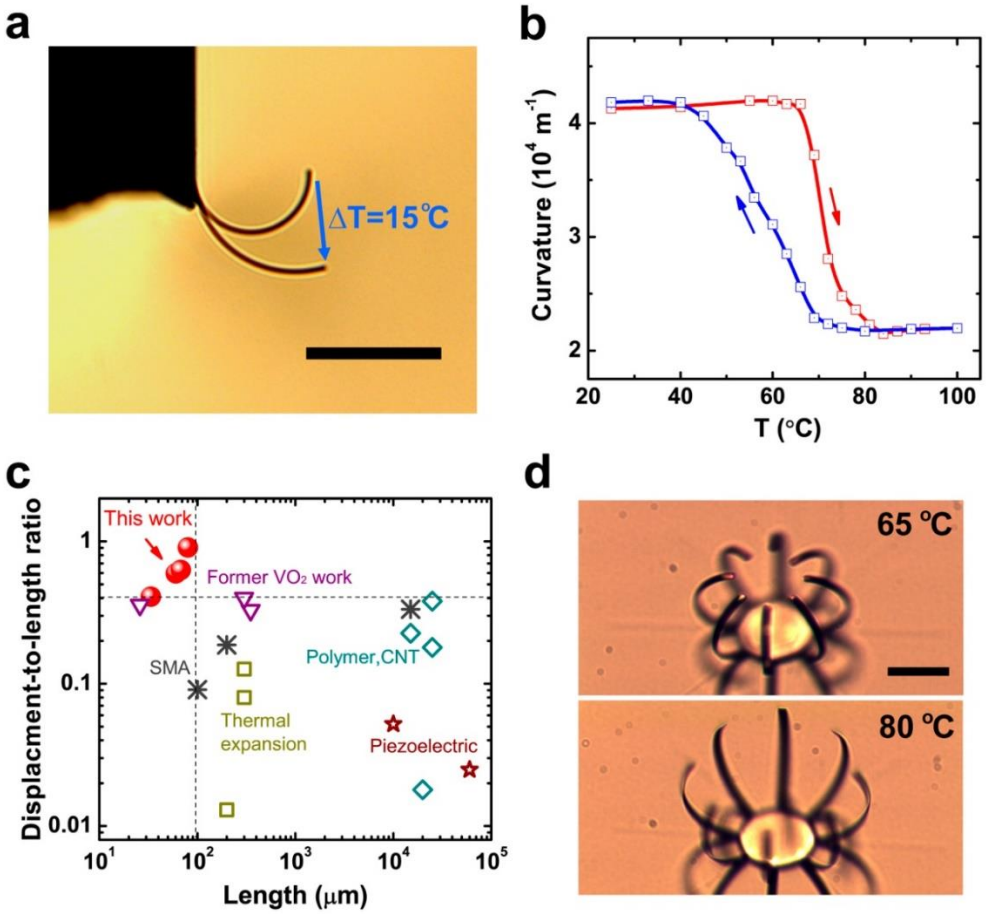

Figure 3-5. Thermally activated bimorph microactuators. ***(a)*** *A cantilevered bimorph showing a large bending amplitude when temperature is increased by ⊿T=15 ℃. Scale bar is 50 μm.* ***(b)*** *Dependence of bimorph curvature on temperature across the VO_2 phase transition (bimorph is Cr/VO_2=50/118 nm, annealed at 200 ℃).* ***(c)*** *Ratio of actuation amplitude (tip displacement) to actuator length D/L, compared to that of thermal bimorphs (Refs. [48–50]), piezoelectric bimorphs (Refs. [51,54]), shape memory alloy-based bimorphs (Refs. [55,56]), polymer or CNTs (Refs. [57–60]), and other VO_2 nanowires or films based bimorphs (Refs. [14,16,18]).* ***(d)*** *Microactuator with a "palm" structure, showing the fingers closed at 65 ℃ and open at 80 ℃. Scale bar is 50 μm.*

3.2.2 Large displacement-to-length ratio

The relative actuation amplitude, represented by the tip displacement-to-length ratio *D*/*L*, is one of the key metrics for microscale actuation. A large *D*/*L* ratio allows actuators that occupy small volume to drive motion over long distance. Our giant *D*/*L* up to unity for *L* less than 100 μm is unusually large compared to other actuation

techniques and materials. As shown in Fig. 3-5c, *D*/*L* of all existing bimorph actuator technologies is limited to 0.4, despite their lengths exceeding 100 μm. We note that for a cantilever with given amount of change in bending curvature ($\Delta(1/\mathrm{R})$), its tip displacement *D* is proportional to the cantilever length *L* squared, instead of *L* as shown in Fig. 3-6 (and discussed in section 2.3.2). Therefore, a longer *L* favors not only higher *D*, but also higher *D*/*L*; thus achieving high *D*/*L* is especially challenging for short *L*. Figure 3-5c shows that the Cr/VO_2 bimorph actuators provide the highest relative amplitude especially for the sub -100 μm regime. In addition, Equation (3.1) indicates that the giant curvature change also benefits from the small thickness of the layers in the bimorph (100~200 nm), as $\Delta\kappa$ scales inversely with the thickness. In contrast, SMAs, the only other material competitive to VO_2 in terms of work density, cannot reach deep sub-μm thickness without sacrificing the actuation properties. We note that for certain applications, thicker bimorphs may be needed to offer larger forces or higher work at the cost of actuation amplitude. Given the high Young's modulus and high work density of VO_2, a high force can be achieved at relatively small bimorph thicknesses. Effects of Cr thickness and annealing temperature on the actuation amplitude are shown and discussed in section 3.4 (Fig. 3-9).

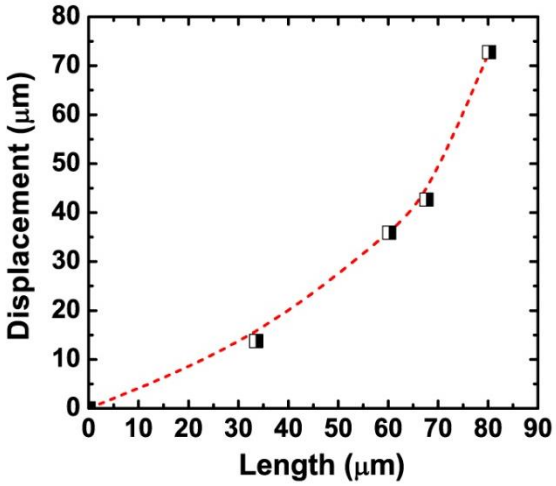

Figure 3-6. Measured tip displacement versus total arm length of Cr/VO_2 (thickness 50 nm/118 nm) bimorph cantilevers.

The major advantages of thin film-based device fabrication are size scalability and versatility in designing arbitrary patterns to fit different needs. Figure 3-5d shows a palm structure as a microactuator that can be thermally activated. Varying temperature from room temperature to 80 °C repeatedly opens and closes the palm (see

supplementary movies online at Nano Letters). Such a structure might be suitable for on-demand capturing and releasing micro-objects, such as cells or pharmaceuticals.

3.3 Performance of Electro- and Photo-thermal Actuation

The actuation can be also activated electrothermally with an electric current, or photothermally with a focused laser. Such electrical and optical control of the actuation offers capability of addressing individual devices at much higher speed and smaller scale than by global heating. As shown in Fig. 3-7a, a micro-heater structured actuator utilizes Joule heating of current flowing through the actuator itself to achieve the actuation. Owing to good electrical conductivity of the Cr and VO_2 layers, a small applied voltage (1.4 V) renders the actuator to bend at its maximum amplitude (Fig. 3-7b) using a low input power of 1.6 mW. In ambient condition, the curvature changes by ~ 14,000 m^{-1} between the voltage ON and OFF states. The electrical actuation is also completely reversible free of materials fatigue and deterioration. Figure 3-7c shows the resistance of the actuator monitored during operation driven by an applied square-wave voltage alternating between 0.2 V and 1.4 V at a frequency of 0.2 Hz. The resistance changes by 5% between the states under high and low voltages due to the current-controlled MIT of the VO_2 layer. The actuator went through tens of thousands of actuation cycles in air without noticeable degradation in performance, suggesting a long lifetime and high durability.

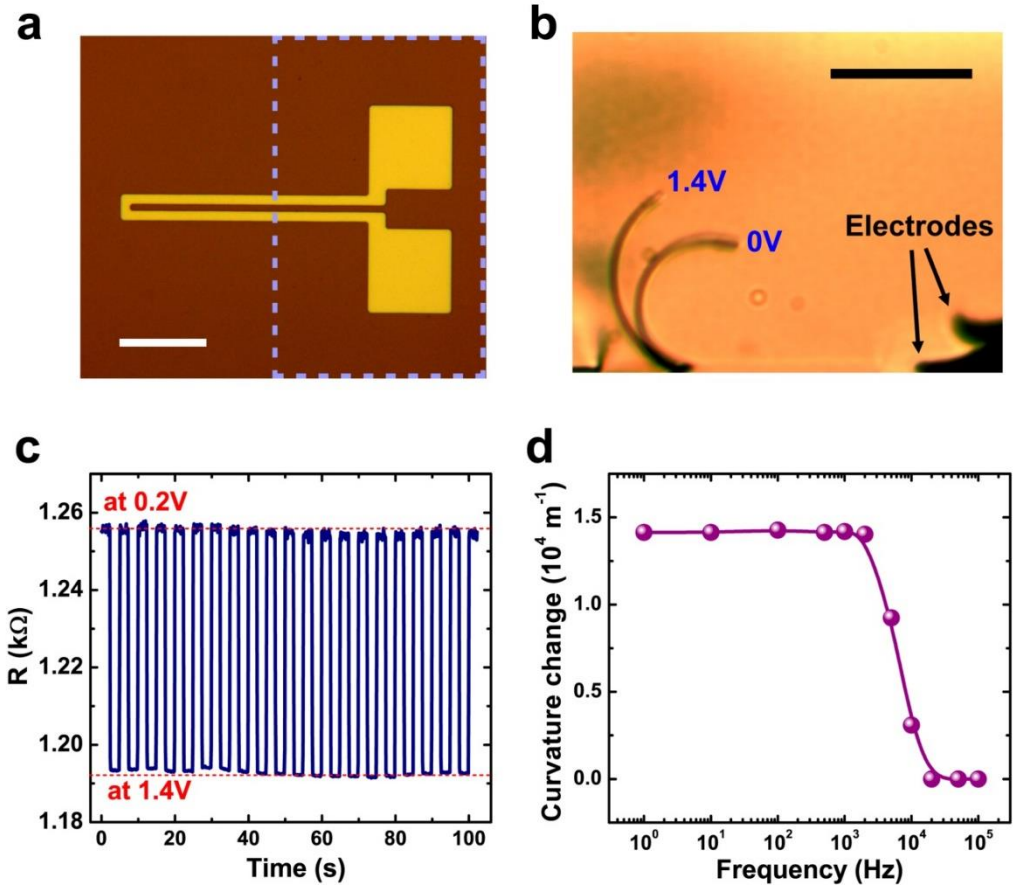

Figure 3-7. Electrically activated bimorph microactuators. ***(a)*** *Top view of a micro-heater actuator patterned out of the Cr/VO_2 bimorph. The part outside the rectangular box will be under-etched and thus free standing. Scale bar is 50 μm.* ***(b)*** *Side view of a micro-heater actuator activated by Joule heating. Bimorph is Cr/VO_2=50/118 nm. Scale bar is 50 μm.* ***(c)*** *Resistance of the actuator when a square wave of voltage is applied, showing high durability of actuation. The voltage switches between 0.2 V and 1.4 V at a frequency of 0.2 Hz.* ***(d)*** *Dependence of the bimorph curvature change on the frequency of the applied voltage, showing a half-amplitude cut-off frequency (3dB) of ~ 6 kHz.*

Figure 3-7d shows dependence of curvature change on the frequency of the square-wave voltage applied. The actuation amplitude remains constant at the maximum until the frequency exceeds 2 kHz. The 3dB attenuation frequency (where the amplitude is reduced by half) is about 6 kHz, corresponding to a response time of ~ 0.17 ms. We note that this definition of 3dB attenuation frequency (1/2 amplitude) is looser than that of the nanobeam actuator in Chapter 2 since the latter chooses $1/\sqrt{2}$ amplitude for energy considerations. The smaller-dimension nanobeam devices are expected to operate faster due to their enhanced convection. Thus, to match their 3dB

specification, the cutoff frequency for these thin film devices drops from 6 kHz to 3.5 kHz, which is indeed slower than the 4.5 kHz cutoff frequency for the nanobeam actuators. The actuation is completely cut off at ~ 20 kHz, where the pulsed heating becomes faster than the heat dissipation through thermal conduction to the substrate and convection to ambient air. This process is slower than piezoelectrically driven actuators (> tens of kHz), comparable to differential thermal expansion actuators, but much faster than shape memory alloy actuators and any polymer and ionic motion - based actuators (< hundreds of Hz).

Compared to thermal and electrical activation, light is desired for contactless and spatially resolved control of actuation through photothermal activation. Figure 3-8 shows actuation of palm structures in air and water with a focused laser. The laser can address each finger of the palm individually in a room-temperature environment with a low power of 4 mW (Fig. 3-8a). This power is on the order of, but larger than, the electrical Joule heating power required for the actuation (1.6 mW), because the heating spot by the focused laser is more local and has a higher temperature, which makes the heat dissipation through convection more severe. Light can also activate the entire palm structure globally (Fig. 3-8b). Due to the limits of the laser power, we elevated the substrate temperature to 53 °C, so that the laser could heat the whole palm structure beyond the MIT temperature. We note that this base heating would be unnecessary with a more powerful light source, a black absorption layer coated on the structure, or if the structure were grown on or transferred to a thermally insulated substrate.

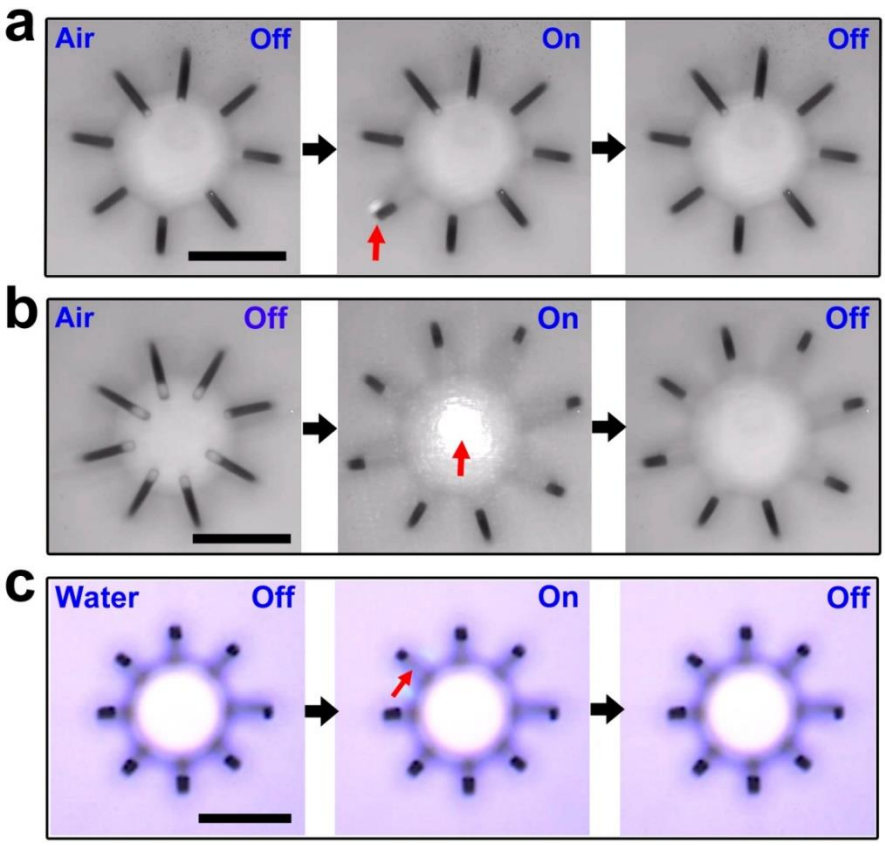

Figure 3-8. Optically activated bimorph microactuators, top view. ***(a)*** *Activating one finger of the palm, and* ***(b)*** *the entire palm structure, with an incident laser. The laser power is 4 mW and substrate temperature is 25 ℃ for (a) and 320 mW and 53 ℃ for (b). Scale bars are 30 μm.* ***(c)*** *Actuating one finger in 40 ℃ water with a 5 mW laser. Scale bar is 50 μm. Red arrows indicate the laser spots. The total finger length is 100 μm for (a) and (b), and 50 μm for (c).*

In addition to working in ambient air, the actuator also works well in aqueous environment. However, because water provides better heat sinking from the structure, more light power or an elevated substrate temperature is required to heat the structure to the phase transition temperature. Fig. 3-8c shows a palm structure is soaked in di-ionized water heated at 40 °C. The actuation in water is stable and the response speed is faster than 17 ms, the frame interval of the camera we used. This is much faster than other mechanisms currently used in aqueous actuation, such as hydrogel swelling and polymer electrostriction [67,68]. Therefore, properly designed Cr/VO_2 microactuators may be used for high-speed microfluidic valves/pumps and reversible molecular cargos in physiological environments.

3.4 Effect of Thermal Anneals

To optimize the bimorph performance, we studied effects of thermal anneal temperature and Cr thickness on the bimorph curvature change (Fig. 3-9). As shown in Fig. 3-9a, an increase in annealing temperature leads to an increase in initial (room-temperature) curvature and a lower beginning temperature of the MIT, possibly attributed to higher built-in stress in bimorphs annealed at higher temperatures. The amount of change in curvature is nearly the same for bimorphs annealed at more than 200 °C, but becomes lower for bimorphs annealed at 150 °C (Fig. 3-9c). It indicates that an anneal temperature > 200 °C is necessary for optimization of the Cr/VO_2 actuator performance.

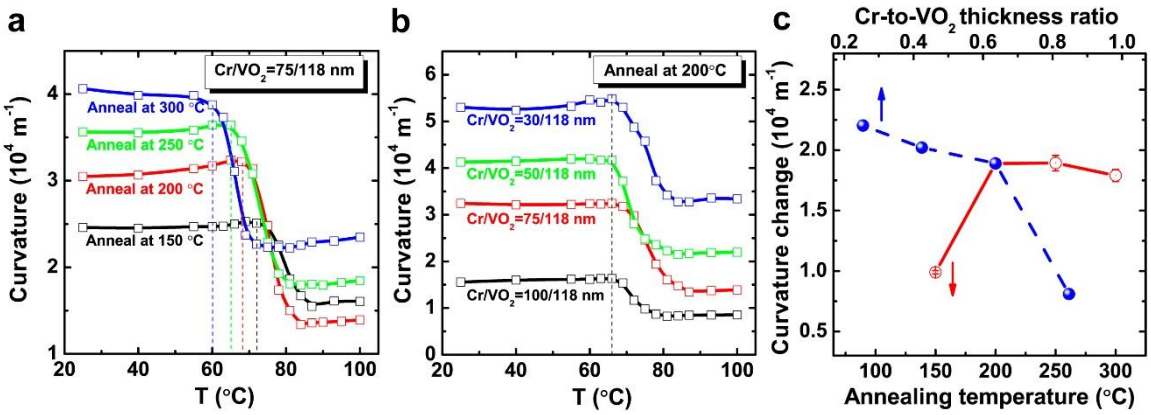

*Figure 3-9. Effects of annealing temperature (**a** and **c**) and Cr thickness (**b** and **c**) on the curvature change Δκ of bimorphs. The data in figure **c** are extracted from Figs. **a** and **b**.*

The thickness of both the active and the clamping layer in bimorph plays a key role on the performance. As shown in Fig. 3-9b and c, the curvature change increases with decreasing Cr thickness, while the beginning MIT temperature of VO_2 remains nearly unchanged. The initial curvature also increases along with the decrease of Cr thickness (Fig. 3-9a), because a thinner Cr layer needs a larger curvature to balance the stress when the VO_2 layer is released from the substrate. These results, suggest that the initial and final curvatures of our microactuators can be tuned by the annealing temperature and the thickness of bimorphs.

3.5 Conclusion

In summary, VO_2-based bimorph microactuators with defined designs are fabricated in batch, which shows giant normalized amplitude over a small temperature

rise, especially at the sub - 100 μm length scale. The large normalized actuation amplitude (*D*/*L*) directly benefits from the giant strain across the phase transition, as well as the nanoscale thickness of the devices. Even if the length of the bimorph actuator scales down to 1 μm, its tip would still displace by more than 10 nm. Using the strain change of $\Delta\varepsilon$ = 0.3% observed in the VO_2 films in this work, a work density as high as 0.63 J/cm^3 is calculated. As a comparison, the work density would be ~ 0.001-0.01 J/cm^3 for the differential thermal expansion actuators (ΔT = 10K) and typical piezoelectric actuators. Therefore, our microactuators offer not only large displacement, but also high work output; consequently, a high actuation force is expected without being compromised by the large displacement.

The microfabrication process developed here is simple, versatile, scalable, and compatible with industry standards. The functionalities of actuation can be further enriched with integrated designs of planar as well as three-dimensional geometries. The diverse range of stimuli that the devices respond to greatly extends the speed and individual addressability of the microactuators. Taken together, a wide range of micro- and nano-scale applications can be envisioned where mechanical motion is needed at high displacement, high force and high speed, such as micro-manipulation, optomechanical and electromechanical switch, microfluidic valving and pumping, drug delivery, heat regulation, and artificial muscles. Development of additional structures, including coils as torsional micromuscles and catapults was explored by the same fabrication process in Ref. [69], but a multitude of designs are yet to be explored.

Chapter 4

Doping of VO_2 with Tungsten

4.1 Background

Vanadium dioxide is not only interesting as a strongly correlated electron material for condensed matter physics studies, but also for a range of device applications surrounding its structural-electronic phase transition. A coupled metal-insulator transition (MIT) and structural transition occur concurrently at T_{MIT} = 67 °C , bringing a monoclinic, insulating phase (I) at low temperatures to a rutile, metallic phase (M) at high temperatures [24,70]. Across the MIT, VO_2 exhibits a drastic change in optical transparency, several orders of magnitude drop in resistivity, and a specimen size change up to 1% [1,2,11,39]. Exploiting these unique characteristics, some of the applications that have been proposed or demonstrated include: optical switch [6], smart window coating [7], Mott transistor [5], memristor [4], strain sensor [8], gas sensor [9], temperature sensor [10], and thermal actuator [15]. To achieve a wide range of functionality in device applications, it is desirable to control the MIT temperature. This chapter shows that 1) we can modify the transition temperature by doping and 2) we can engineer the transition to occur across a broad range of temperatures in a single device by spatially varying the doping concentration. We first study the effect of doping tungsten on the electrical transport properties of VO_2 thin films and then study the second phenomenon in nanowires by controlling the dopant distribution along their length.

VO_2 can be doped with transition metals to alter the critical MIT temperature, T_c, by tens and even hundreds of degrees. In this correlated electron material, excess electrons lower the MIT temperature by increasing the instability of the bandgap that leads to its eventual collapse. By substituting V^{4+} in the lattice, elements with higher oxidation state serve as donors (eg. W^{6+}, Mo^{5+}, Nb^{5+}, Ta^{5+}) and lower the MIT temperature [71–73]. Conversely, elements with lower oxidation state (Cr^{3+}, Al^{3+}, Ti^{3+}, Fe^{3+}, Ga^{3+}) serve as acceptors and raise the MIT temperature [12,74]. Note that the electronic configuration or periodic table group of the dopant atom alone is not sufficient to predict the resulting behavior. For instance, niobium is isoelectronic with

vanadium, yet takes a +5 charge state, resulting in donor-like behavior and lowered MIT temperature. Meanwhile, chromium has one more valence electron than vanadium, suggesting donor behavior, yet doping with it leads to acceptor behavior with a +3 charge and increased MIT temperature.

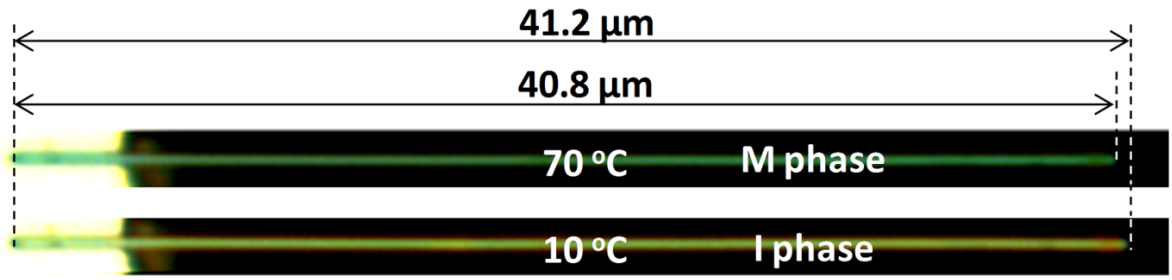

Figure 4-1. Optical images showing length change across the complete phase transition of a $W_xV_{1-x}O_2$ NW with graded W doping. The overall length decreases by ~ 1% between the M and the I phases.

It should be noted that doping at these high concentrations actually form substitutional alloys of $M_xV_{1-x}O_2$, with the transition metal M forming solid solutions with VO_2 for atomic fractions, x up to 0.33, where the tri-rutile phase is formed. Previous XRD studies on bulk samples [75] and thin films [72,76] of $W_xV_{1-x}O_2$ showed only single-phase monoclinic structure (of VO_2), or rutile if the W fraction is high enough to depress the MIT temperature below room temperature (during XRD analysis). It is also important to note that W-doped samples still exhibit the full 1% length contraction, as shown in Fig. 4-1, matching the c-axis length change in undoped VO_2 across the MIT. This is important for actuator applications, as discussed in Chapters 2.4.1 and 4.4.6.

4.2 Origin of Dopant Effect on MIT Temperature

Traditionally, the effect of dopants on the MIT temperature was attributed to the electronic contribution, but recent experiments have shed light onto the importance of the structural perturbation and local stresses introduced near dopant atoms. As described above, additional electrons in VO_2 from thermal excitation or impurities populate the π^*band. This causes an increased split in the $d_{||}$ and $d_{||}^*$ band energies and lowering of the π^*band towards E_f, which eventually leads to bandgap collapse and the transition from insulator to metal [2,77]. The number of excess electrons contributed by dopant atoms help explain this effect on the MIT: Tungsten atoms are the most effective dopant because they ionize to W^{6+} and contribute 2 extra electrons, reducing T_c by 18 –

26K / at. % W. This behavior persists up to 7.5% atomic fraction W, where the material remains metallic at ground state, with little remanent MIT behavior; the MIT reappears at 10% W, rising with a positive slope, dT/dx(W) until the trirutile phase at 33% W [78]. Meanwhile, molybdenum [79] and niobium [73] dopants reach only the +5 oxidation state, contributing only 1 extra electron and suppressing T_c by half as much (7.5 – 15K / % Mo or Nb). The extra electrons reduce adjacent vanadium atoms and localize at the V^{3+} sites, which is supported by structural characterization. Magnetization and X-ray absorption fine structure (EXAFS) investigations by Tang [80] found tungsten-doped VO_2 bulk samples to have only substitutional W^{6+} atoms, forming adjacent W^{6+}-V^{3+} and V^{4+}-V^{3+}pairs by charge compensation. Similarly, Takami [76] found only W^{6+} species using x-ray photoemission spectroscopy (XPS) on doped thin films.

Additional evidence of the electronic doping effect is presented by MIT temperature depression occurs for both 1) additional electrons from isovalent Ti^{4+}, due to unequal electron sharing and 2) substituting oxygen with lower-valent fluorine F^-, which requires fewer electrons for bonding [81]. When fluorine substitutes oxygen in the lattice or Ti substitutes V, more electrons populate the vanadium d bands, which leads to destabilization of the bandgap and eventual transition to metallic rutile state. In addition to chemical modification of the electronic occupation to alter the phase transition dynamics, electrostatic gating of VO_2 has also been successfully demonstrated, highlighting the function of optical and electrical devices based on VO_2.

Several experimentalists including Takami and Rakotoniaina [82] include simple modeling to show that stresses introduced by the larger W ion are *insufficient* to cause appreciable MIT temperature shift. From Shannon's the cation bond lengths in oxides [83], the ionic radius of W^{6+} is 60 Å, which is 3.4% larger than V^{4+} at 58 Å. However, after projecting the length differences along the crystal directions, and averaging for a tungsten dopant composition of 1%, the authors estimate the stress within the crystal to be 0.12 – 0.3 GPa. This stress is insufficient to cause significant depression of the MIT temperature; from the Clausius-Clapeyron relation for a 1-Dimensional transformation:

$$\frac{dT_c}{d\sigma} = \frac{\epsilon_0 T_c^0}{\Delta H} \tag{4.1}$$

We can deduce the change in the transition temperature, ΔT_c with knowledge of the latent heat (ΔH= 5kJ/mol), transformation strain (ϵ_0= 1%) along the c-axis, and the unstrained transition temperature (T_c^0= 340K). Both Takami and Rakotoniaina reference hydrostatic experiments, which tend to underestimate the influence of structural change by smearing the pressure isotropically, and most importantly, leads to ΔT_c of the

wrong sign. With the 1D Clausius-Clapeyron relation in Equation (4.1), I estimate T_c to decrease by 3.7 K given a compressive stress of 0.3 GPa. This is much higher than Takami's estimate of ΔT_c (0.24 K) and Rakotoniaina's (0.6 K) but still much less than the experimental result of 18-26K decrease resulting from 1% W-doping in VO_2. On the other hand, using only the local stress environment around the dopant, without averaging for concentration, results in an overestimate of the temperature reduction effect. Therefore, the MIT temperature depression is best described by the electronic doping effect, where greater charge transfer causes greater ΔT_c.

4.3 Tungsten-doped VO_2 thin films

By mixing WO_2 and VO_2 powders in the correct atomic ratios, I formed $W_xV_{1-x}O_2$ PLD targets with W fraction of 1%, 2%, 4% and 8%. The powders were thoroughly mixed and formed into dense targets with a cold isostatic press. Even though the targets were prepared with a nominal W fraction, the cation stoichiometry in the final film may vary, depending on laser fluence [84], oxygen pressure [85–87] and target-substrate distance [88,89]. As in sputtering, the background gas mixture is extremely important to the film characteristics, and affects the transit of ions from the target towards the substrate. A known drawback of PLD is the difficulty in achieving stoichiometry uniformity across a large area. This problem is especially pronounced when the masses of the elements in the target differ greatly, causing scattering at different rates [90]. This is the case for W and V, which have a masses of 184 and 51 amu respectively, meaning films will have a higher W/V ratio closer to the center of the film or laser spot, since heavier W experiences less lateral scattering through the background oxygen gas. However, these $W_xV_{1-x}O_2$ films were small, under 1 cm x 1cm in size, so the stoichiometry of the films were spatially uniform, as determined by RBS.

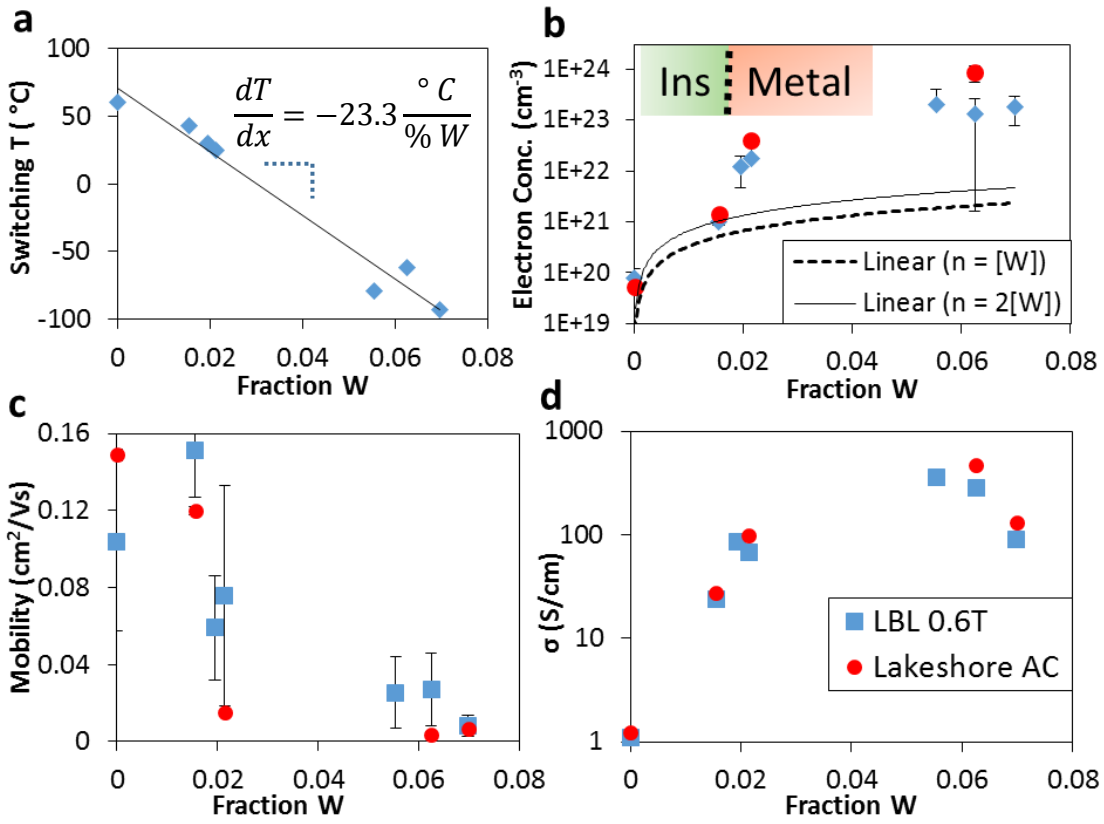

Figure 4-2. MIT switching temperature T_C and transport properties vs. tungsten fraction of WVO_2 films. **b-d)** Electrical transport properties measured by AC and DC hall effect setups at 300K. The colored inset in **b)** indicates the phase at room temperature (insulating at < 2% W and metallic above this doping level). We acknowledge the assistance of Dr. Jeffery Lindemuth and Lakeshore Cryogenics for AC Hall effect measurements.

$W_xV_{1-x}O_2$ films were grown in the with tungsten fraction x up to 7%, and showed the expected linear decrease in T_c, as shown in Fig. 4-2a. These critical transition temperatures were measured by taking resistance vs. temperature plots for each sample, and selecting the halfway point between T_{up} and T_{down}, the temperatures for the insulator-to-metal and metal-to-insulator transitions, respectively. The rest of Fig. 4-2 shows the electrical transport properties of these films, measured by Hall effect in both DC and AC configurations. The very low mobility (<0.2 cm^2/Vs) of VO_2 films is near the detection limit of the DC hall effect setup at LBL, and is expected to be even lower for doped films due to Coulomb scattering by ionized impurities. Therefore, we collect

the AC Hall voltage in response to a time-varying magnetic field to determine mobility with higher precision.

As the tungsten doping of the VO_2 film increases from undoped to 7 percent, the electron mobility drops to 6.5×10^{-3} cm^2/Vs. This extremely low mobility approaches values reported for TiO2, in the range of. Previous studies of undoped VO_2 in thinfilm and single-crystal form reveal that the mobility does not change considerably between the insulating and conducting phases [74,91,92]. Thus, we attribute the conductivity change across the phase transition to be primarily due to change in carrier concentration. Figure 4-2b shows the room temperature carrier concentration rises from 5×10^{19} cm^{-3} when undoped to 8×10^{24} cm^{-3} at a W fraction of 6.5%. As each sample has a different T_c, this figure plots the electron concentration for samples at different states along the MIT. We note that a more meaningful comparison would be between samples all in a fully insulating phase, or all fully metallic, rather than at different points along the transition. The solid and dotted lines in Fig. 4-2b indicate the expected concentration if each dopant W atom contributes 1 or 2 excess electrons to the insulating phase. We note that these results assume a single-band model for conduction; we group all carriers giving rise to the conductivity into one band and carrier type, and compute the overall mobility for this group. It may be the case that this picture does not suffice due to the complex correlated nature of conduction in vanadium dioxide.

Synthesizing thin films with a graded tungsten doping level may be useful to broaden the MIT transformation across a range of temperatures. This feature is explored in the next section within nanowires, but could also be achieved in thin films across their thickness. The film could be grown in multiple layers, with targets of different W/V ratio. A change in film composition is also expected if the target-substrate distance is slowly varied during growth, due to the scattering effects previously discussed. If alternating layers of pure VO_2 are used in between WVO_2 layers, we expect some interdiffusion due to the high growth temperature of the PLD system (500 – 600 °C). A few of these heterostructure films were grown, but were not studied in depth. This may be an interesting source for future studies and applications.

4.4 Axially Graded-Doped Nanowires

4.4.1 Motivation – Widen Operating Region

Among previous applications of VO_2, including optical and electrical switches, and thermal actuators, the functionality occurs only within a very narrow temperature window around T_{MIT}, because the phase transition is first-order and occurs abruptly only near T_{MIT} = 67 °C. Doping of transition metals into VO_2 is widely used to tune the T_{MIT} to serve application-specific needs, but it simply shifts this abrupt transition behavior to another temperature. As discussed previously, T_{MIT} can be decreased by substituting V^{4+} with high-oxidation state atoms like W^{6+}, Mo^{6+}, and Nb^{5+} [44,82,93–98]. Likewise, T_{MIT} can be increased by substituting lower-oxidation state atoms like Cr^{3+}, Ga^{3+}, and Al^{3+} [12,98,99]. Among these, tungsten (W) is the most effective dopant, enabling precise and wide range control of T_{MIT}, with a nearly linear reduction rate of 18.4 °C/at% for single-crystal VO_2 nanowires [44], 24 °C/at% for polycrystal thin films [93], and 25~26 °C/at% for powder and bulk single crystal [82,94]. However, in all these cases, the W-doping of VO_2 is spatially homogeneous; therefore it simply shifts T_{MIT} to another value, and does not modify the abrupt first-order nature of the MIT. The response temperature is still limited to a very narrow window around the new T_{MIT}, and a responsivity across a wide temperature range is lacking.

In this work, we address this narrow-band limitation by engineering a spatially graded MIT along individual single-crystal VO_2 nanowires (NWs). The VO_2 NWs are axially graded-doped with W, forming $W_xV_{1-x}O_2$ NWs where *x* varies continuously along the NW axis, thus achieving a NW system that supports a MIT responding to a *wide range of activation temperature*, practically analogous to a second order phase transition. The M and I domains evolve gradually along the NW axis, leading to unique characteristics absent in un-doped VO_2: gradual but exceedingly large total changes in optical contrast, electrical resistivity and NW length. Enabled by these characteristics, we propose or demonstrate novel applications in optically readable micro-thermometer, un-cooled infrared bolometer, and bimorph thermal micro-actuator.

4.4.2 Experimental

The graded doped $W_xV_{1-x}O_2$ NWs were synthesized using a vapor transport scheme modified from a previously reported method [100]. V_2O_5 and 20 wt% of WO_2 powder were placed in a quartz boat in the center of a horizontal tube furnace, and

evaporated at 880 °C for 10 min, with Ar as the carrier gas (6.8 sccm) at 4 Torr of pressure. The reaction product was collected at 850 °C on an unpolished quartz substrate from downstream of the evaporated sources. The mechanism of axially graded doping of W in the VO_2 NWs is not yet fully understood, but a tentative explanation is given in the Supporting Information. The morphology, crystal structure, crystal orientation, and doping level of these NWs were characterized by optical microscopy, scanning electron microscopy (SEM), transmission electron microscopy, Raman spectroscopy, and energy dispersive x-ray spectroscopy in SEM.

In order to measure the electrical properties in an unstrained state, we used suspended, flexural micro-pads to make electrical devices. Electrically conductive Pt lines were coated on the suspended pads and arms. An individual as-grown NW was transferred between two suspended, parallel pads, and Pt was deposited onto both ends of the NW using focused ion beam for good electrical contact with the pads. To make Cr/NW bimorph micro-actuators, Cr layers were deposited onto one side of graded doped $W_xV_{1-x}O_2$ NWs by electron-beam evaporation with a deposition rate of 0.2 nm/sec. The micro-actuators always bend toward Cr layer due to built-in stress between the Cr and the NW during the Cr evaporation. The sample temperature was controlled by global heating/cooling of the entire device with a ramping rate of 2.5 °C/min, using an electrical micro-heater combined with a resistive temperature sensor.

4.4.3 Synthesis and Structural Characterization

The graded doped $W_xV_{1-x}O_2$ NWs were grown by the vapor transport method as schematically shown in Figure 4-3a, similar to previous growth method for high-density un-doped VO_2 wires [100], except that WO_2 powder was added as W doping source. In the downstream, NWs were produced on an unpolished quartz substrate, as shown in Figure 4-3b. The as-synthesized NWs free stand randomly on the substrate, and the lengths are in the range of 5 to 50 μm. Figure 4-3c and d show optical image and scanning electron microscopic (SEM) image of a typical NW (~32 μm in length and ~210 nm in width) cantilevered from the edge of a substrate. Most notably, at room temperature, the M and I phases coexist axially within the single NW. It is well known that these two phases are clearly distinguishable by their optical reflection under white light illumination: dark domains (green in this work) are the M phase and the bright domain (yellow in this work) is the I phase [39]. Almost all NWs have three distinctive domains: M phase at both tips and I phase in the middle part. These phases were cross checked by transmission electron microscope (TEM). The selected area electron diffraction (SAED) pattern of the NW (Figure 4-3e and f) show that the dark green part

is indeed M phase (rutile, $P4_2/mnm$), while the bright yellow part is I phase (monoclinic, $P2_1/c$). The single-crystallinity of the NW is confirmed by the fact that the SAED pattern. Therefore, it is clear that the tips of the NWs are W-doped more heavily than the middle part, such that the T_{MIT} at the tips is below room temperature, while at the middle part is above.

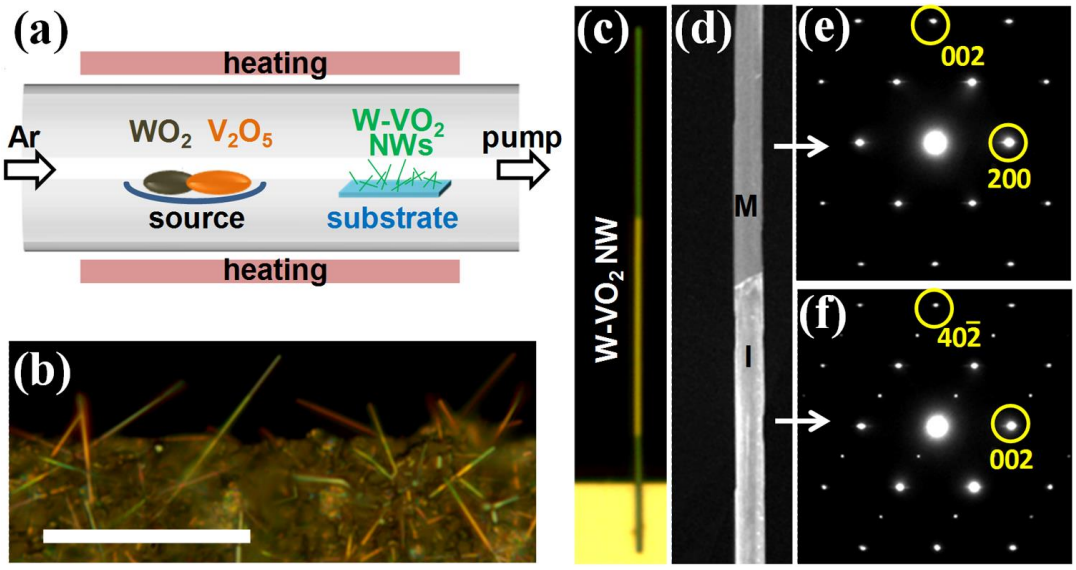

Figure 4-3. Axially Graded WVO_2 NW Synthesis and TEM. ***(a)*** *Schematic of growing the graded doped $W_xV_{1-x}O_2$ NWs.* ***(b)*** *Optical image of an as-grown sample at room temperature. Scale bar is 20 µm. (c-d) Optical* ***(c)*** *and SEM* ***(d)*** *image of a typical graded doped $W_xV_{1-x}O_2$ NW (length: ~32 µm, and width: ~210 nm). The NW was transferred onto a Si substrate from the as-grown substrate. Optical images were taken using un-polarized white light. Visual color of the NW is a combined result of multiple factors including illumination light spectrum and resolution limit of the optics. (e-f) Electron diffraction pattern taken from the dark green region* ***(e)*** *and bright yellow region* ***(f)****. The patterns are indexed to rutile (metallic phase, M) and monoclinic (insulating phase, I) structure of VO_2, using rutile-[010] and monoclinic-[010] zone axis, respectively.*

In the optical and TEM imaging above, the NW is free-standing. This is important in order to probe the intrinsic phase transition and domain structure. It has been shown that under strain, the MIT temperature and the M-I domain structure of VO_2 appear different from free-standing VO_2 [11,39]. A free-standing VO_2 NW or a free-standing uniformly W-doped VO_2 NW undergoes the MIT abruptly when temperature is raised across its T_{MIT} [11,44]. However, when the same NW is assembled into a two-probe device where the two ends (and only the two ends) are firmly clamped on a rigid substrate by electrodes, the M phase grows gradually along the NW as a function of temperature [64]. This is because this is the minimum-energy M/I domain structure of

the NW when an additional elastic energy term is introduced by strain accumulated in such an end-end clamped configuration [64,101]. Therefore, externally imposed strain should be avoided when the intrinsic MIT behavior is to be characterized.

To eliminate strain accumulation in measuring the electrical resistance of these NWs, we use suspended micro-device pads typically used for isolated thermal transport measurements [102]; here the pads are conductive and suspended by long flexural arms, serving as two electrical contacts to the NW. Unlike ordinary NW devices firmly clamped on solid substrates, however, in our case the suspended pads are free to move, and thus the NW is free to shrink or elongate to avoid axial strain accumulation. A single NW was transferred to bridging the two pads (inset of Fig. 4-5a), and Pt was deposited to bond the NW onto the pads using Focused Ion Beam, as shown in Fig. 4-4c.

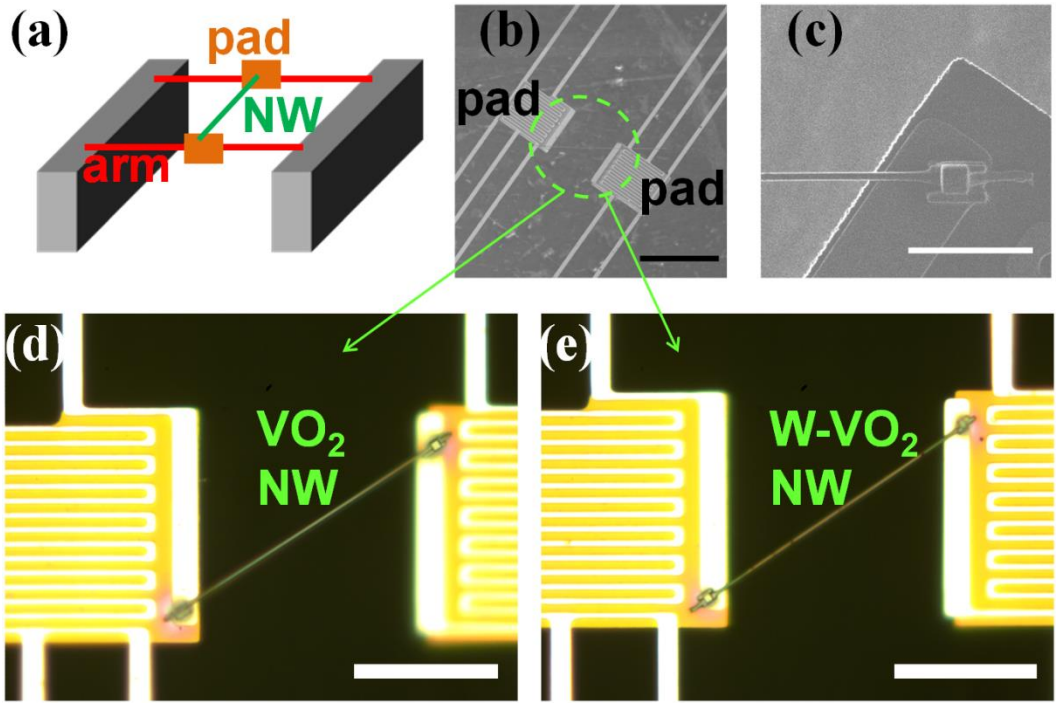

Figure 4-4. Suspended pad based microdevice used for electrical measurements. (a) Schematic of the device structure, (b) SEM images showing the top view of the device, (c) FIB-deposited platinum to bond the NW onto the pad, (d) optical images of the fabricated devices with an undoped VO_2 NW, and (e) a graded doped WVO_2 NW. Scale bars: (b) 50 µm, (c) 5 µm, (d) 20 µm, (e) 20 µm.

More than 5 each of $W_xV_{1-x}O_2$ and un-doped VO_2 devices were fabricated in this way. The typical length and width of NWs is ~40 µm and ~300 nm, respectively. All

devices showed linear *I-V* curves, indicating ohmic contacts. Figure 4-5a plots a typical resistance-temperature curve of a graded doped $W_xV_{1-x}O_2$ NW and an un-doped VO_2 NW. Here the temperature ramping rate is controlled to be very slow (< 2.5 °C / min), to eliminate kinetic effects. The un-doped VO_2 NW shows the expected [11] sharp resistance switching around 67 °C with a ~2 °C hysteresis. We note that the T_{MIT} may be also affected by chemical non-stoichiometry of the NW [26]. In stark contrast, the resistance of the graded doped $W_xV_{1-x}O_2$ NW decreases gradually from room temperature to 60 °C without the typical abrupt resistance switching. This resistance behavior results in an exceedingly large temperature coefficient of resistivity (TCR) of -(12 ± 2) % / K. The TCR is defined as $(1/\rho)(d\rho/dT) = d(\ln\rho)/dT$, where ρ is resistivity. The TCR is a key parameter for many thermal sensing applications such as electrical thermometer and infrared bolometer (see below).

The origin of this gradual MIT occurring over a ΔT of 30 °C can be understood from the concurrently taken optical images of the graded doped NW. As shown in Figure 4-5b, with the increase in temperature, the M phase grows out of the two ends of the NW, followed by a progressive invasion into the I phase toward the middle of the NW, and the entire NW turns into a single M phase at 55~60 °C. Such a domain behavior was observed from all graded W-doped VO_2 NWs, but not from the un-doped VO_2 NWs; Moreover, even when the NW was cantilevered at one end from the edge of a heated substrate, the M phase grew from both the root and the tip of the NW (Figure 4-6), therefore we rule out the possibility that temperature gradient along the NW axis might cause this domain behavior.

The axially progressed M/I domain wall means that the local T_{MIT} itself is encoded by the growth, and varies gradually along the axis, from heavily W-doped tips to a lightly W-doped center. The coexisting M and I phases along a single NW is further confirmed by their micro-Raman spectra in Fig. 4-5c. Figure 4-5d shows axially varying T_{MIT} from the center (position l = 0) to one of the tips (l = 1) of a graded doped $W_xV_{1-x}O_2$ NW, and the W doping fraction measured along the NW axis by energy dispersive x-ray spectroscopy (EDS). The EDS results verify that the NW is graded W-doped and the doping level increases from 1.0 at% at l = 0 to 2.6 at% at l = 1. The measured W doping level agrees well with the predicted W fraction (also plotted in Fig. 4-5d), converted from the measured T_{MIT} using the T_{MIT} reduction rate, -18.4 °C/at% of W, reported from homogeneously W-doped VO_2 NWs [44].

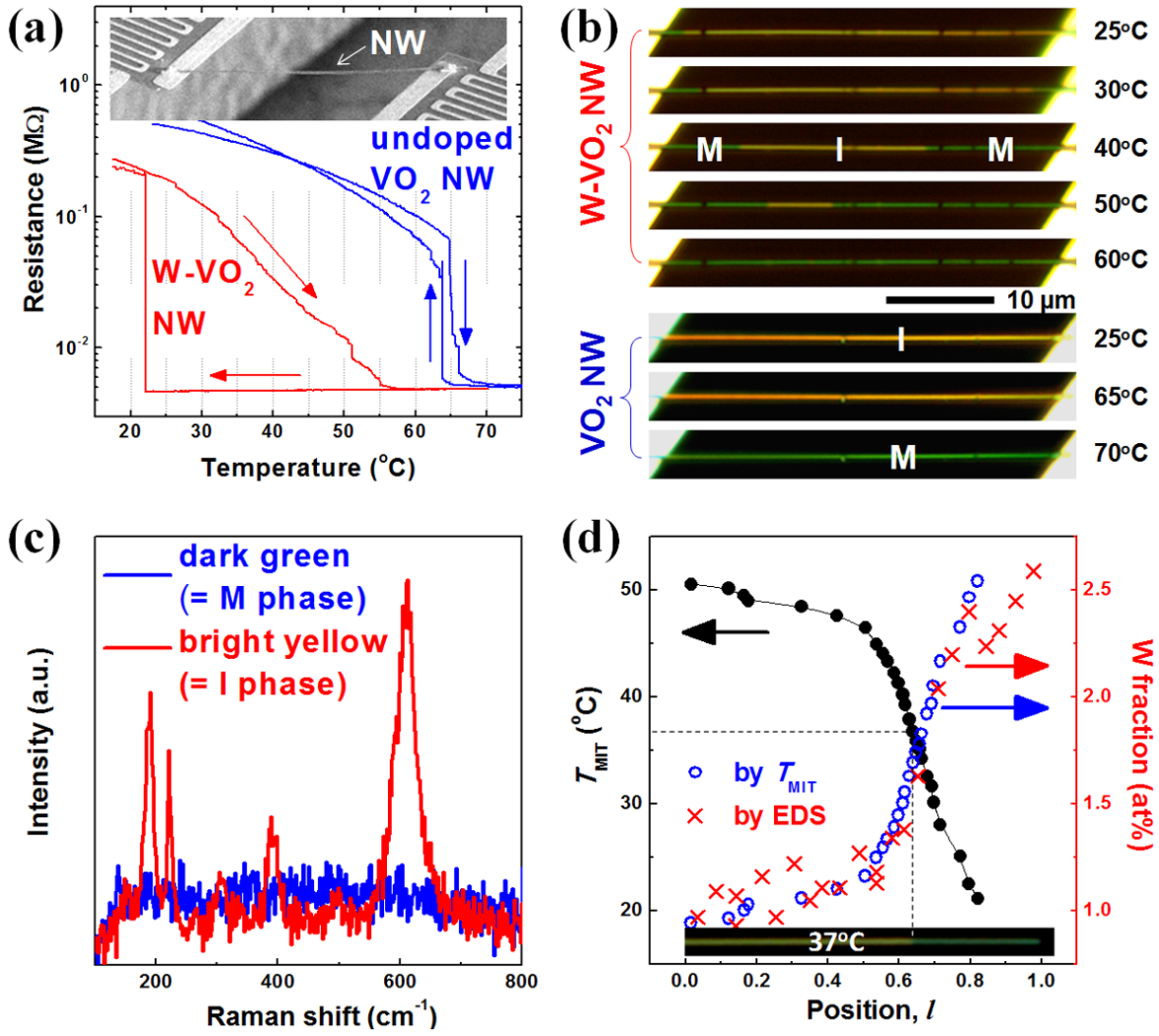

Figure 4-5. Graded doping and gradual MIT. (a) Temperature dependence of resistance of a graded doped $W_xV_{1-x}O_2$ NW and an undoped VO_2 NW. The resistance was measured on suspended pads (Inset) to minimize strain. (b) Optical images of the graded doped $W_xV_{1-x}O_2$ NW device (upper panel) and the undoped VO_2 NW device (lower panel), at various temperatures during heating up. (c) Raman spectra taken from the dark part and the bright part of the graded doped $W_xV_{1-x}O_2$ NW. The peaks for the bright part are identified as I phase of VO_2 (monoclinic). There are no peaks related to other stoichiometries of vanadium oxides. (d) Local MIT temperature (left axis) and W fraction (right axis). The latter was measured by EDS and calculated from the measured T_{MIT}, respectively. The horizontal axis is position along the graded doped nanowire from the center (l = 0) to the tip (l = 1). l=1 corresponds to 20 μm. The inset shows optical image of the analyzed NW at 37 °C as an example.

We note that when the graded-doped $W_xV_{1-x}O_2$ NWs are cooled down from high temperatures where the NW is in full M state, they always show a large hysteresis as in

Fig. 4-5a. On the other hand, when they are cooled down from an M / I / M domain configuration at intermediate temperatures, they show only a small (less than 5 °C) hysteresis followed by a gradual transition back to the full I state. This is an effect of large super-cooling because of the lack of nucleation site for the transition starting from the full M state. As shown in our previous work [103], the M / I domain wall or twin walls in VO_2 can serve as sites to seed the growth of new phase, thus eliminate super-heating or super-cooling during the MIT. However, when the NW is fully in the M state, an M / I wall is absent, and the tetragonal crystal structure of the M-phase also precludes the possibility of structural twinning. Therefore the system has to undergo a large super-cooling before the first I domain appears. This is not the case for the transition starting from an M / I / M state where the M / I domain wall acts as the seed for growth of new phase. Therefore, a large kinetic asymmetry with a strong super-cooling is seen in the MIT of these NWs.

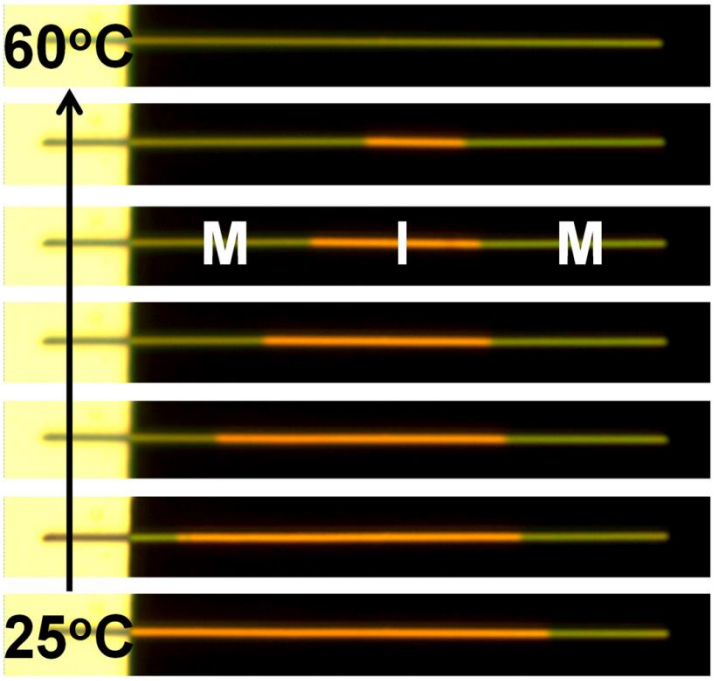

Figure 4-6. Optical images of graded-doped WVO_2 NW at several temperatures. The progressive M domain growth with increasing temperature shows the broadened MIT across a range of temperatures and locations. The wire length is ~35 µm.

Due to the stark color contrast between the M and I domains, the M/I domain wall can be easily resolved with an optical microscope. Its axial progress with temperature rise naturally offers a single-NW micro-thermometer that can be optically

read out. Optically readable micro-thermometers have been demonstrated utilizing temperature-sensitive light emission of quantum dots [104] or molecules [105]. However, in those cases an excitation light source and a spectrometer are needed to record and spectrally resolve the emitted light. In our case by a rapid, simple optical imaging of the M/I domain wall position along the NW, local temperature can be determined after proper calibration. Moreover, the temperature range over which the NW thermometer works is between room temperature and ~ 60 °C, a temperature range of special importance in biology and microfluidics. We note that a un-doped VO_2 NW can also support a axially gradual MIT when it is firmly clamped at its two ends on a rigid substrate [64]. However, the requirement of end clamping is undesired for application, while in our case this is achieved with W doping.

4.4.4 Mechanism for W incorporation to achieve the axial doping profile

Our graded doped W-VO_2 NWs show "V"-shape W doping profile along the axial direction, as sketched in Fig. 4-7a. The mechanism of axially graded doping of W in the VO_2 NWs is not fully understood, but a possible explanation is given as follows. First, we note that these NWs were grown catalyst-free [106] on a substrate with rough surface geometry to facilitate the dense growth of free-standing NWs, as shown schematically in Fig. 4-7b [100]. If a (quasi)-flat substrate (eg. thermal oxide, SiO2 on Si) is used, most of the NWs are grown firmly clamped onto, or half-embedded into the surface, imposing large strain to the NWs and influencing their MIT behavior [39]. Liberating the NWs from the substrate by chemical etch is possible, but results in low yield and may damage the surface of the NWs.

Secondly, in Fig. 4-7c we show a few possible temperature profiles we tried for the growth. In route B, the sample was taken out of the tube furnace abruptly (within ~ seconds) after the 880^{o}C growth. In all other routes, the temperature ramping up and down processes were on the order of 50^{o}C/min, and were controlled by the temperature controller of the furnace. We observed that i) No NWs were grown at all in route E; ii) NWs were grown in route A, B, C and D, and surprisingly they all yielded NWs with similar lengths; iii) all A, B, C and D growths led to "V"-shape W doping in VO_2 NWs; and iv) the average W doping levels were the highest for route A and the lowest for D.

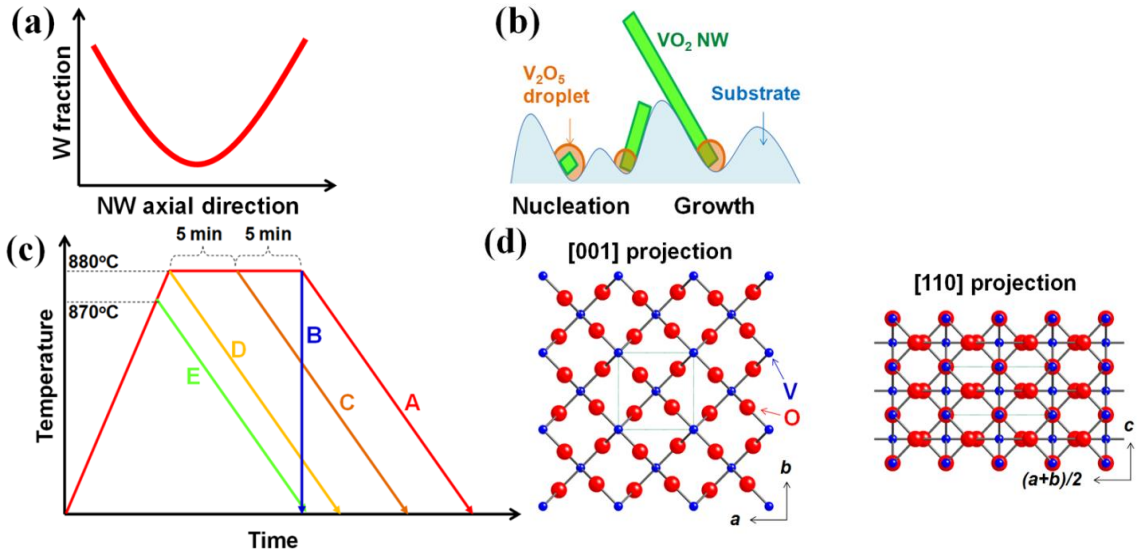

Figure 4-7. ***(a)*** *A sketch showing the typical W fraction along the graded W-doped VO_2 NW.* ***(b)*** *Mechanism of growing free-standing VO_2 NWs on rough quartz substrates using V_2O_5 powder as the source. At the growth temperature when VO_2 nucleates and grows out of the V_2O_5 droplet, owing to capillary force, the VO_2 NWs are initially bound onto the local substrate surface. However, at later times, following the surface roughness, the NWs grow out of the surface plane and become free-standing.* ***(c)*** *A schematic showing various temperature profiles we tried for the NW synthesis.* ***(d)*** *The structural model of the VO_2 rutile (M phase); [001] projection (viewed along the cR axis), and [110] projection.*

We now discuss two possible W doping mechanisms: 1) W incorporation during the NW growth, and 2) W doping by axial diffusion after the NW growth.

In the first picture, the W atoms are incorporated into the VO_2 NW while the NW is forming along its length. Because tungsten oxide has different vapor pressure from that of V_2O_5, it is possible that W incorporation is more efficient at relative low temperatures slightly below 880°C. In this way both the root and the tip of the VO_2 NW were heavily doped with W, because they are the parts of the NW that formed at slightly lower temperatures (i.e., during the temperature ramping up and ramping down processes).

However, our observation iii above shows that the NWs were still doped as the "V"-shape W profile even in absence of the temperature ramping down process (route B). This is contradicting with the idea that W atoms were incorporated during the NW formation. This idea is also inconsistent with the observation ii. We therefore propose:

In the second doping model, the VO_2 NWs were rapidly grown, and then W diffuses along the axis of the NW from the two ends towards the center, fed by the tungsten oxide vapor and assisted by the high temperature. This is consistent with all the observations above. V_2O_5 micro-droplets are transported to the substrate at high temperatures, and an un-doped VO_2 NW rapidly forms from each liquid V_2O_5 droplet when temperature approaches 880°C. This NW stops to grow when its V_2O_5 droplet is depleted even if the V_2O_5 vapor supply continues; therefore, longer growth time at 880°C (from routes D to C to A) does not grow longer NWs. The formation of VO_2 NW is too fast for significant amount of W to be doped in, therefore, these rapidly formed VO_2 NWs are nominally un-doped or only lightly doped. Instead, W atoms axially diffuse from the two ends of each already-grown VO_2 NW toward the center, resulting in a "V"-shape W doping profile. This diffusion process is fed by the abundant tungsten oxide vapor and assisted by the high temperature of the furnace.

The diffusion is mostly axial instead of radial along the NWs because of diffusion anisotropy. The high-temperature crystal structure (rutile phase) of the VO_2 NWs has large openings along the NW axis (c_R) direction acting as diffusion channels for the W atoms, but the V and O atoms are much more closely packed in the NW radial direction (i.e., directions perpendicular to c_R) (Fig. 4-7d); this allows a much easier axial diffusion than radial diffusion. In TiO_2 which has a similar rutile structure, it has been reported that some cations diffuse more easily along the c-direction channels [107–109]. Such quasi-one-dimensional diffusion warrants further investigation and may be used to achieve other novel structures.

4.4.5 Application of High Thermal Coefficient of Resistance for Infrared Detection

Now we turn to another potential application, infrared detection. For electromagnetic radiation in the far-infrared spectral range, conventional p-n junction based photo-detectors do not work because the infrared light energy is below its bandgap. In this case bolometers are typically used, which measure the incident infrared light intensity by monitoring the resistance (R) change of an infrared-sensing material. The material absorbs the infrared light and heats up, thus lowering its R. Typical bolometers are cooled by liquid helium to reduce optical and electrical noises, which add undesired cost, volume and weight. For un-cooled bolometers, high performance requires the following properties from the sensing material: 1) strong infrared absorption to maximize efficiency, 2) a high temperature coefficient of resistance (TCR) for maximum sensitivity, and 3) a low resistivity (ρ) to minimize thermal noise and Joule heating. Achieving a high TCR and simultaneously low ρ is a challenge for

semiconductors because they are mutually exclusive: $\rho = \rho_0 \exp(E_a/k_B T)$, and $\mathrm{TCR} = \left(\frac{1}{\rho}\right)\left(\frac{d\rho}{dT}\right) = -E_a/k_B T^2$, where E_a is the thermal activation energy of ρ. Therefore a high TCR typically correlates with a high ρ.

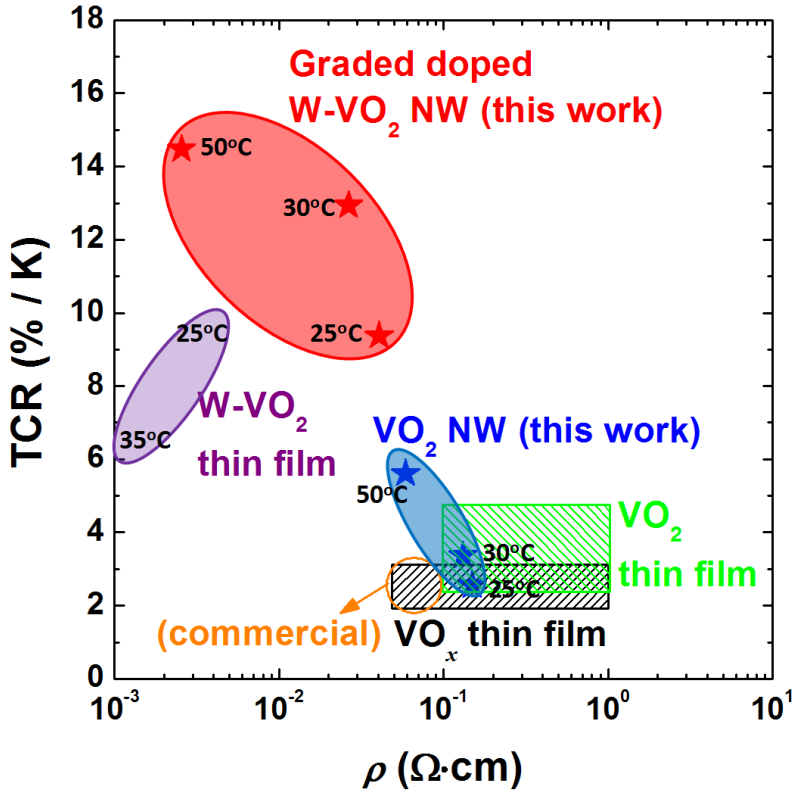

Figure 4-8. Temperature coefficient of resistance for VO_X materials. Temperature coefficient of resistance (TCR) versus resistivity of various sensing materials for un-cooled infrared bolometer. The graded doped $W_xV_{1-x}O_2$ NW is compared with VO_x thin films [110–114], VO_2 thin films [110,111,115,116], W-doped VO_2 (1.5 at%) thin film [96], and VO_2 NW (this work). The stars are the data points measured in this work. An ideal bolometer material prefers high TCR and low ρ.

VO_2 thin films have a relatively high TCR of 2 ~ 5% / K in the I phase, but the high ρ of 0.1 ~ 1 Ω·cm makes them unsuitable for uncooled bolometry applications [110,111]. Moreover, its abrupt, first-order MIT is considered a nuisance that needs to be avoided, because it introduces high non-linearity in the sensing response. Other vanadium oxide (VO_x) thin films with various stoichiometries free of MIT have been used as commercial bolometer sensing material, taking advantage of their strong infrared absorption, relatively high TCR (2 ~ 3% / K) and low ρ (0.05 ~ 0.1 Ω·cm) [110,111]. Our graded W-doped VO_2 offers a new, superior bolometer material by exploiting the MIT, as opposed

to avoiding it. First of all, VO_2 and W-doped VO_2 are intrinsically strongly absorptive in the far-infrared region, especially in the M phase [92,117]. Figure 4-8 plots the TCR and ρ of the graded doped $W_xV_{1-x}O_2$ NWs compared to VO_x thin films that are currently used as the working material for un-cooled bolometers. The graded doped $W_xV_{1-x}O_2$ NWs exhibit an exceptionally high TCR on the order of 10% / K, together with a low ρ between 0.001 and 0.1 Ω·cm. These two parameters are superior to VO_2 thin films [110,111,115,116], VO_x thin films [110–114], $W_xV_{1-x}O_2$ (x=0.015) thin films [96], and un-doped VO_2 NW. Therefore, the spatially (and thermally) progressing MIT of graded W-doped VO_2 presents a new candidate for prospective bolometer material by offering ~5 times higher TCR simultaneously with a lower ρ than commercially used bolometer materials. Compared to polycrystal VO_x thin films, the graded doped single-crystal $W_xV_{1-x}O_2$ may have other advantages: 1) low $1/f$ noise (another main factor affecting device sensitivity) because of its single-crystallinity and thus much fewer domain/grain boundaries [118]; and 2) high effective infrared absorption due to the existence of the M phase, featuring an absorption coefficient 5 to 100 times higher than in the I phase in the infrared range of wavelength > ~ 8 μm [119,120].

4.4.6 Application as Broadband Thermal Actuator

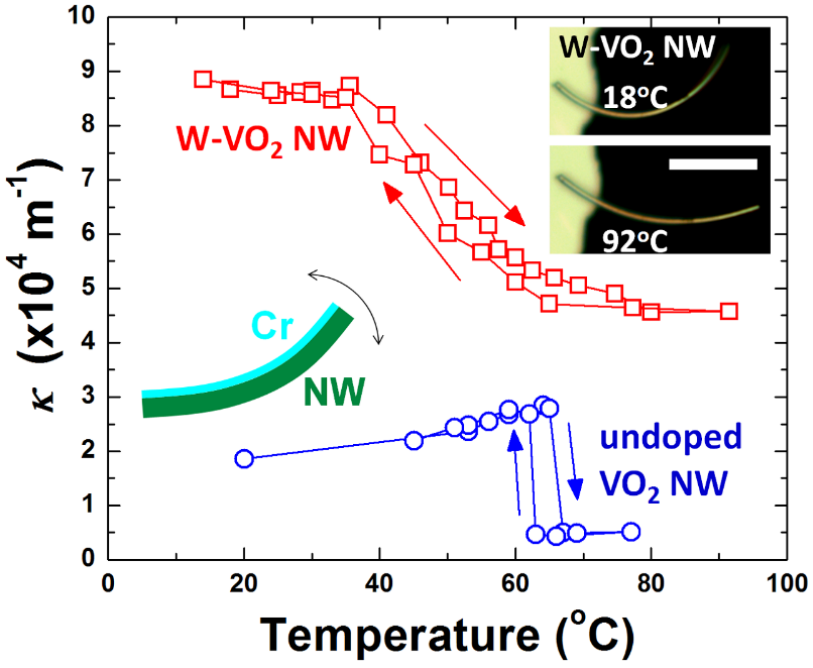

Figure 4-9. Temperature dependence of bending curvature of two bimorph thermal actuators, Cr on a graded doped $W_xV_{1-x}O_2$ NW, and Cr on a un-doped VO_2 NW. Upper inset shows optical images of the $W_xV_{1-x}O_2$ -based actuator (scale bar: 10 μm) at 18 °C and 92 °C, and lower inset shows a scheme of the bimorph structure.

The axially engineered MIT in the graded doped $W_xV_{1-x}O_2$ NWs also enables broad-range thermal micro-actuators. As described in Chapter 2, this actuation is driven by the spontaneous strain in the structural phase transition, ε ~ 1%, along the rutile c-axis (c_R), which accompanies the MIT in VO_2 [14]. In NWs where the wire axis is always along c_R, the strain causes an abrupt shrinkage of the NW length by 1%. To use this effect in thermal micro-actuators in a bending configuration, we mechanically couple the VO_2 NW with an inactive layer forming a bimorph. Crossing the MIT, the bimorph bends to high curvatures (κ), and outputs actuation at high force, high amplitude and high speed compared to conventional actuators [14–16,121]. This phase transition based actuation, however, is triggered abruptly near the VO_2 MIT temperature ~67 °C, and does not respond to lower driving temperatures, which limits the operation responsivity, as shown in the blue curve of Fig. 4-9.

We found that W-doping retains the 1% spontaneous strain in VO_2 (Figure 4-1), but the graded doping causes the NW length shrinkage to occur gradually instead of

abruptly. This property offers a way to lower the temperature threshold and broaden the response range of un-doped VO_2 actuators. Figure 4-9 shows the temperature-dependent κ change of a bimorph actuator comprised of a graded doped $W_xV_{1-x}O_2$ NW coupled to a Cr overlayer as shown in the inset. The length and thickness of the NW are ~24 μm and ~250 nm, respectively. We coated ~ 90 nm of Cr onto one side of the NW, because the maximum curvature change ($\Delta\kappa$) of a Cr/VO_2 bimorph is expected at a thickness ratio of ~ 0.37 [16]. In contrast to the Cr/VO_2 bimorph, the κ of the Cr/$W_xV_{1-x}O_2$ changes gradually over a temperature range of 35 °C ~ 80 °C with a rate $\Delta\kappa/\Delta T$ of ~900 $m^{-1}\cdot K^{-1}$, leading to an overall $\Delta\kappa$ of ~ 4×10^4 m^{-1}. This wider range of working temperature, gradual κ change, and smaller $\Delta\kappa/dT$ (compared to Cr/VO_2 bimorph) allows precise control of the actuation displacement, while outputting similarly large amplitude of displacement. Moreover, it has been shown [15] that VO_2 provides a high volumetric work density ($Y\varepsilon^2/2$, where Y = 140GPa is the Young's modulus) up to 7 J/cm^3. This allows the Cr/VO_2 bimorph actuator to deliver simultaneously high force and large amplitude in actuation. This work density is comparable to shape memory alloys, more than ten times higher than that of most organic materials and electrostrictive polymers, hundreds of times higher than piezoelectric materials, and three orders of magnitude higher than human muscles [122].

4.5 Conclusion

In summary, we synthesized W-doped VO_2 thin films by PLD from mixed WO_2/VO_2 targets. The tungsten incorporation into the film depends not only on the target stoichiometry, but also on the PLD growth conditions, such as oxygen pressure and target distance. RBS was used to quantify the tungsten cation fraction, which varied from from 0% (undoped) up to 7%. The MIT temperature was determined by measuring the film resistance vs. temperature behavior, and the expected linear decrease with W-doping was verified, with T_C decreasing by 23K / % W. Hall effect measurements revealed the room temperature carrier concentrations increase with doping, while mobility decreased. This agrees with the expected behavior as increased tungsten ionizes to W^{6+} in the lattice, contributing extra electrons to the conduction band, but the ionized impurities also increase Coulombic scattering and decrease electron mobility.

Next, we synthesized W-doped VO_2 nanowires where the doping level is axially graded from the two tips toward the center of the NW. These $W_xV_{1-x}O_2$ NWs exhibit axially graded metal-insulator phase transition and structural transition. Their extremely high temperature coefficient of resistivity combined with the low resistivity make them

a good candidate for far-infrared sensing material in un-cooled bolometers; the high optical contrast between the two phases renders each individual NW an optically readable micro-thermometer; the gradual structural transition allows the operation of bimorph micro-actuators with high amplitude and wide temperature responsivity. We note that the coupled structural-electronic phase transition of VO_2 and $W_xV_{1-x}O_2$ can be activated by a diverse range of external stimuli: heat, electric current [44], strain [11], focused light [15], and electrical field [123,124]. Consequently, the graded doped $W_xV_{1-x}O_2$ NWs may find extensive applications in microscale thermo-opto-electro-mechanical signal transduction and energy conversion.

Chapter 5

Structural Transition-based "Mechanical" Anneal

5.1 Background

The large mechanical strain and significant latent heat of VO_2's structural phase transition potentially provide an avenue for increased defect mobility. If point defects such as vacancies or interstitials were to move and annihilate at high speed due to the structural transition, this could serve as a new method of annealing materials at low temperature. The shape change of the crystal can lead to preferential migration of point defects, with high-volume defects migrating towards regions of low (or negative) strain, while low-volume defects accumulate in regions of higher strain. The presence of strain fields alters the defect equilibrium energies and also changes the activation barriers for defect migration [125], as shown in Fig 5-1. This behavior for point defects has previously been observed near crack tips in steel [126] and in silicon under pressure [127,128]. Time-dependent defect motion under stress can be considered diffusional Nabarro-Herring creep when occurring in bulk crystals [129].

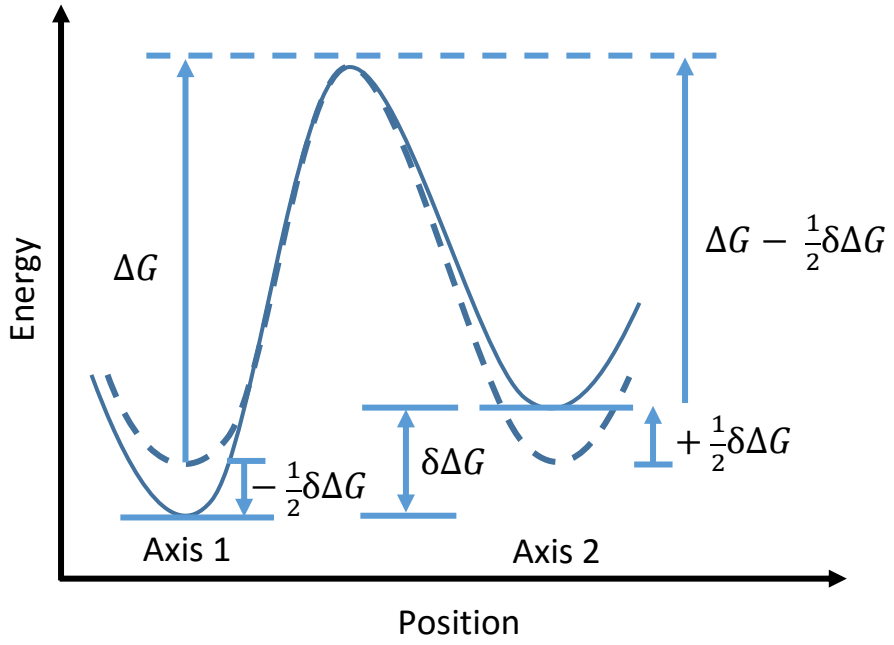

Figure 5-1. Free Energy vs. Position. ΔG represents the energy for migration of a defect (interstitial or substitutional). Modeled after Ref. [130]

Creep deformation that recovers towards the initial shape is termed viscoelasticity, and that resulting in full recovery is termed anelasticity. While creep is generally a high-temperature phenomenon is only appreciable in oxides at a high homologous temperature ($T/T_m > 0.6$), nanostructured materials have shown very high defect diffusivity at much lower temperatures. TiO_2 (rutile) conventionally shows appreciable creep [131] at 1200 °C, nanocrystalline (40nm) TiO_2 displayed diffusional creep under compression in the 600-800 °C range [132]. The enhancement is attributed to high mobilities and low dislocation densities of nanostructured materials, though the high surface area could contribute to greater point defect density.

Likewise, room temperature anelasticity was recently observed in ZnO nanowires [133]. By bending the ZnO wires and holding them for extended periods (10 minutes+), defects diffused under the asymmetric strain gradient, which resulted in an anelastic, gradual shape recovery towards the original shape after the load was removed. This demonstration of the Gorsky effect, where defects move down a chemical potential gradient imposed by strain, is a specialized case of diffusional creep, in which an asymmetric strain exists. Traditionally, the Gorsky effect is displayed in the movement of interstitial hydrogen in bent metal samples, towards tensile regions [134]. In the ZnO system, oxygen vacancies and other low-volume defects migrate towards the

compressed side of a bent nanowire, while larger defects move towards the tensile side. Short-range diffusion of interstitials in response to a strain field is described by Snoek relaxation, where defects move towards positions where the elastic dipoles are orthogonal to those created by the applied strain [130]. When species have very high diffusivities, we can observe more macroscopic behavior as in the case of the Gorsky effect.

The goal of this section is to search for a potential "mechanical" anneal utilizing VO_2's structural phase transition as a means of straining the material at a relatively low temperatures (30 – 70 °C) compared to those conventionally used for annealing (several hundreds of degrees C). If point defects are more mobile in the vicinity of a domain wall, their motion and annihilation could serve as a new means of annealing at low temperature. We explore this possibility by examining the quality of VO_2 thin films and nanowires, subjected to many passages across the phase transition by means of Joule heating, laser absorption, and also mechanical actuation. The last of these opens an avenue of exploration for true room-temperature annealing, relying only on mechanical strain to promote defect motion. Thus any material could potentially be a candidate to test point defect motion under strain. We propose InP nanopillars as a future direction of research for this effect, as 1) the wires provide very high brightness photoluminescence, as a measure of defect quality 2) InP is very stable in air and 3) the moderate piezoelectricity of wurtzite InP could encourage defect motion given the charged nature of point defects.

5.1.1 Role of Domain Wall Energy and Latent Heat

As the MIT progresses through a thin film or nanowire, the movement of the interface or domain wall between the metal and insulator phases may provide some thermal driving force for the motion and recombination of defects. The mismatch of the two crystalline phases (monoclinic and rutile) leads to a large surface energy, γ_{MR}, for the interface, with estimates ranging from 25 mJ/m^2 from measurements of the substrate strain-domain coupling [39] to 30 mJ/m^2 from DFT calculations (rutile free surface energy minus monoclinic free surface) [135,136]. These surface energies, if divided equally among the plane by vanadium atoms correspond to 30 – 36 meV / V atom, which equate to temperature fluctuations of 98 – 180 °C, higher than the MIT temperature. As the domain progresses through the material multiple times, thermal energy is absorbed locally to sustain the surface, but it is released as the interface progresses away, leaving behind a single-domain phase. Along with this extra energy from domain wall motion, the latent heat of the phase transition could also contribute

locally to point defect motion. Assuming the minimum domain size to be the thickness of a unit cell, the latent heat volume energy is as high as 68 mJ/m^2 when dissipated along the phase boundary; this represents an equivalent temperature of 760 °C in the vicinity of the M->I transition.

A different source for point defect motion may be the defects' preferential migration towards or away from metal-insulator interfaces; in $BaTiO_3$ and $CaTiO_3$, oxygen vacancies have been observed to migrate towards ferroelectric domain walls [137,138]. While these domain walls, including twin walls, do not demarcate distinct phases, they often serve as nucleation sites for the ferroelectric-paraelectric transition between tetragonal and cubic phases [139,140]. This behavior is mirrored in ferroelastic domain boundaries in VO_2, where the MIT was observed with polarized microscopy to locally nucleate in the vicinity of these domains [101,103]. Point defect annihilation is only expected to be significant if the appearance of twin walls is not spatially random upon cooling into the monoclinic phase, but linked to the geometry of the structure (be it nanowire or grain in a thin film). Along with the spatial location, it is surmised that repeatedly directed progression of the MIT can reliably push defects into the same direction across many cycles.

We note that enhanced reaction rates were reported around the phase transformation in barium and cesium oxides, termed the Hedvall effect [141,142]. Later studies put this up for debate, with some finding the effect in cement reactions [143], but most explained the observed anomalies as caused by water contamination, leading to unforeseen reactions [144,145]. These results cannot disprove the existence of this effect in VO_2's first order phase transformation, but do cast some doubt as to whether the proposed mechanisms can provide significant enhancements in point defect motion.

It is important to note that the process of cycling across the phase transition is more energy-intensive than a 'conventional anneal' holding the temperature constant above the phase transition. This is due to the aforementioned surface energy and latent heat being released upon cooling and escaping into the environment. Thus, any potential enhancement in point defect motion by a cyclic anneal must account for this additional input energy. Nonetheless, any observation of accelerated point defect motion at these low temperatures (below 100 °C) would be extremely interesting.

5.2 Thermal Cycling of Irradiated Thin Films

To assess the potential structural annealing effect in VO_2 thin films, we analyze the film quality before and after irradiation to introduce defects, and after anneal treatments that would repair the defective material through defect motion and recombination. Hall effect measurements on thin films provide a reliable gauge of defect concentrations by revealing carrier concentrations and mobility. The phase transition thermal hysteresis also provides a measure of crystal quality, but this characterization is only suitable for free-standing single-crystal VO_2 structures where the transition is not influenced by lattice strain. The phase transition is nucleated at defects and in these polycrystalline thin films, many grain boundaries exist. Furthermore, strain from the larger sapphire substrate and adjacent grains broaden the phase transition thermal hysteresis, reducing the influence of point defects in the bulk towards nucleating and progressing the transition. While this transition hysteresis ΔT of nanowires is around 10K and reduces with irradiation and increases in point defect concentration, the hysteresis for films is typically around 8K, and insensitive to it. Therefore, we rule out thermal hysteresis as a measure of film quality in the bulk, but still have two good measurements of quality via the Hall effect and RBS channeling.

5.2.1 Alpha-particle Irradiation

We first explore the structural annealing effect in VO_2 by measuring the Hall effect and electron mobility in thin films. To introduce additional point defects into the films, these films were irradiated by alpha particles (He^{2+} ions). At MeV energies, the alpha particles undergo some nuclear collisions with the VO_2 lattice, creating defects, but the majority experience only electronic stopping and fully penetrate the film (100 – 200 nm) and be embedded in the sapphire substrate [146,147]. The final positions for implanted ions generally follows a Gaussian distribution given by Equation 5.1:

$$n(x) = n(R_p)\exp\left(-\frac{(x-R_p)^2}{2\Delta R_p^2}\right) \tag{5.1}$$

where x is the position starting from the surface, R_p is the projected range, or average final position of the ions, and ΔR_p is the straggle or standard deviation of the projected range. For a 300nm VO_2 film on sapphire, the projected range of 3MeV He^{2+} ions is predicted to be 6.5um, as shown in Figure 5-2, well past the film and into the Al_2O_3

substrate. The simulation shows that only a negligible fraction of He ions remain embedded in the VO_2 film. Due to the extremely small number, and expected small size and non-bonding nature, we can ignore the presence of He in the lattice in considering the resulting defective VO_2 and its electronic and phase transition properties. We also assume the resulting point defects in VO_2 are non-interacting and do not accumulate into clusters. A recent study by Ramirez [148] on VO_2 irradiated by O^+ ions demonstrated no new phases or defect clusters form, with nearly identical x-ray diffraction reciprocal space maps before and after irradiation.

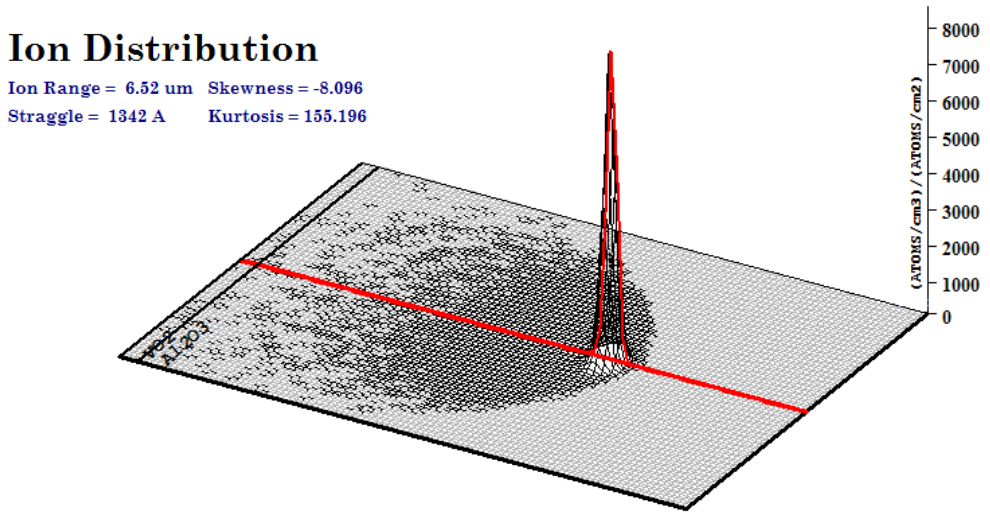

Figure 5-2. End of Range for 3 MeV He^{2+} Ions calculated by SRIM simulation. The VO_2 thickness is 300nm on a 10um Al_2O_3 substrate. The red line indicates the ion incidence direction and the concentration profile along it.

Figure 5-3 shows the results of a Monte Carlo simulation from Stopping Range of Ions in Matter (SRIM) for the damage produced by irradiation, with vacancies being produced at a roughly constant rate throughout the depth of the film. As a single He^{2+} ion with 3MeV initial energy travels through a film 250nm thick, it produces roughly 0.6 oxygen vacancies (the integrated area of the collision damage plot). The VO_2 films in this study were irradiated with a He^{2+} ion fluence (dose) of 2×10^{16} cm^{-2}, which should produce a maximum oxygen vacancy concentration of 4.8×10^{20} cm^{-3}, assuming there is no heating and refilling of vacancies during irradiation. The concentration of oxygen interstitials should also be in this range, but in practice, both numbers will be smaller due to some thermal relaxation and additional perturbation from He ions not simulated

in SRIM. Meanwhile, the vanadium vacancy concentration is only expected to be 8×10^{19} cm^{-3} from the same 2×10^{16} cm^{-2} ion dose.

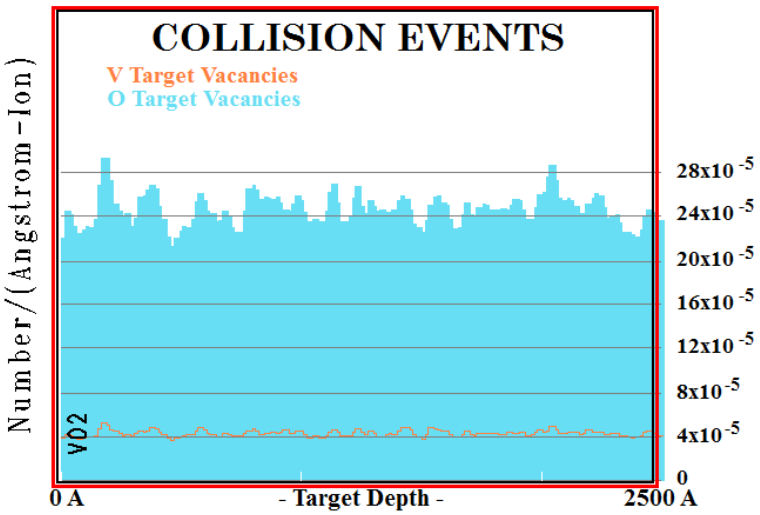

Figure 5-3. SRIM simulation of vacancy profile in VO_2 under 3 MeV He^{2+} ions (after 10^6 particle histories). The O vacancy concentration can be found by multiplying the simulated vacancy production factor with the fluence of He^{2+} ions: $(24 \times 10^{-5}/\text{Å} \cdot ion)(2 \times 10^{16}\ ions/cm^2) = 4.8 \times 10^{20}\ cm^{-3}$

The concentration of vanadium vacancies is only 1/6 of the oxygen vacancy concentration, owing to the larger mass of V (51 amu) compared to O (16amu), and the fact that there are only half as many vanadium atoms in the lattice. Another crucial input into the SRIM calculation is the displacement energy required to dislodge an atom from the lattice and form a vacancy. These displacement energy values of 65 eV for O and 135 eV for V, were taken from molecular dynamics studies on rutile, TiO_2, a compound with an identical crystal structure and nearly the same atomic masses [149,150]. After creating point defects in the semiconductor film by ion irradiation, we can quantify them via Hall effect and RBS channeling measurements. While both vacancies and interstitials for cations (V) and anions (O) are created by irradiation, oxygen point defects are far more prevalent due to their lighter mass, and persist after irradiation due to their energetic favorability [151–154]. We can characterize the amount of defects after irradiation via Hall effect to get the number of charge carriers. The large increase in conductivity and electron concentration is assumed to derive primarily from an increase in double-donor oxygen vacancies; a small fraction of singly-charged donor vanadium interstitials, acceptor vanadium vacancies, and acceptor oxygen interstitials exist but in reduced number, with relaxation even at room temperature [152,155,156].

A number of methods exist for characterizing point defects. In thin films, electron paramagnetic resonance (EPR) [152], deep-level transient spectroscopy (DLTS) [157,158], photo-induced conductivity transient spectroscopy (PICTS) [159], and Fourier transform infrared spectroscopy (FTIR) [160] are often used to identify defects, but quantifying them is very difficult. Particle beam methods like Rutherford backscattering (RBS) or secondary ion mass spectroscopy (SIMS) [161] can identify defect atoms like unknown dopants, but they cannot detect native defects, such as vacancies or interstitials based on a compound's constituent atoms. To detect vacancies, another beam-based method, positron annihilation spectroscopy (PAS) can be used [152]. This method is a time-resolved study of gamma rays in materials, which correspond to positron population decay by annihilation. Instead of these, we select RBS channeling and Hall effect as a rough quantification of the defects in the material, due to the high availability of this equipment at LBL.

5.2.2 Cyclic Heating Circuit

To enable heating across the phase transition temperature across a high number of cycles, I designed a custom heater circuit, shown in Figure 5-4. First, a power MOS (IRF510) provided a controllable high-current switch for the heater ON/OFF states. This was gated with a square wave from a function generator (generally 7.5 second period, with 2.5 seconds of signal HI for heating and 5 seconds signal LO for cooling). The local temperature of the chip during the cyclical heating was verified by a thermocouple, as well as by in situ electrical measurements tracking the resistance of a VO_2 film. This can be compared with the known resistance vs. temperature characteristic of the film to estimate the temperature. The resulting temperature response was a ΔT of 30K, with the temperature oscillating between T_{low} of 50 °C and T_{high} of 80 °C. This corresponded to the 10 to 90% levels of conductivity for the thin film, which was used rather than the full range in phase transition across the thin film, in order to reduce the total time spent heating and cooling.

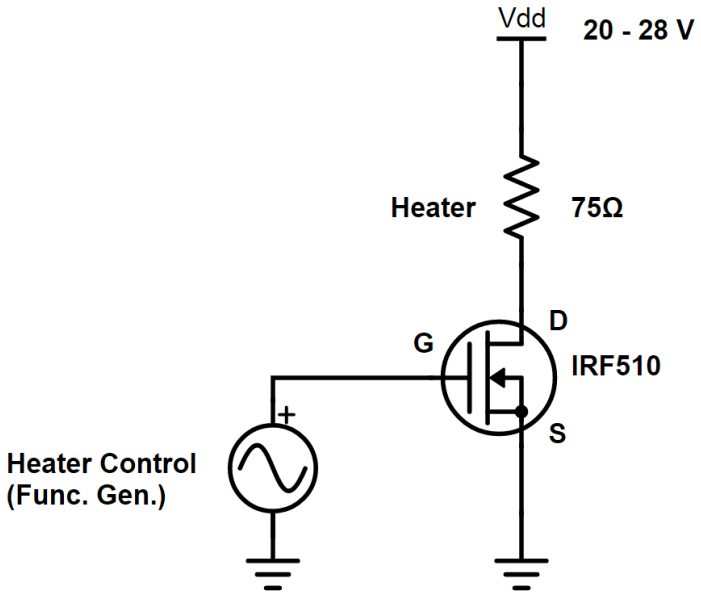

Figure 5-4. Schematic of Heating Circuit for Cycling Temperature. The heater is a Kapton-encapsulated film resistor and the control signal is a square wave of ~0.2Hz (or 5 sec period). Drawn with Digikey's online tool at http://www.digikey.com/schemeit/

In addition, the heater was fixed on an aluminum block which circulated cooling water to accelerate the cooling process. This heatsink was necessary as the natural convective cooling of the film had a long time constant, subjecting the thin films to an unnecessarily long thermal budget. By providing a cooled heatsink for thermal conduction, the temperature range was much more controllable and switching towards these endpoints proceeded more quickly. Without this pathway, the thin film and heater sit in air or on a mass, accumulating heat and eventually heating the surrounding air; the result is temperatures spiraling upwards unless we wait unreasonably long for the cooling phase. A photo of the setup is shown in Figure 5-5. As shown in the top right of the figure, the heating element is a flat serpentine metal resistor, encapsulated in Kapton (Omega KHLV series).

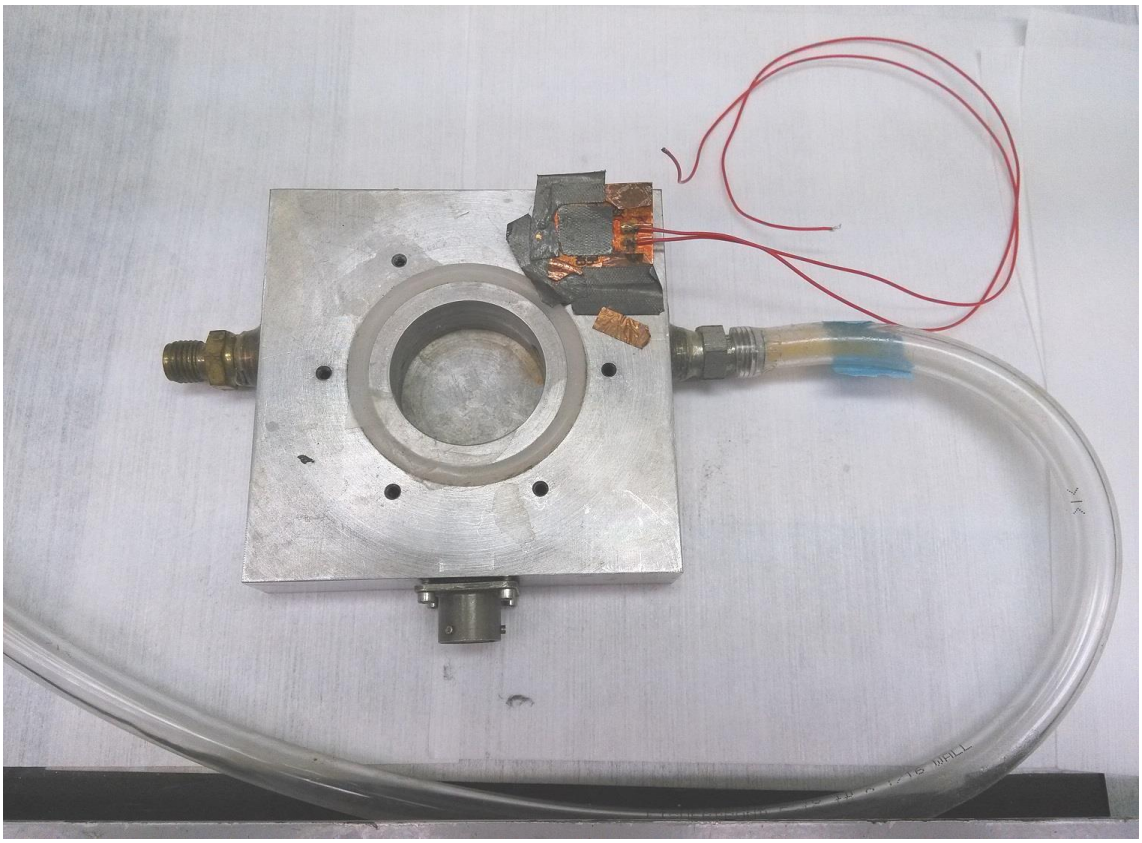

Figure 5-5. Photo of Cyclic Heating & Cooling Setup. Water flows through the aluminum block from right to left. The film heater (top right, in orange) is mounted with thermal tape to the aluminum block.

5.2.3 RBS Channeling Yield

We first track the quality of the VO_2 films by a precisely oriented RBS measurement, characterizing the minimum channeling yield, χ_{min}. The films grown by the PLD system are extremely high quality, with a χ_{min} of 5%, matching those previously reported for PLD-grown VO_2 films on sapphire [162] and approaching the minimum channeling yields of 3-4% for single-crystal silicon and GaAs [163]. This corroborates other evidence of high quality from measurements of our VO_2 films, including XRD rocking curves [92] and high resistance switching ratios, R_I/R_M, between the insulating and metal phases.

To assess the efficacy of the hypothesized 'MIT anneal', we examine the channeling yields of the VO_2 films before and after irradiation, and finally after anneal treatments. We irradiate the films with 3 MeV He^{2+} ions to create disorder, including

vacancies and interstitials in the lattice. This disorder causes a significant increase in channeling yield, χ_{min}, as the decrease in crystallinity allows more atoms to be visible to probing ions in the channeling RBS geometry. Figure 5-6 shows that after ion irradiation, the films' χ_{min} yields increase about 1-2% in absolute terms, which is large considering the χ_{min} for the pristine samples are only 5-8%. We note that there is an error bar of 0.5-1%, which is significant compared to the signal, but still smaller than the changes imparted by irradiation and the subsequent anneals.

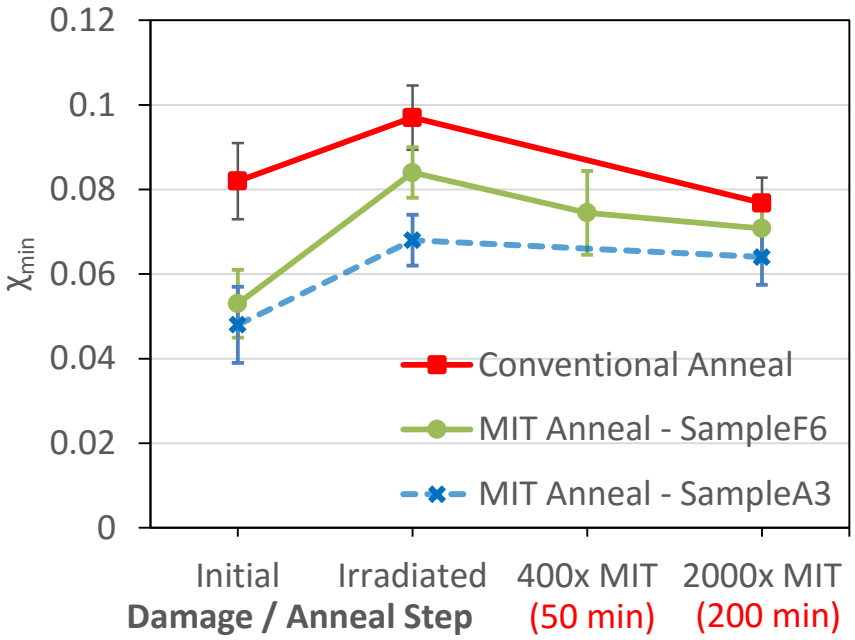

Figure 5-6. RBS Channeling Yield of VO_2 films in Pristine (initial), Irradiated (2×10^{16} cm^{-2} dose He^{2+}), and 2 stages of annealing. The conventional anneal (red) holds the samples at 85 °C, with the red numbers indicating cumulative anneal time. The bottom 2 data sets underwent cyclic (MIT) annealing, with the sample T cycled from 65 – 80 °C.

Each sample received one of two types of anneal treatments: 1) Conventional anneal – film held at 85 °C for the entire duration or 2) MIT (cyclic) anneal – film cycled from 65-80 °C, for at a time period of 7.5 seconds. The durations for conventional anneals (50 and 200 minutes) were chosen to correspond exactly to the amount of time the MIT annealed films were cycled for (400x or 2000x) times 7.5 seconds. The indicated anneal times or cycles are cumulative; *to serve as an upper bound for the thermal effect, the conventional anneal is slightly hotter and spans the entire duration of an equivalent MIT anneal, even though much of the time during the MIT anneal is spent with the heater off, in a cooling state towards 65 °C*. In this manner, we can more *definitively observe if*

the MIT anneal can do more to restore crystal quality, compared to a conventional single-step anneal with similar or slightly larger thermal budget. Lastly, the temperature range for the MIT anneal was chosen by looking at the resistance vs. temperature curve of the films, and sweeping between a range where the film undergoes 90% of the full range of transition (I/M resistance ratio). This represents a compromise between undergoing a full MIT in the film, while trying to keep the switching time low to reduce the total time spent heating and cooling.

Although we see a crystallinity increase (χ_{min} decrease) of 1.4% after 2000 MIT anneal cycles, we also observe a similar decrease of 2% with the conventional anneal. Thus, any improvement in crystal quality, as measured by RBS channeling, occurs on the same timescale, between the two anneal types. In other words, the repeated passage through the MIT with a cyclical anneal appears to result in the same rate of defect motion or passivation as achieved with a single thermal treatment. Furthermore, a second test of the MIT anneal with a higher quality film shows little improvement in the crystal quality (0.4%), well within the error in the measurement. We note that we select the lowest quality film (with χ_{min} of 8%) for conventional annealing, to assess the upper end of anneal behavior. A high defect concentration in a low-crystallinity setting gives us a large base of defects to annihilate, while the worse crystal quality should impede their motion. To conclude, the conventional anneal slightly outperforms the MIT anneal in recovering crystal quality, meaning the cyclic MIT anneal does not contribute any enhanced defect recovery in VO_2 thin films that is measurable by RBS channeling. We next turn to electronic conduction measurements to provide a different signal of crystal quality.

5.2.4 Hall Effect on Irradiated Thin Films

Electron mobility can reflect the crystal quality and the amount of disorder and scattering, while electron concentration can describe the amount of electrically active defects. Through Hall effect and electrical conductivity measurements, we can determine carrier type, concentration, and mobility of the thin films. As mentioned in the chapter on W-doped VO_2 films, extreme care must be taken with Hall effect measurements due to VO_2's low mobility ~0.1 cm^2/Vs, near the detection limit of conventional Hall effect measurements with a DC current. Figure 5-7 shows the electron concentrations of the samples before and after irradiation and anneal treatments. The initial electron concentrations for the highest quality films range from 1-1.7 × 10^{19} cm^{-3} while lower quality film F6 had 4.2 × 10^{19} electrons cm^{-3}. A brief study of varying irradiation doses shows a linear increase of electron concentration, *n*, for doses up to 3

× 10^{16} cm^{-2}. It is interesting to note that the more defective film is initially (with greater *n*), the more defects are produced by irradiation with 2 × 10^{16} He^{2+}/cm^2. This may be explained conceptually increased scattering interaction and "visibility" of nuclei in a defective crystal, as opposed to a more pristine sample, where some unintentional channeling might occur. After irradiation, the average film experiences an increase in electron concentration of 3 × 10^{19} cm^{-3}; dividing by the dose of 2 × 10^{16} He^{2+}/cm^2 and film thickness, this corresponds to 0.04 defects per incident ion, about an order of magnitude lower than predicted by SRIM.

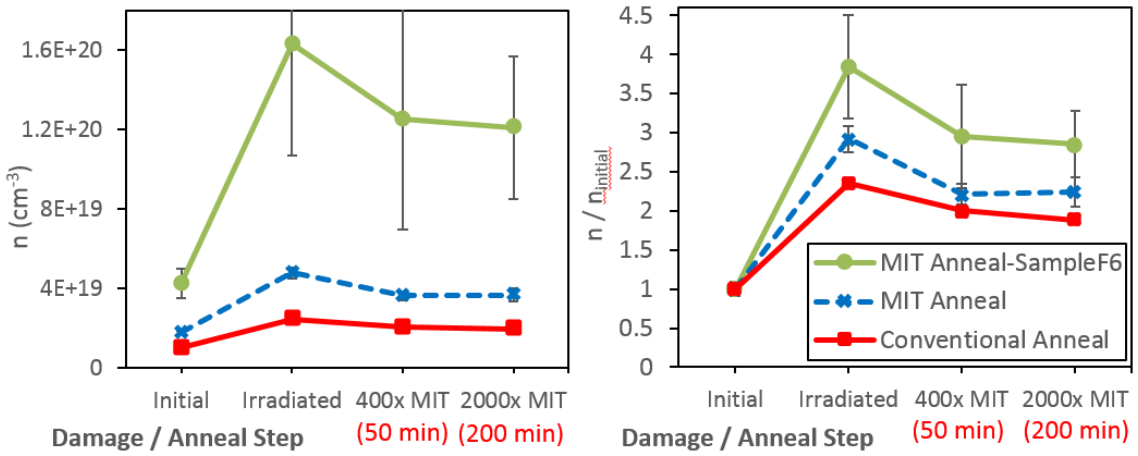

Figure 5-7. Electron concentration of VO_2 films before and after irradiation and anneal steps. Irradiated is after 2 × 10^{16} cm^{-2} dose of He^{2+}. Left: electron concentration, right: normalized electron concentration to sample initial concentration. All films and steps correspond to the same samples measured by RBS Channeling shown in Figure 5-6.

The long irradiation step increases the electron concentration 140-300% as shown in the normalized plot on the right side of Fig. 5-7. We next assess the effects of a cyclic MIT anneal and a conventional thermal anneal across different films by comparing the relative change in electron concentrations. Particle irradiation can lead to increases or decreases in carrier concentration, based on the compensating defect theory observed in several semiconductors [164–168]. The position of the Fermi stabilization level, E_{FS}, with respect to the semiconductor's band edges determines the net electronic effect of irradiation-induced point defects. In silicon, this stabilization level seems to be mid-gap, with irradiation resulting in carrier decrease in both p- and n-type silicon devices [169,170]. A "universal Fermi stabilization energy" is found to be 4.9 eV below vacuum, and for many compound semiconductors, exists near or above the conduction band edge [167,168,171–173]. This causes the amphoteric defects to be net n-type or electron doping in nature, and is the observed behavior when irradiating VO_2.

After 2000 cycles across the phase transition, *n* is reduced by 23-26%; for a conventional anneal combining the heating times into a single step, n Is reduced by 20%. Thus, the two anneals provide a very similar effect, and is within the error of the Hall effect measurements. A closer look at the sampling point after 400 cycles (equivalently 50 minutes conventional anneal) shows most of the change in *n* already occurs by this point. While the MIT anneal seems to produce a bigger change in *n* (24% decrease) at this point compared to a conventional anneal (16% decrease), the contrast is still not significant and does not indicate a great enhancement in anneal effectiveness.

The Hall effect measurements also provide the electron mobility, shedding further light on the lattice quality, but again show evidence that there is no significant effect for a cyclic anneal. Figure 5-8 shows that similar changes in mobility and resistivity can be achieved in irradiated VO_2 films using both the MIT cyclic anneal and the conventional one. The error bars for resistivity are very low, since this is only a 4-point thin film measurement, and does not involve applying a magnetic field to measure the resultant Hall voltage. The irradiation step lowers the resistivity 60-77% as shown in Fig. 5-8b, primarily due to the large change in electron concentration, since the mobility only changes around 10-50%. The resistivity increases slightly towards the pristine values, but both the cyclic MIT and conventional anneal steps cause a ~10% increase.

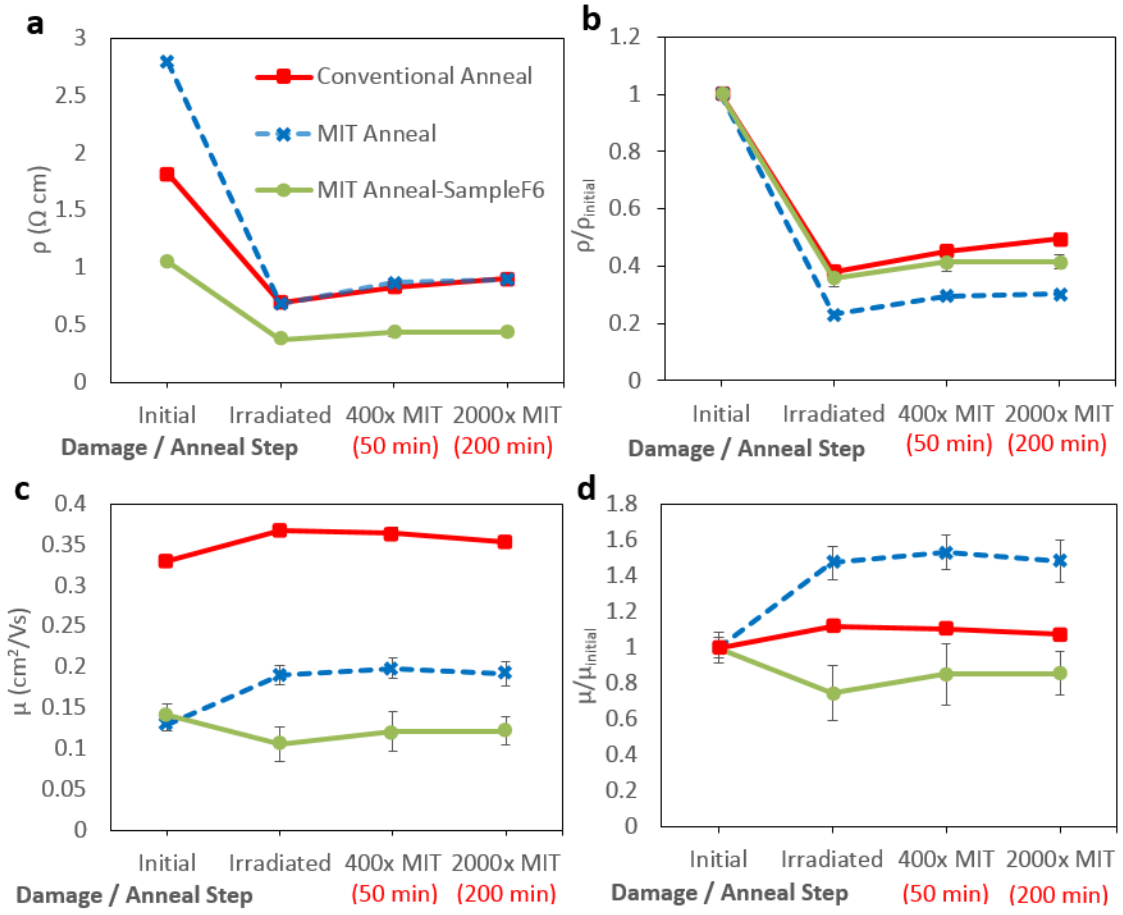

Figure 5-8. Resistivity and mobility of VO_2 films after irradiation (2×10^{16} cm^{-2}) and anneal treatments. a,c)resistivity, mobility, b,d) normalized resistivity, mobility (to Initial, pristine value for each sample)

The electron mobility of VO_2 thin films show unexpected behavior after irradiation, with different films experience increases or decrease in mobility. Electron mobility is expected to decrease with increased lattice disorder, with point defects breaking the periodicity and providing local recombination as well as elastic scattering centers [174,175]. However, decreasing mobility was only observed in one film, while the other two films showed a mobility increase after irradiation. The highest quality film (studied with conventional annealing) had a pristine mobility of 0.33 cm^2/Vs, irradiation increased it to nearly 0.37 cm^2/Vs. Meanwhile, a second film had a low pristine mobility around 0.13 cm^2/Vs, increasing to 0.19 cm^2/Vs after irradiation. This mobility increase contrasts with previous reports on irradiated materials, where introduction of defects

resulted in lowered mobility [171,176,177]. This is generally the case as doping and carrier concentration increases, due to increased Coulombic scattering. Regardless of the contribution to the carrier concentration, the local strain around point defects introduces increased scattering around the deformation potential [168,178].

A possible explanation for the mobility increase may be that the large increase in electron concentration spills electrons into a higher conduction band valley which shows increased mobility, owing to decreased effective mass and/or reduced intervalley scattering. While mobility increase versus irradiation has been observed in InN films, that mechanism involves a shift of conduction from the n-surface layer to the bulk layer (as the carrier concentration increases) [179], which may not be applicable in VO_2. However, this effect should not be ruled out, for films with small grain size and high interfacial defect concentrations. AFM and grain size characterization was not performed for all films, since an initial test showed grain sizes >200 nm, much larger than the electron mean free path, only 0.7 nm. Related to this discussion of grain boundaries and surface versus bulk conduction, another potential mechanism for the mobility increase is heating during irradiation. Despite keeping the He2+ beam current to a moderately low value, the irradiation occurs in vacuum which increases the thermal decay time, and bursts of ions may be localized in space or time, to cause heating and thermal annealing. The net effect may still be an increase in point defect and carrier concentration, while causing grain growth or passivation of traps along grains, contributing to increased mobility.

Comparing the changes in mobility, carrier concentration and conductivity imparted by the two types of low-temperature anneal, it is impossible to distinguish the effects of a cyclic or single-stage anneal. This is also the case when comparing the structural crystal quality measurements by RBS channeling. Unfortunately, there is no enhanced cyclic, phase transition-based anneal that can be observed in VO_2 films.

5.3 Conclusion

We assessed the quality of ion-irradiated VO_2 thin films to compare a cyclic, phase transition-based anneal and a conventional, single-step anneal. The two different anneals occurred at temperatures lower than conventional annealing, and resulted in a similar relative changes in electrical and structural characteristics. To controllably introduce point defects into the films, alpha-particle irradiation by an ion accelerator was used. Hall effect measurements provided a picture of crystal quality through

electron concentration and mobility, while RBS channeling qualitatively described the amount of interstitials. In both experiments, the films did not show a difference in recovery behavior whether annealed cyclically 2000 times across the MIT or heated in a single stage.

While several mechanisms were proposed for the possibility of increased point defect motion through the structural phase transition, our tests do not support this hypothesis. Any enhancement in defect motion and annihilation with a cyclic anneal would still require a greater energy input than the conventional anneal holding above the MIT temperature. This is a manifestation of the first law of thermodynamics, but the current results suggest that the additional input energy for a cyclic anneal is not available or insufficient in quantity to promote significant point defect migration.

Chapter 6

Summary

In this dissertation, we explored several applications and investigated the doping and annealing behavior utilizing the phase transition of VO_2. The simultaneous metal-insulator transition (MIT) and structural phase transition at 67 °C enable a variety of electrical, optical, and mechanical applications for vanadium dioxide. We synthesize high quality single-crystalline nanobeams by PVD and grow epitaxial VO_2 thin films by PLD to build bimorph actuators which operate with extremely high displacement and force. In both nanobeams and thin films, we explore tungsten doping as a means of lowering the transition temperature and engineering the device operation range. Spatially engineering the doping level in nanobeams enables a more controllable, broadband thermal actuator and sensor, as well as an improved bolometry material. To study a cyclic anneal based on the MIT, we characterize thin films by RBS channeling and Hall effect, and nanobeams by their MIT temperature hysteresis measured optically. The evidence suggests there is not enhanced annealing behavior from a cyclic, MIT anneal compared to a conventional single-stage anneal at the same temperature.

In our study on VO_2/Cr nanobeam bimorph actuators, we reveal the existence of an intermediate M2 phase that doubles the actuation amplitude, we find the operating cutoff frequency to be at least 4.5 kHz in the nanobeam width regime of hundreds nm to 1 μm, and we test their operation in water and in a millimeter-scale ensemble configuration embedded in polymer. The actuation speed agrees well with basic modeling of thermal conduction and convection, with the convection pathway dominating in nanostructures (owing to high surface area) and providing high operating speeds. VO_2 can be described as a solid engine for performing work, where the monoclinic-to-rutile structural phase transition is likened to the water-steam transformation for a steam engine. For a bimorph actuator performing work in the bending mode, we calculate the energy efficiency to be 3.6% ideally, which equates to a thermoelectric material with figure of merit ZT = 2, operating at this temperature difference of $T_{MIT} - T_0 = 40$ K. Nanobeam bimorph actuators enable a variety of applications including mobility as a leg or swimmer, sensing of wind and temperatures, as well as more complex operations like serving as a gate for cells.

To more controllably utilize these phase transition-based bimorph actuators, we demonstrated a VO_2 thin film fabrication process that can utilize conventional photolithography and dry etching to pattern devices into any desired shape. We demonstrate a palm-finger structure that could capture and release micro-particles. Most importantly, the Cr metal along the bimorph can be patterned into electrodes, which enable electrical actuation of the bimorphs via Joule heating. These bimorphs were found to have a cutoff operating frequency of 3.5 kHz, slower due to wider dimensions than nanobeams. From the bulk properties of VO_2, we find it to have extremely high work density (0.63J/cm^3), or amount of useful work it can perform via the structural transition per volume of material. Likewise, it stands out among other actuation materials by having a high stroke, or displacement-to-length ratio. Control of the actuator shape enables many more applications, including drug particle delivery microfluidic pumping, and artificial muscles. Phase-transition based thin film actuators may be promising in future applications in microrobotics and microfluidics. Specifically, one potential application that naturally progresses through cycles in temperature is polymerase chain reaction (PCR) in microfluidics, to would amplify or copy DNA [180]. The pumping and VO_2 actuation stages could be coupled to the PCR process, providing a quick, energy-efficient, and miniaturized functionality essential to many experiments in microbiology.

Next, we explore tungsten doping into VO_2 thin films and nanobeams to further increase device functionality. Several dopants can modify the MIT temperature, but tungsten is consistently found to be the most effective, by lowering the T_C by more than 20 K / % W. In our PLD-synthesized $W_xV_{1-x}O_2$ films with up to 7% tungsten, we confirm the T_C lowering effect and examine the effect of the doping on electronic properties. As expected, the W ionizes to W^{6+} and donates extra electrons to the VO_2 conduction band and Hall effect measurements show an increase in carrier concentration due to doping as well as partial MIT due to the lowered T_C. However, mobility is severely degraded in the doped films, which is expected due to ionized impurity scattering, but possibly also increased grain boundary scattering from worsened crystallinity. While RBS channeling measurements indicate the W is substitutional and Raman shows it to be single-phase, the study would benefit from additional AFM measurements to characterize the film crystallinity.

By axially varying the W composition along a VO_2 nanowire, we realize a device that responds to a range of temperatures, rather than in a narrow region around the undoped VO_2 MIT at 67 °C. This makes VO_2-based devices much more appealing, since a broader response curve allows greater sensitivity as a detector across a much wider

range of temperatures, or better control of actuation amplitude corresponding to a temperature setpoint. Specifically, the axially-doped WVO_2 nanobeams achieve an extremely high thermal coefficient of resistance (TCR) of 10-15 %/K which makes the material especially useful for bolometry. Both electrical measurements of the graded-doped nanobeams and operation as a WVO_2/Cr bimorph actuator showed a broad response to temperature across ΔT = 30 K, compared to a sharp response at the transition edges, separated by 2-5 K centered around T_C.

Finally, we explore a cyclic anneal, based on repeated transitions across the MIT, which was found to have the same effect as holding the material at an elevated temperature above the MIT for an equivalent time. Both treatments are low-temperature anneals at roughly 80 °C, much lower than conventional temperatures for defect recovery, but it was surmised that the structural phase transition could enhance point defect motion. High quality VO_2 thin films on sapphire were irradiated by alpha particles to introduce point defects, and the defect concentrations were roughly quantified by RBS channeling and Hall effect measurements. The irradiated films responded similarly to cyclic anneals of 2000 phase transitions and single-stage anneals at T greater than T_C. While we did not observe any enhanced annealing phenomena, our experiments confirm that the phase transition behavior of VO_2 is robust to large amounts of disorder (radiation > 2×10^{16} cm^{-2}, producing > 10^{19} defects cm^{-3}). This gives credit to potential uses of VO_2 for in high-radiation environments.

Appendix A

A.1 Rutherford Backscattering Spectrometry (RBS)

Rutherford Backscattering Spectrometry (RBS) is a well-established technique to determine composition and film thickness by examining the energy spectra of high energy (MeV) light ions that are backscattered by the sample. The energy carried by a backscattered ion (He^{2+}) can be found by modeling an elastic collision, using a kinematic factor, K_{m2}, relating the recoil energy, E_1, to the initial energy, E_0:

$$K_{m_2}(\theta, m_1, m_2) = \frac{E_1}{E_0} = \left[\frac{\sqrt{m_2^2 - m_1^2 \sin^2\theta} + m_1 \cos\theta}{m_1 + m_2}\right]^2$$

where m_1 is the mass of the incident ion and m_2 is the mass of the nucleus in the sample (stationary), and θ is the angle of scattering [181]. While the kinematic factor determines the energy of backscattered ions for a given geometry and target composition, quantitative results of the composition rely on measuring the counts of ions having various energies. The scattering is Coulombic in nature, and proportional to $(Z_1 Z_2 e^2)^2$, or to the square of the target atom's atomic number Z_2. Thus, the signal strength is much higher for heavier elements, and these are most easily identified with RBS even at small quantities.

As oxygen is very light, with atomic number of 8, RBS is not that accurate in determining the oxygen content of a binary oxide film, such as VO_X or TiO_X. Nonetheless, the technique shines in determining cation ratios in more complex compounds like $BaTiO_3$, $BiFeO_3$, or in our case, $W_xV_{1-x}O_2$. A backscattering spectrum can also be analyzed to provide depth profiling information, to determine changes in composition along the depth, or to explore heterostructure films.

A.2 Channeling RBS

Traditional Rutherford Backscattering spectroscopy relies on the backscattered signal from a randomly oriented film, with modeling of the resulting spectrum based on the likelihood of collision with a target element, specifically its areal number density. By precisely aligning a target's crystallographic directions along with the incoming ion directions, we can probe the crystal's structure and quality. This is related to the channeling effect seen in ion implantation, where high-energy ions travel much deeper into the crystal, along "channels" or open regions in the crystal structure, experiencing

much less nuclear scattering. Similarly, when high-energy ions enter a perfectly aligned crystal, the amount of backscattered ions is highly suppressed, and the remaining signal is often due to scattering by surface defects, or interstitials and other defects that are exposed or "visible" in the open channels [182,183].

By comparing the backscattering yield in a channeling geometry to a regular unaligned geometry, we get a measure of the disorder in the film. The minimum channeling yield, χ_{min}, is the ratio between the highly-aligned signal to the signal collected at a random orientation, with a low χ_{min} indicating high crystal quality. Figure A-1 illustrates a typical channeling spectrum and unaligned (regular RBS) spectrum for an epitaxial VO_2 film, showing how $\chi_{min} = Yield_{aligned}/Yield_{random}$ is calculated. For clarity of $Yield_{aligned}$, the film plotted in this figure is an earlier, lower quality film with χ_{min} of 10%. Our best VO_2 films grown by PLD show a χ_{min} of 5%, matching previous reports on films on sapphire [162]. In comparison, high quality, single-crystal silicon can have χ_{min} as low as 3%, and GaAs samples 4% [163].

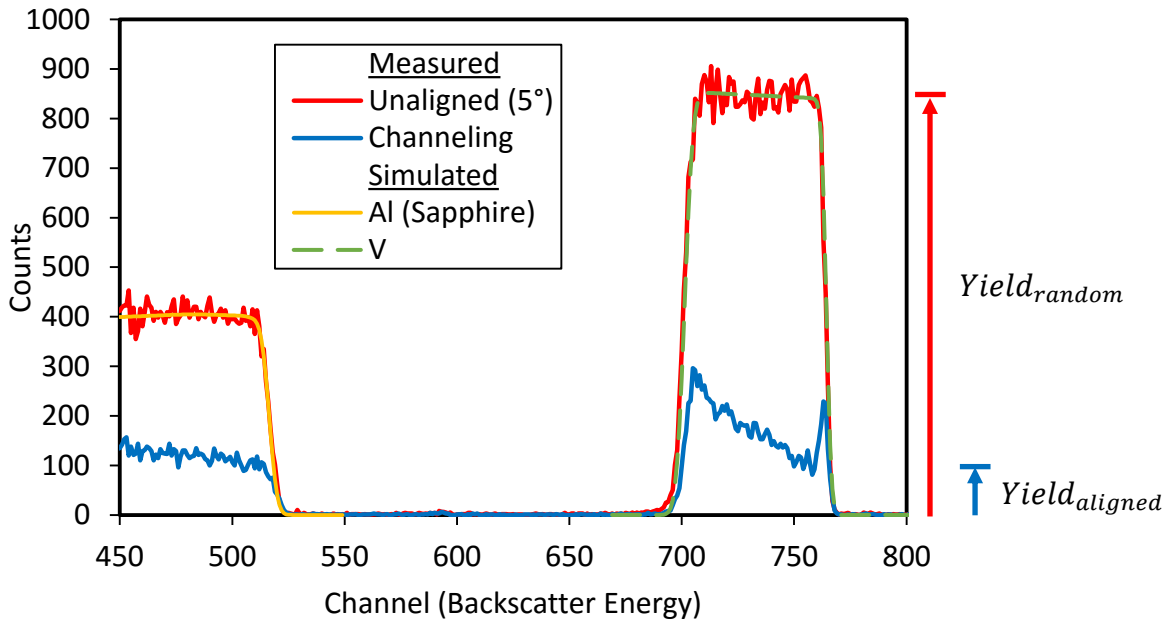

Figure A-1. Channeling RBS spectrum of VO_2 film on sapphire (Al_2O_3). Red: unaligned, at 5° tilt for random spectrum, Blue: channeling spectrum, aligned for minimum counts. Green/Yellow: Simulated spectrum for V/Al atoms at random alignment. The yield is taken as an integral of the signal for a small range in energy (channel), and χ_{min} is given by the ratio of aligned to random

yields. Signal from oxygen at lower energies is ignored; there is a large resonant scattering peak at the accelerating speed of 3.04 MeV.

The channeling RBS technique requires a sample to be single-crystalline within the beam spot, to allow for aligning to one crystal direction. While our epitaxial VO_2 films are not single-crystalline, their textured orientation on the sapphire into 3 rotationally variant domain directions still enables RBS channeling measurements. Specifically, these 3 rotational variants follow sapphire's trigonal structure in the film growth plane, and all share the [010] monoclinic VO_2 direction parallel to the sapphire [0001] direction or c-axis, perpendicular to the film and substrate surface [184,185].

As the RBS technique is destructive, extreme care must be taken in performing and interpreting the results of these channeling measurements. The same He^{2+} ions that are used to measure the film composition and quality by RBS are the exact same ones used during film irradiation to impart damage; the only difference is beam defocus during irradiation to damage the large film roughly across a 0.6mm x 0.6mm space. We collect measurements in several spots across the film, to determine the repeatability of our technique and understand the uniformity in quality across the film. The RBS measurements are taken from a 0.5mm diameter spot on the sample, with signal collected from 10 μC of charge: both are smaller than typical to limit the amount of film damage. At this dosage, each RBS measurement results in the equivalent of 4×10^{15} He^{2+}/cm^2 damage in the spot exposed to the beam. Thus, a film irradiated to 2×10^{16} He^{2+}/cm^2 receives 20% more damage when probed by RBS. We record the positions of all previously measured spots in order to only examine fresh regions of the film that have not yet been exposed to the focused RBS beam.

A.3 MIT Cycling of WVO_2 Nanowires

To repeatedly subject nanowires to the MIT, we can a) mechanically strain them at room temperature or b) heat them, to study the possible annealing effects and point defect motion. Both of these methods of cycling across the MIT can be contrasted with a single cycle of equivalent duration, to rule out any steady-state thermal effects. A schematic of this experiment is shown in Fig. A-2. We first study the thermal-based cycling by using a chopped laser to repeatedly heat and cool the graded and step-doped WVO_2 nanowires, while looking for changes in MIT behavior spatially across the nanobeam. Next, we study pristine and irradiated VO_2 nanobeams by cyclic mechanical strain and observing the MIT hysteresis as a gauge of point defect concentration. Though we thermally cycled the WVO_2 nanobeams to tens of millions (3E7) cycles, and

mechanically strained the VO_2 nanobeams thousands of cycles, we only observed slight changes, insufficient to demonstrate any mechanical annealing effect.

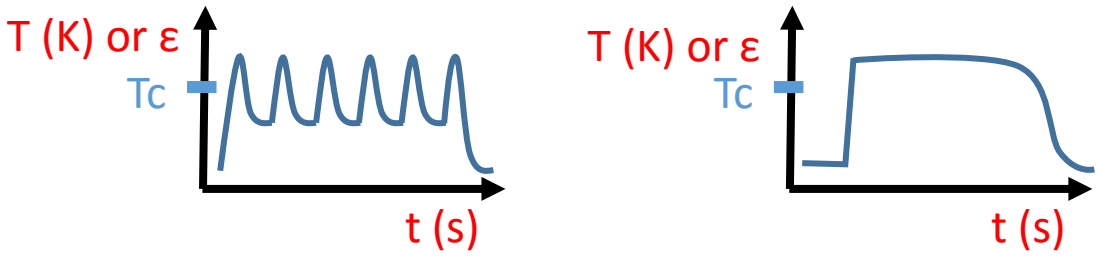

Figure A-2. MIT cycling of nanowires (or thin films) in experiment. Left: cyclic anneal applied via strain or temperature. Right: single-step strain or temperature, representing one cycle across the MIT for an equivalent time compared to the cyclic anneal.

From the bimorph actuator work, we know the nanowire's thermal response speed is in the 4 kHz range. Thus, we chop the laser at 1 kHz to stay well below this limit ensuring repeated passage across the phase transition. The Raman system's 488nm wavelength laser was used, with the power increased just enough to transition the majority of the nanowire to metal phase. We study the MIT behavior of graded- and step-doped wires to check if there is enhanced W diffusion along the rutile c-axis that can be activated by the MIT. With the help of Dr. Sangwook Lee, graded-doped WVO_2 wires were grown as before, from mixed WO_2 and VO_2 powder, for 10-min at 880 °C. WVO_2 wires with a step-profile in W concentration in the middle were grown by: a) 900 °C for 1 hr, from VO_2 powder only, b) magnetically inserting crucible with WO_2 powder into the heated zone of the furnace, and continuing growth for 3 more hours.

Fickian diffusion predicts that W should diffuse down a concentration gradient to regions with lower W composition. Figure A-3a shows that the MIT behavior of the graded-doped wire changes in this manner, with the end of the nanobeam adopting a lower MIT temperature by ~8K after 10 million cycles of the laser, presumably due to increased tungsten composition in that region. Meanwhile, the MIT behavior of the step-doped wire might be seen to broaden after 10 million cycles, but this is within the noise of the measurement ±1 °C, determined from repeated measurements.

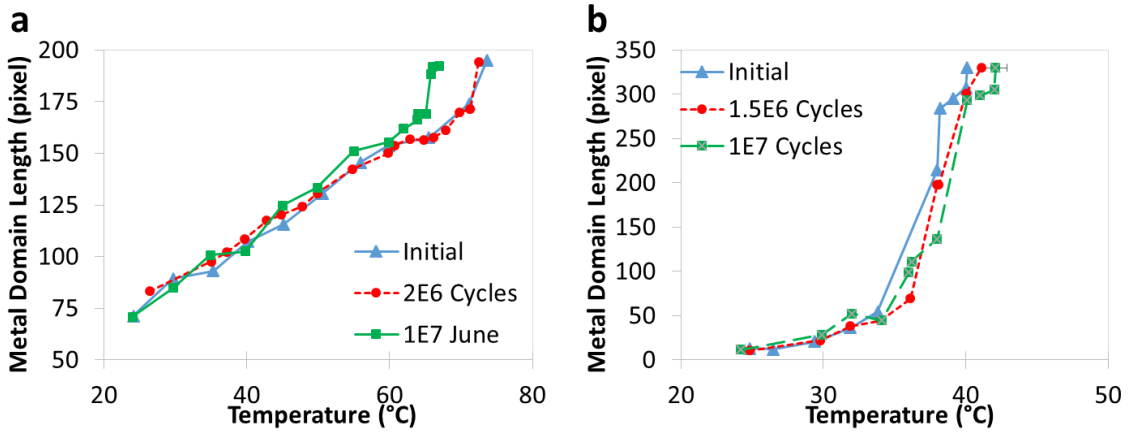

Figure A-3. Progression of the MIT progress vs. T in a) graded-doped and b) step-doped WVO_2 nanobeams. The y-axis, metal domain length can be converted into axial position along the nanobeam, while the x-axis can be divided by W doping power (dT/dx(W)) to yield W composition. Transposing such axes would result in a plot of W composition vs. nanowire position.

Despite encouraging results in the graded-doped wire, we see that a single-cycle thermal anneal leads to similar changes in the MIT temperature. Figure A-4 shows that annealing for 80 minutes leads to a 8K rise in the MIT temperature, which eventually falls back down after annealing for 260 minutes. It is possible that oxygen related passivation is at play here, as these final transition temperatures are in the range of undoped VO_2. The lower temperature regions governed by the WVO_2 doped areas are still transitioning at the same points; thus it is likely that there is little to no motion of the W atoms.

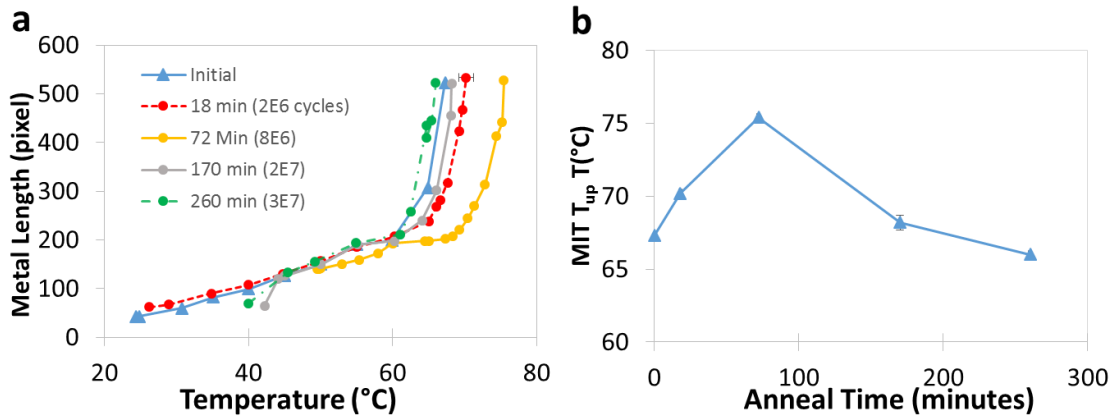

Figure A-4. Single-step laser anneal of graded-doped WVO_2 nanobeam. a) MIT progression, b) Temperature of full MIT progress (T_{up}) determined by the T where the metal domain length reaches the maximum, or entire nanobeam length.

A.4 MIT Cycling of Irradiated VO_2 Nanowires

Strain-induced MIT was performed by bending irradiated VO_2 nanobeams at room temperature to assess the effect on point defects, measured by the MIT hysteresis. As with the thin films, the MIT behavior was measured at 5K/min heating and cooling rate. The initial results were promising, with irradiated nanowires showing decreased hysteresis due to point defects, and mechanical cycling led to some recovery of the hysteresis towards larger, pristine values. Similar to the thin films, the VO_2 nanobeams were irradiated by 3MeV alpha particles (He^{2+}) in doses of 1-2 × 10^{16} cm^{-2}. To perform strain cycling, a piezoelectric stage (PI E-500) was driven by a sine wave voltage at 5-12 Hz up to 67,000 cycles. While we cannot see the nucleated metal domains during bending due to microscope and angle, the VO_2 is strained to curvatures that should produce a triangular metal/insulator domain structure according to previous work by Cao.

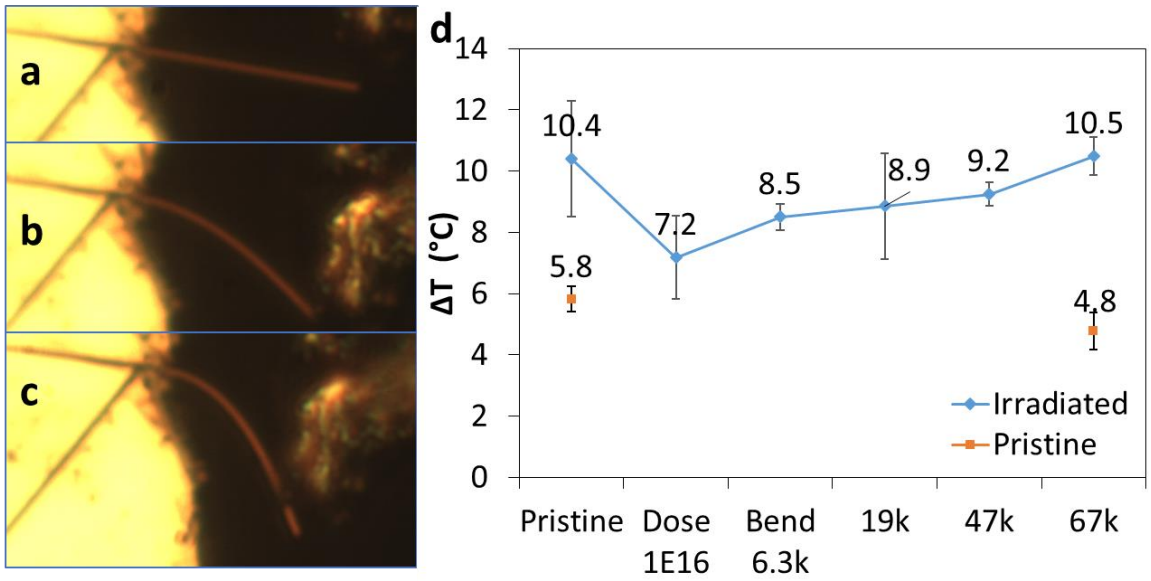

Figure A-5. Bending of VO_2 nanobeams (a-c), MIT hysteresis, ΔT (d) after 1E16 cm^{-2} He^{2+} irradiation and bending. Error bars are taken as standard deviation of 3-10 measurements after each irradiation or bending stage.

After bending the nanobeam 67,000 times, the MIT hysteresis ΔT increases from 7.2K to 10.5K, the pristine value. We compare this to holding the nanowire strained for an extended period, as well as adding some moderate heat (to 150 °C) in one duration, to rule out any ambient or aging effects. Figure A-6 shows that the hysteresis in this control strangely increases after irradiation, and subsequent low-temperature

annealing does not further increase hysteresis (decreasing point defects). Rather, the MIT hysteresis decreases slightly after 8 hours (the equivalent time needed for 67,000 bending transitions).

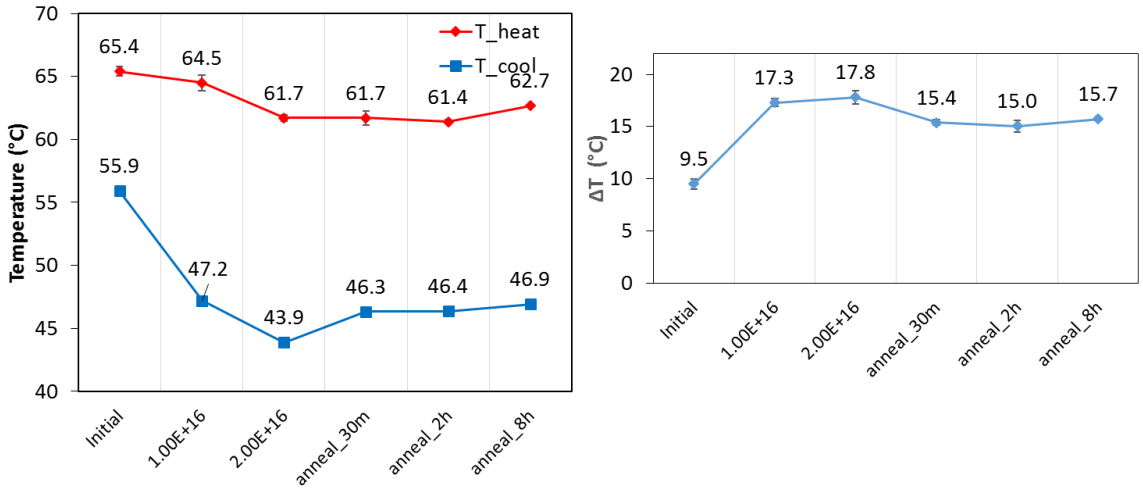

Figure A-6. Control for single-cycle bending. Anneals applied global heat of 150 °C for cumulative times listed. Left: T_{heat} and T_{cool} are the hysteresis endpoints Right: MIT hysteresis ΔT calculated by : T_{heat} - T_{cool}

Unfortunately, the recovery behavior of the wire in Fig. A-5 was not reproduced in other nanobeams. Some nanobeams did not show any increase in hysteresis after bending, and instead exhibit a decrease, suggesting an increase in defect concentration. Care must be taken in future studies to first reproduce the same nanowire quality after irradiation, as measured by a decrease in MIT hysteresis. Heating of the sample by the He^{2+} ion beam could contribute to some heating and unintentional recovery of point defects. However, this heating also occurs in vacuum, which could lead to some oxygen deficiencies, and result in lowered MIT temperature due to the electronic effect of vacancies. For this reason, it is also suggested that future studies of the MIT in nanobeams be undertaken in a controlled environment, with better isolation of wind and control of environmental gas such as oxygen. The current results suggest that any potential mechanical annealing effect, utilizing thermal and mechanical cycling across a phase transition, is weak or non-existent and not easily observed.

Bibliography

[1] Berglund, C. N. & Guggenheim, H. J. Electronic Properties of VO_2 near the Semiconductor-Metal Transition. *Physical Review* **185,** 1022–1033 (1969).

[2] Goodenough, J. B. The two components of the crystallographic transition in VO_2. *Journal of Solid State Chemistry* **3,** 490–500 (1971).

[3] Pellegrino, L., Manca, N., Kanki, T., Tanaka, H., Biasotti, M., Bellingeri, E., Siri, A. S. & Marré, D. Multistate Memory Devices Based on Free-standing VO_2/TiO_2 Microstructures Driven by Joule Self-Heating. *Advanced Materials* **24,** 2929–2934 (2012).

[4] Coy, H., Cabrera, R., Sepúlveda, N. & Fernández, F. E. Optoelectronic and all-optical multiple memory states in vanadium dioxide. *Journal of Applied Physics* **108,** 113115 (2010).

[5] Hormoz, S. & Ramanathan, S. Limits on vanadium oxide Mott metal–insulator transition field-effect transistors. *Solid-State Electronics* **54,** 654–659 (2010).

[6] Chain, E. E. Optical properties of vanadium dioxide and vanadium pentoxide thin films. *Applied Optics* **30,** 2782 (1991).

[7] Gao, Y., Wang, S., Kang, L., Chen, Z., Du, J., Liu, X., Luo, H. & Kanehira, M. VO_2–$Sb:SnO_2$ composite thermochromic smart glass foil. *Energy & Environmental Science* **5,** 8234–8237 (2012).

[8] Hu, B., Zhang, Y., Chen, W., Xu, C. & Wang, Z. L. Self-heating and External Strain Coupling Induced Phase Transition of VO_2 Nanobeam as Single Domain Switch. *Advanced Materials* **23,** 3536–3541 (2011).

[9] Strelcov, E., Lilach, Y. & Kolmakov, A. Gas Sensor Based on Metal−Insulator Transition in VO_2 Nanowire Thermistor. *Nano Letters* **9,** 2322–2326 (2009).

[10] Kim, B.-J., Lee, Y. W., Chae, B.-G., Yun, S. J., Oh, S.-Y., Kim, H.-T. & Lim, Y.-S. Temperature dependence of the first-order metal-insulator transition in VO_2 and programmable critical temperature sensor. *Applied Physics Letters* **90,** 23515 (2007).

[11] Cao, J., Ertekin, E., Srinivasan, V., Fan, W., Huang, S., Zheng, H., Yim, J. W. L., Khanal, D. R., Ogletree, D. F., Grossman, J. C. & Wu, J. Strain engineering and one-

dimensional organization of metal–insulator domains in single-crystal vanadium dioxide beams. *Nature Nanotechnology* **4,** 732–737 (2009).

[12] Brückner, W., Gerlach, U., Brückner, H.-P., Moldenhauer, W. & Oppermann, H. Influence of nonstoichiometry on the phase transitions in Ga-, Al-, and Fe-doped VO_2. *physica status solidi (a)* **42,** 295–303 (1977).

[13] Brückner, W. Structural relations between the VO_2 phases. *Kristall und Technik* **16,** K28–K31 (1981).

[14] Rúa, A., Fernández, F. E. & Sepúlveda, N. Bending in VO_2-coated microcantilevers suitable for thermally activated actuators. *Journal of Applied Physics* **107,** 74506 (2010).

[15] Liu, K., Cheng, C., Cheng, Z., Wang, K., Ramesh, R. & Wu, J. Giant-Amplitude, High-Work Density Microactuators with Phase Transition Activated Nanolayer Bimorphs. *Nano Letters* **12,** 6302–6308 (2012).

[16] Cao, J., Fan, W., Zhou, Q., Sheu, E., Liu, A., Barrett, C. & Wu, J. Colossal thermal-mechanical actuation via phase transition in single-crystal VO_2 microcantilevers. *Journal of Applied Physics* **108,** 83538 (2010).

[17] Toda, M., Ono, T., Liu, F. & Voiculescu, I. Evaluation of bimaterial cantilever beam for heat sensing at atmospheric pressure. *Review of Scientific Instruments* **81,** 55104 (2010).

[18] Cabrera, R., Merced, E., Sepúlveda, N. & Fernández, F. E. Dynamics of photothermally driven VO_2-coated microcantilevers. *Journal of Applied Physics* **110,** 94510 (2011).

[19] Tselev, A., Budai, J. D., Strelcov, E., Tischler, J. Z., Kolmakov, A. & Kalinin, S. V. Electromechanical Actuation and Current-Induced Metastable States in Suspended Single-Crystalline VO_2 Nanoplatelets. *Nano Letters* **11,** 3065–3073 (2011).

[20] Sengupta, S., Wang, K., Liu, K., Bhat, A. K., Dhara, S., Wu, J. & Deshmukh, M. M. Field-effect modulation of conductance in VO_2 nanobeam transistors with HfO2 as the gate dielectric. *Applied Physics Letters* **99,** 62114 (2011).

[21] Merced, E., Dávila, N., Torres, D., Cabrera, R., Fernández, F. E. & Sepúlveda, N. Photothermal actuation of VO_2 :Cr-coated microcantilevers in air and aqueous media. *Smart Materials and Structures* **21,** 105009 (2012).

[22] Cheng, C., Fan, W., Cao, J., Ryu, S.-G., Ji, J., Grigoropoulos, C. P. & Wu, J. Heat Transfer across the Interface between Nanoscale Solids and Gas. *ACS Nano* **5,** 10102–10107 (2011).

[23] Kucharczyk, D. & Niklewski, T. Accurate X-ray determination of the lattice parameters and the thermal expansion coefficients of VO_2 near the transition temperature. *Journal of Applied Crystallography* **12,** 370–373 (1979).

[24] Marezio, M., McWhan, D. B., Remeika, J. P. & Dernier, P. D. Structural Aspects of the Metal-Insulator Transitions in Cr-Doped VO_{2}. *Physical Review B* **5,** 2541–2551 (1972).

[25] Rúa, A., Cabrera, R., Coy, H., Merced, E., Sepúlveda, N. & Fernández, F. E. Phase transition behavior in microcantilevers coated with M1-phase VO_2 and M2-phase VO_2:Cr thin films. *Journal of Applied Physics* **111,** 104502 (2012).

[26] Zhang, S., Kim, I. S. & Lauhon, L. J. Stoichiometry Engineering of Monoclinic to Rutile Phase Transition in Suspended Single Crystalline Vanadium Dioxide Nanobeams. *Nano Letters* **11,** 1443–1447 (2011).

[27] Tselev, A., Strelcov, E., Luk'yanchuk, I. A., Budai, J. D., Tischler, J. Z., Ivanov, I. N., Jones, K., Proksch, R., Kalinin, S. V. & Kolmakov, A. Interplay between Ferroelastic and Metal−Insulator Phase Transitions in Strained Quasi-Two-Dimensional VO_2 Nanoplatelets. *Nano Letters* **10,** 2003–2011 (2010).

[28] Guo, H., Chen, K., Oh, Y., Wang, K., Dejoie, C., Syed Asif, S. A., Warren, O. L., Shan, Z. W., Wu, J. & Minor, A. M. Mechanics and Dynamics of the Strain-Induced M1–M2 Structural Phase Transition in Individual VO_2 Nanowires. *Nano Letters* **11,** 3207–3213 (2011).

[29] Okimura, K., Watanabe, T. & Sakai, J. Stress-induced VO_2 films with M2 monoclinic phase stable at room temperature grown by inductively coupled plasma-assisted reactive sputtering. *Journal of Applied Physics* **111,** 73514 (2012).

[30] Cao, J., Gu, Y., Fan, W., Chen, L. Q., Ogletree, D. F., Chen, K., Tamura, N., Kunz, M., Barrett, C., Seidel, J. & Wu, J. Extended Mapping and Exploration of the Vanadium Dioxide Stress-Temperature Phase Diagram. *Nano Letters* **10,** 2667–2673 (2010).

[31] Steeneken, P. G., Le Phan, K., Goossens, M. J., Koops, G. E. J., Brom, G. J. a. M., van der Avoort, C. & van Beek, J. T. M. Piezoresistive heat engine and refrigerator. *Nature Physics* **7,** 354–359 (2011).

[32] Liu, Y. The work production of shape memory alloy. *Smart Materials and Structures* **13,** 552 (2004).

[33] Lima, M. D., Li, N., Andrade, M. J. de, Fang, S., Oh, J., Spinks, G. M., Kozlov, M. E., Haines, C. S., Suh, D., Foroughi, J., Kim, S. J., Chen, Y., Ware, T., Shin, M. K., Machado, L. D., Fonseca, A. F., Madden, J. D. W., Voit, W. E., Galvão, D. S. &

Baughman, R. H. Electrically, Chemically, and Photonically Powered Torsional and Tensile Actuation of Hybrid Carbon Nanotube Yarn Muscles. *Science* **338,** 928–932 (2012).

[34] Shen, D., Park, J.-H., Ajitsaria, J., Choe, S.-Y., III, H. C. W. & Kim, D.-J. The design, fabrication and evaluation of a MEMS PZT cantilever with an integrated Si proof mass for vibration energy harvesting. *Journal of Micromechanics and Microengineering* **18,** 55017 (2008).

[35] Timoshenko, S. Analysis of Bi-Metal Thermostats. *Journal of the Optical Society of America* **11,** 233 (1925).

[36] Straumanis, M. E. & Weng, C. C. The precise lattice constant and the expansion coefficient of chromium between +10 and +60° C. *Acta Crystallographica* **8,** 367–371 (1955).

[37] McWhan, D. B., Marezio, M., Remeika, J. P. & Dernier, P. D. X-ray diffraction study of metallic VO_2. *Physical Review B* **10,** 490–495 (1974).

[38] Stokey, W.F. in *Shock and Vibration Handbook* (eds. Harris, C.M. & Crede, C.E.) 7.1-7.18 (McGraw-Hill, 1976).

[39] Wu, J., Gu, Q., Guiton, B. S., de Leon, N. P., Ouyang, L. & Park, H. Strain-Induced Self Organization of Metal−Insulator Domains in Single-Crystalline VO_2 Nanobeams. *Nano Letters* **6,** 2313–2317 (2006).

[40] Koumelis, C. N. The thermal expansion coefficient of chromium in the temperature region of 3 to 80 °C. *physica status solidi (a)* **19,** K65–K69 (1973).

[41] Incropera, F.P. & Dewitt, D.P. *Introduction to Heat Transfer*. (John Wiley & Sons, Inc., 2002).

[42] Atkin, J. M., Berweger, S., Chavez, E. K., Raschke, M. B., Cao, J., Fan, W. & Wu, J. Strain and temperature dependence of the insulating phases of VO_2 near the metal-insulator transition. *Physical Review B* **85,** 20101 (2012).

[43] Tselev, A., Luk'yanchuk, I. A., Ivanov, I. N., Budai, J. D., Tischler, J. Z., Strelcov, E., Kolmakov, A. & Kalinin, S. V. Symmetry Relationship and Strain-Induced Transitions between Insulating M1 and M2 and Metallic R phases of Vanadium Dioxide. *Nano Letters* **10,** 4409–4416 (2010).

[44] Gu, Q., Falk, A., Wu, J., Ouyang, L. & Park, H. Current-Driven Phase Oscillation and Domain-Wall Propagation in WxV1-xO2 Nanobeams. *Nano Letters* **7,** 363–366 (2007).

[45] Mirfakhrai, T., Madden, J. D. W. & Baughman, R. H. Polymer artificial muscles. *Materials Today* **10,** 30–38 (2007).

[46] Vaia, R. & Baur, J. Adaptive Composites. *Science* **319,** 420–421 (2008).

[47] Koerner, H., White, T. J., Tabiryan, N. V., Bunning, T. J. & Vaia, R. A. Photogenerating work from polymers. *Materials Today* **11,** 34–42 (2008).

[48] LeMieux, M. C., McConney, M. E., Lin, Y.-H., Singamaneni, S., Jiang, H., Bunning, T. J. & Tsukruk, V. V. Polymeric Nanolayers as Actuators for Ultrasensitive Thermal Bimorphs. *Nano Letters* **6,** 730–734 (2006).

[49] Zheng, L.-S. & Lu, M. S.-C. A large-displacement CMOS micromachined thermal actuator with comb electrodes for capacitive sensing. *Sensors and Actuators A: Physical* **136,** 697–703 (2007).

[50] Zhu, S.-E., Shabani, R., Rho, J., Kim, Y., Hong, B. H., Ahn, J.-H. & Cho, H. J. Graphene-Based Bimorph Microactuators. *Nano Letters* **11,** 977–981 (2011).

[51] Steel, M. R., Harrison, F. & Harper, P. G. The piezoelectric bimorph: An experimental and theoretical study of its quasistatic response. *Journal of Physics D: Applied Physics* **11,** 979 (1978).

[52] King, T. G., Preston, M. E., Murphy, B. J. M. & Cannell, D. S. Piezoelectric ceramic actuators: A review of machinery applications. *Precision Engineering* **12,** 131–136 (1990).

[53] Wu, C. C. M., Kahn, M. & Moy, W. Piezoelectric Ceramics with Functional Gradients: A New Application in Material Design. *Journal of the American Ceramic Society* **79,** 809–812 (1996).

[54] Wood, R. J., Steltz, E. & Fearing, R. S. Optimal energy density piezoelectric bending actuators. *Sensors and Actuators A: Physical* **119,** 476–488 (2005).

[55] Krulevitch, P., Lee, A. P., Ramsey, P. B., Trevino, J. C., Hamilton, J. & Northrup, M. A. Thin film shape memory alloy microactuators. *Journal of Microelectromechanical Systems* **5,** 270–282 (1996).

[56] Makino, E., Mineta, T., Mitsunaga, T., Kawashima, T. & Shibata, T. Sphincter actuator fabricated with PDMS/SMA bimorph cantilevers. *Microelectronic Engineering* **88,** 2662–2665 (2011).

[57] Baughman, R. H., Cui, C., Zakhidov, A. A., Iqbal, Z., Barisci, J. N., Spinks, G. M., Wallace, G. G., Mazzoldi, A., Rossi, D. D., Rinzler, A. G., Jaschinski, O., Roth, S. & Kertesz, M. Carbon Nanotube Actuators. *Science* **284,** 1340–1344 (1999).

[58] Landi, B. J., Raffaelle, R. P., Heben, M. J., Alleman, J. L., VanDerveer, W. & Gennett, T. Single Wall Carbon Nanotube−Nafion Composite Actuators. *Nano Letters* **2,** 1329–1332 (2002).

[59] Chen, L., Liu, C., Liu, K., Meng, C., Hu, C., Wang, J. & Fan, S. High-performance, low-voltage, and easy-operable bending actuator based on aligned carbon nanotube/polymer composites. *ACS Nano* **5,** 1588–1593 (2011).

[60] Li, J., Ma, W., Song, L., Niu, Z., Cai, L., Zeng, Q., Zhang, X., Dong, H., Zhao, D., Zhou, W. & Xie, S. Superfast-Response and Ultrahigh-Power-Density Electromechanical Actuators Based on Hierarchal Carbon Nanotube Electrodes and Chitosan. *Nano Letters* **11,** 4636–4641 (2011).

[61] Zhang, X., Pint, C. L., Lee, M. H., Schubert, B. E., Jamshidi, A., Takei, K., Ko, H., Gillies, A., Bardhan, R., Urban, J. J., Wu, M., Fearing, R. & Javey, A. Optically- and Thermally-Responsive Programmable Materials Based on Carbon Nanotube-Hydrogel Polymer Composites. *Nano Letters* **11,** 3239–3244 (2011).

[62] Huber, J. E., Fleck, N. A. & Ashby, M. F. The selection of mechanical actuators based on performance indices. *Proceedings of the Royal Society of London A: Mathematical, Physical and Engineering Sciences* **453,** 2185–2205 (1997).

[63] Zhang, Q. M., Bharti, V. & Zhao, X. Giant Electrostriction and Relaxor Ferroelectric Behavior in Electron-Irradiated Poly(vinylidene fluoride-trifluoroethylene) Copolymer. *Science* **280,** 2101–2104 (1998).

[64] Wei, J., Wang, Z., Chen, W. & Cobden, D. H. New aspects of the metal–insulator transition in single-domain vanadium dioxide nanobeams. *Nature Nanotechnology* **4,** 420–424 (2009).

[65] Wall, S., Wegkamp, D., Foglia, L., Appavoo, K., Nag, J., Jr, R. F. H., Stähler, J. & Wolf, M. Ultrafast changes in lattice symmetry probed by coherent phonons. *Nature Communications* **3,** 721 (2012).

[66] Rivera, F., Burk, L., Davis, R. & Vanfleet, R. Electron back-scattered diffraction of crystallized vanadium dioxide thin films on amorphous silicon dioxide. *Thin Solid Films* **520,** 2461–2466 (2012).

[67] Sershen, S. R., Mensing, G. A., Ng, M., Halas, N. J., Beebe, D. J. & West, J. L. Independent Optical Control of Microfluidic Valves Formed from Optomechanically Responsive Nanocomposite Hydrogels. *Advanced Materials* **17,** 1366–1368 (2005).

[68] Garcia-Cordero, J. L., Kurzbuch, D., Benito-Lopez, F., Diamond, D., Lee, L. P. & Ricco, A. J. Optically addressable single-use microfluidic valves by laser printer lithography. *Lab on a Chip* **10,** 2680–2687 (2010).

[69] Liu, K., Cheng, C., Suh, J., Tang-Kong, R., Fu, D., Lee, S., Zhou, J., Chua, L. O. & Wu, J. Powerful, Multifunctional Torsional Micromuscles Activated by Phase Transition. *Advanced Materials* **26,** 1746–1750 (2014).

[70] Eyert, V. The metal-insulator transitions of VO_2: A band theoretical approach. *Annalen der Physik* **11,** 650–704 (2002).

[71] Hörlin, T., Niklewski, T. & Nygren, M. Magnetic, electrical and thermal studies on the V1−xMox02. *Materials Research Bulletin* **8,** 179–189 (1973).

[72] Shibuya, K., Kawasaki, M. & Tokura, Y. Metal-insulator transition in epitaxial V1−xWxO2(0 ≤ x ≤ 0.33) thin films. *Applied Physics Letters* **96,** 22102-22102–3 (2010).

[73] Batista, C., Ribeiro, R. M. & Teixeira, V. Synthesis and characterization of VO_2-based thermochromic thin films for energy-efficient windows. *Nanoscale research letters* **6,** 1–7 (2011).

[74] Brown, B. L., Lee, M., Clem, P. G., Nordquist, C. D., Jordan, T. S., Wolfley, S. L., Leonhardt, D., Edney, C. & Custer, J. A. Electrical and optical characterization of the metal-insulator transition temperature in Cr-doped VO_2 thin films. *Journal of Applied Physics* **113,** 173704-173704–4 (2013).

[75] Israelsson, M. & Kihlborg, L. The phase relations in the VO_2|WO2 system. *Materials Research Bulletin* **5,** 19–29 (1970).

[76] Takami, H., Kanki, T., Ueda, S., Kobayashi, K. & Tanaka, H. Electronic Structure of W-Doped VO_2 Thin Films with Giant Metal–Insulator Transition Investigated by Hard X-ray Core-Level Photoemission Spectroscopy. *Applied Physics Express* **3,** 63201 (2010).

[77] Aetukuri, N. B., Gray, A. X., Drouard, M., Cossale, M., Gao, L., Reid, A. H., Kukreja, R., Ohldag, H., Jenkins, C. A., Arenholz, E., Roche, K. P., Dürr, H. A., Samant, M. G. & Parkin, S. S. P. Control of the metal-insulator transition in vanadium dioxide by modifying orbital occupancy. *Nature Physics* **9,** 661–666 (2013).

[78] Lee, J. S., Shibuya, K., Kawasaki, M. & Tokura, Y. Optical investigation of metal-insulator transitions in $V_{1-x}W_xO_2$ ($0 \le x \le 0.33$). *Physical Review B* **85,** 155110 (2012).

[79] Patridge, C. J., Whittaker, L., Ravel, B. & Banerjee, S. Elucidating the Influence of Local Structure Perturbations on the Metal–Insulator Transitions of V1–xMoxO2

Nanowires: Mechanistic Insights from an X-ray Absorption Spectroscopy Study. *The Journal of Physical Chemistry C* **116,** 3728–3736 (2012).

[80] Tang, C., Georgopoulos, P., Fine, M. E., Cohen, J. B., Nygren, M., Knapp, G. S. & Aldred, A. Local atomic and electronic arrangements in W_{x}V_{1-x}O_{2}. *Physical Review B* **31,** 1000–1011 (1985).

[81] Burkhardt, W., Christmann, T., Franke, S., Kriegseis, W., Meister, D., Meyer, B. K., Niessner, W., Schalch, D. & Scharmann, A. Tungsten and fluorine co-doping of VO_2 films. *Thin Solid Films* **402,** 226–231 (2002).

[82] Rakotoniaina, J. C., Mokrani-Tamellin, R., Gavarri, J. R., Vacquier, G., Casalot, A. & Calvarin, G. The Thermochromic Vanadium Dioxide: I. Role of Stresses and Substitution on Switching Properties. *Journal of Solid State Chemistry* **103,** 81–94 (1993).

[83] Shannon, R. D. Revised effective ionic radii and systematic studies of interatomic distances in halides and chalcogenides. *Acta Crystallographica Section A* **32,** 751–767 (1976).

[84] Kwok, H. S. Formation of atomic beams and dynamics of in situ superconducting film growth by pulsed-laser deposition. *Thin Solid Films* **218,** 277–290 (1992).

[85] Kim, H., Charipar, N., Osofsky, M., Qadri, S. B. & Piqué, A. Optimization of the semiconductor-metal transition in VO_2 epitaxial thin films as a function of oxygen growth pressure. *Applied Physics Letters* **104,** 81913 (2014).

[86] Nagashima, K., Yanagida, T., Tanaka, H. & Kawai, T. Influence of ambient atmosphere on metal-insulator transition of strained vanadium dioxide ultrathin films. *Journal of Applied Physics* **100,** 63714-63714–4 (2006).

[87] Lafane, S., Kerdja, T., Abdelli-Messaci, S., Khereddine, Y., Kechouane, M. & Nemraoui, O. Correlation of plume dynamics and oxygen pressure with VO_2 stoichiometry during pulsed laser deposition. *Applied Physics A* **112,** 159–164 (2012).

[88] Canulescu, S., Papadopoulou, E. L., Anglos, D., Lippert, T., Schneider, C. W. & Wokaun, A. Mechanisms of the laser plume expansion during the ablation of LiMn2O4. *Journal of Applied Physics* **105,** 63107 (2009).

[89] Esposito, M., Bator, M., Döbeli, M., Lippert, T., Schneider, C. W. & Wokaun, A. Negative ions: The overlooked species in thin film growth by pulsed laser deposition. *Applied Physics Letters* **99,** 191501-191501–3 (2011).

[90] Packwood, D. M., Shiraki, S. & Hitosugi, T. Effects of Atomic Collisions on the Stoichiometry of Thin Films Prepared by Pulsed Laser Deposition. *Physical Review Letters* **111,** 36101 (2013).

[91] Rosevear, W. H. & Paul, W. Hall Effect in VO_{2} near the Semiconductor-to-Metal Transition. *Physical Review B* **7,** 2109–2111 (1973).

[92] Fu, D., Liu, K., Tao, T., Lo, K., Cheng, C., Liu, B., Zhang, R., Bechtel, H. A. & Wu, J. Comprehensive study of the metal-insulator transition in pulsed laser deposited epitaxial VO_2 thin films. *Journal of Applied Physics* **113,** 43707-43707–7 (2013).

[93] Jin, P., Nakao, S. & Tanemura, S. Tungsten doping into vanadium dioxide thermochromic films by high-energy ion implantation and thermal annealing. *Thin Solid Films* **324,** 151–158 (1998).

[94] Hörlin, T., Niklewski, T. & Nygren, M. Electrical and magnetic properties of V1−xWxO2, 0 ≤ x ≤ 0.060. *Materials Research Bulletin* **7,** 1515–1524 (1972).

[95] Whittaker, L., Wu, T.-L., Stabile, A., Sambandamurthy, G. & Banerjee, S. Single-Nanowire Raman Microprobe Studies of Doping-, Temperature-, and Voltage-Induced Metal–Insulator Transitions of WxV1–xO2 Nanowires. *ACS Nano* **5,** 8861–8867 (2011).

[96] Takami, H., Kawatani, K., Kanki, T. & Tanaka, H. High Temperature-Coefficient of Resistance at Room Temperature in W-Doped VO_2 Thin Films on Al_2O_3 Substrate and Their Thickness Dependence. *Japanese Journal of Applied Physics* **50,** 55804 (2011).

[97] Wu, Z. P., Miyashita, A., Yamamoto, S., Abe, H., Nashiyama, I., Narumi, K. & Naramoto, H. Molybdenum substitutional doping and its effects on phase transition properties in single crystalline vanadium dioxide thin film. *Journal of Applied Physics* **86,** 5311–5313 (1999).

[98] Fisher, B. Electrical and seebeck effect measurements in Nb doped VO_2. *Journal of Physics and Chemistry of Solids* **43,** 205–211 (1982).

[99] Strelcov, E., Tselev, A., Ivanov, I., Budai, J. D., Zhang, J., Tischler, J. Z., Kravchenko, I., Kalinin, S. V. & Kolmakov, A. Doping-Based Stabilization of the M2 Phase in Free-Standing VO_2 Nanostructures at Room Temperature. *Nano Letters* **12,** 6198–6205 (2012).

[100] Cheng, C., Liu, K., Xiang, B., Suh, J. & Wu, J. Ultra-long, free-standing, single-crystalline vanadium dioxide micro/nanowires grown by simple thermal evaporation. *Applied Physics Letters* **100,** 103111-103111–4 (2012).

[101] Tselev, A., Meunier, V., Strelcov, E., Shelton, W. A., Luk'yanchuk, I. A., Jones, K., Proksch, R., Kolmakov, A. & Kalinin, S. V. Mesoscopic Metal−Insulator Transition at Ferroelastic Domain Walls in VO_2. *ACS Nano* **4,** 4412–4419 (2010).

[102] Kim, P., Shi, L., Majumdar, A. & McEuen, P. L. Thermal Transport Measurements of Individual Multiwalled Nanotubes. *Physical Review Letters* **87,** 215502 (2001).

[103] Fan, W., Cao, J., Seidel, J., Gu, Y., Yim, J. W., Barrett, C., Yu, K. M., Ji, J., Ramesh, R., Chen, L. Q. & Wu, J. Large kinetic asymmetry in the metal-insulator transition nucleated at localized and extended defects. *Physical Review B* **83,** (2011).

[104] Li, S., Zhang, K., Yang, J.-M., Lin, L. & Yang, H. Single Quantum Dots as Local Temperature Markers. *Nano Letters* **7,** 3102–3105 (2007).

[105] Wienken, C. J., Baaske, P., Rothbauer, U., Braun, D. & Duhr, S. Protein-binding assays in biological liquids using microscale thermophoresis. *Nature Communications* **1,** 100 (2010).

[106] Guiton, B. S., Gu, Q., Prieto, A. L., Gudiksen, M. S. & Park, H. Single-Crystalline Vanadium Dioxide Nanowires with Rectangular Cross Sections. *Journal of the American Chemical Society* **127,** 498–499 (2005).

[107] Orman, J. A. V. & Crispin, K. L. Diffusion in Oxides. *Reviews in Mineralogy and Geochemistry* **72,** 757–825 (2010).

[108] Johnson, O. W. One-Dimensional Diffusion of Li in Rutile. *Physical Review* **136,** A284–A290 (1964).

[109] Steele, J. L. & Mccartney, E. R. Anisotropy of Diffusion in Rutile. *Nature* **222,** 79–79 (1969).

[110] Gurvitch, M., Luryi, S., Polyakov, A. & Shabalov, A. Nonhysteretic behavior inside the hysteresis loop of VO[sub 2] and its possible application in infrared imaging. *Journal of Applied Physics* **106,** 104504 (2009).

[111] Niklaus, F., Vieider, C. & Jakobsen, H. MEMS-based uncooled infrared bolometer arrays: a review. in *Proceedings of the SPIE* **6836,** 68360D–68360D–15 (2007).

[112] Kang, H. K., Han, Y. H., Shin, H. J., Moon, S. & Kim, T. H. Enhanced infrared detection characteristics of VOx films prepared using alternating V2O5 and V layers. *Journal of Vacuum Science & Technology B* **21,** 1027–1031 (2003).

[113] Wang, B., Lai, J., Zhao, E., Hu, H., Liu, Q. & Chen, S. Vanadium oxide microbolometer with gold black absorbing layer. *Optical Engineering* **51,** 74003–1 (2012).

[114] Radford, W. A., Murphy, D. F., Ray, M., Propst, S. H., Kennedy, A., Kojiro, J. K., Woolaway II, J. T., Soch, K. L., Coda, R., Lung, G., Moody, E. A., Gleichman, D. & Baur, S. T. 320 x 240 silicon microbolometer uncooled IR FPAs with on-chip offset correction. in *Proceedings of the SPIE* **2746,** 82–92 (1996).

[115] Cheng, Q., Paradis, S., Bui, T. & Almasri, M. Design of Dual-Band Uncooled Infrared Microbolometer. *IEEE Sensors Journal* **11,** 167–175 (2011).

[116] Gurvitch, M., Luryi, S., Polyakov, A., Shabalov, A., Dudley, M., Wang, G., Ge, S. & Yakovlev, V. VO_2 films with strong semiconductor to metal phase transition prepared by the precursor oxidation process. *Journal of Applied Physics* **102,** 33504-33504–13 (2007).

[117] Soltani, M., Chaker, M., Haddad, E., Kruzelecky, R. & Margot, J. Micro-optical switch device based on semiconductor-to-metallic phase transition characteristics of W-doped VO_2 smart coatings. *Journal of Vacuum Science & Technology A* **25,** 971–975 (2007).

[118] Kruse, P. W. Can the 300-K radiating background noise limit be attained by uncooled thermal imagers? in *Proceedings of the SPIE* **5406,** 437–446 (2004).

[119] Coath, J. A. & Richardson, M. A. Optical properties of vanadium dioxide films on suitable infrared transmitting substrates. in *Proceedings of the SPIE* **3738,** 554–559 (1999).

[120] Kats, M. A., Sharma, D., Lin, J., Genevet, P., Blanchard, R., Yang, Z., Qazilbash, M. M., Basov, D. N., Ramanathan, S. & Capasso, F. Ultra-thin perfect absorber employing a tunable phase change material. *Applied Physics Letters* **101,** 221101 (2012).

[121] Wang, K., Cheng, C., Cardona, E., Guan, J., Liu, K. & Wu, J. Performance Limits of Microactuation with Vanadium Dioxide as a Solid Engine. *ACS Nano* **7,** 2266–2272 (2013).

[122] Mirfakhrai, T., Madden, J. D. W. & Baughman, R. H. Polymer artificial muscles. *Materials Today* **10,** 30–38 (2007).

[123] Liu, K., Fu, D., Cao, J., Suh, J., Wang, K. X., Cheng, C., Ogletree, D. F., Guo, H., Sengupta, S., Khan, A., Yeung, C. W., Salahuddin, S., Deshmukh, M. M. & Wu, J. Dense Electron System from Gate-Controlled Surface Metal–Insulator Transition. *Nano Letters* **12,** 6272–6277 (2012).

[124] Nakano, M., Shibuya, K., Okuyama, D., Hatano, T., Ono, S., Kawasaki, M., Iwasa, Y. & Tokura, Y. Collective bulk carrier delocalization driven by electrostatic surface charge accumulation. *Nature* **487,** 459–462 (2012).

[125] Koehler, J. S. Diffusion of Lattice Defects in a Stress Field. *Physical Review* **181,** 1015–1019 (1969).

[126] Schwartz, M. W. & Mukherjee, A. K. The migration of point defects in crack tip stress fields. *Materials Science and Engineering* **13,** 175–179 (1974).

[127] Nygren, E., Aziz, M. J., Turnbull, D., Poate, J. M., Jacobson, D. C. & Hull, R. Pressure dependence of arsenic diffusivity in silicon. *Applied Physics Letters* **47,** 105–107 (1985).

[128] Halicioglu, T. & Barnett, D. M. Formation and migration energies of interstitials in silicon under strain conditions. *Surface Science* **441,** 265–269 (1999).

[129] Nabarro, F. R. N. Steady-state diffusional creep. *Philosophical Magazine* **16,** 231–237 (1967).

[130] Borg, R. J. & Dienes, G. J. in *An Introduction to Solid State Diffusion* 255–286 (Academic Press, 1988).

[131] Philpot, K. A., Ikuma, Y., Miller, G. R. & Gordon, R. S. High temperature steady-state creep of polycrystalline rutile, pure and doped with tantalum. *Journal of Materials Science* **18,** 1698–1708 (1983).

[132] Hahn, H. & Averback, R. S. Low-Temperature Creep of Nanocrystalline Titanium(IV) Oxide. *Journal of the American Ceramic Society* **74,** 2918–2921 (1991).

[133] Cheng, G., Miao, C., Qin, Q., Li, J., Xu, F., Haftbaradaran, H., Dickey, E. C., Gao, H. & Zhu, Y. Large anelasticity and associated energy dissipation in single-crystalline nanowires. *Nature Nanotechnology* **10,** 687–691 (2015).

[134] Völkl, J. The Gorsky effect. *Berichte der Bunsengesellschaft für physikalische Chemie* **76,** 797–805 (1972).

[135] Appavoo, K., Lei, D. Y., Sonnefraud, Y., Wang, B., Pantelides, S. T., Maier, S. A. & Haglund, R. F. Role of Defects in the Phase Transition of VO_2 Nanoparticles Probed by Plasmon Resonance Spectroscopy. *Nano Letters* **12,** 780–786 (2012).

[136] Mellan, T. A. & Grau-Crespo, R. Density functional theory study of rutile VO_2 surfaces. *The Journal of Chemical Physics* **137,** 154706-154706–8 (2012).

[137] Cheng, B. L., Button, T. W., Gabbay, M., Fantozzi, G. & Maglione, M. Oxygen Vacancy Relaxation and Domain Wall Hysteresis Motion in Cobalt-Doped Barium Titanate Ceramics. *Journal of the American Ceramic Society* **88,** 907–911 (2005).

[138] Goncalves-Ferreira, L., Redfern, S. A. T., Artacho, E., Salje, E. & Lee, W. T. Trapping of oxygen vacancies in the twin walls of perovskite. *Physical Review B* **81,** 24109 (2010).

[139] Lee, S., Liu, Z.-K., Kim, M.-H. & Randall, C. A. Influence of nonstoichiometry on ferroelectric phase transition in BaTiO3. *Journal of Applied Physics* **101,** 54119 (2007).

[140] Warren, W. L., Dimos, D., Tuttle, B. A. & Smyth, D. M. Electronic and Ionic Trapping at Domain Walls in BaTiO3. *Journal of the American Ceramic Society* **77,** 2753–2757 (1994).

[141] Hedvall, J. A. Changes in Crystal Structure and Their Influence on the Reactivity and Catalytic Effect of Solids. *Chemical Reviews* **15,** 139–168 (1934).

[142] Cohn, G. & Hedvall, J. A. The influence of the transition from ferromagnetism to paramagnetism on catalytic activity. *The Journal of Physical Chemistry* **46,** 841–847 (1942).

[143] Ramachandran, V. S. & Sereda, P. J. Hedvall Effect in Cement Chemistry. *Nature* **233,** 134–135 (1971).

[144] Garn, P. D. & Habash, T. S. Solid state reactions. A rigorous test of the Hedvall effect. *The Journal of Physical Chemistry* **83,** 229–231 (1979).

[145] Thompson, R. A. Hedvall Effect in Cement Chemistry. *Nature* **240,** 119–119 (1972).

[146] Wu, J., Walukiewicz, W., Yu, K. M., Shan, W., Ager, J. W., Haller, E. E., Lu, H., Schaff, W. J., Metzger, W. K. & Kurtz, S. Superior radiation resistance of $In_{1-x}Ga_xN$ alloys: Full-solar-spectrum photovoltaic material system. *Journal of Applied Physics* **94,** 6477–6482 (2003).

[147] Messenger, S. R., Burke, E. A., Summers, G. P., Xapsos, M. A., Walters, R. J., Jackson, E. M. & Weaver, B. D. Nonionizing energy loss (NIEL) for heavy ions. *IEEE Transactions on Nuclear Science* **46,** 1595–1602 (1999).

[148] Ramirez, J. G., Saerbeck, T., Wang, S., Trastoy, J., Malnou, M., Lesueur, J., Crocombette, J.-P., Villegas, J. E. & Schuller, I. K. Effect of disorder on the metal-insulator transition of vanadium oxides: Local versus global effects. *Physical Review B* **91,** 205123 (2015).

[149] Thomas, B. S., Marks, N. A., Corrales, L. R. & Devanathan, R. Threshold displacement energies in rutile TiO2: A molecular dynamics simulation study. *Nuclear Instruments and Methods in Physics Research Section B: Beam Interactions with Materials and Atoms* **239,** 191–201 (2005).

[150] Robinson, M., Marks, N. A., Whittle, K. R. & Lumpkin, G. R. Systematic calculation of threshold displacement energies: Case study in rutile. *Physical Review B* **85,** 104105 (2012).

[151] Janotti, A. & Van de Walle, C. G. Native point defects in ZnO. *Physical Review B* **76,** 165202 (2007).

[152] Tuomisto, F., Saarinen, K., Look, D. C. & Farlow, G. C. Introduction and recovery of point defects in electron-irradiated ZnO. *Physical Review B* **72,** 85206 (2005).

[153] Okada, M., Nakagawa, M., Atobe, K. & Kawabata, Y. Defects in TiO2 crystals produced by neutron irradiations at 20 K. *Nuclear Instruments and Methods in Physics Research Section B: Beam Interactions with Materials and Atoms* **91,** 359–361 (1994).

[154] Sawatari, H., Iguchi, E. & Tilley, R. J. D. Formation energies of point defects in rutile (TiO2). *Journal of Physics and Chemistry of Solids* **43,** 1147–1155 (1982).

[155] Deák, P., Aradi, B. & Frauenheim, T. Oxygen deficiency in TiO_2: Similarities and differences between the Ti self-interstitial and the O vacancy in bulk rutile and anatase. *Physical Review B* **92,** 45204 (2015).

[156] Yu, N. & Halley, J. W. Electronic structure of point defects in rutile TiO_2. *Physical Review B* **51,** 4768–4776 (1995).

[157] Corbel, C., Stucky, M., Hautojärvi, P., Saarinen, K. & Moser, P. Positron-annihilation spectroscopy of native vacancies in as-grown GaAs. *Physical Review B* **38,** 8192–8208 (1988).

[158] Omling, P., Weber, E. R., Montelius, L., Alexander, H. & Michel, J. Electrical properties of dislocations and point defects in plastically deformed silicon. *Physical Review B* **32,** 6571–6581 (1985).

[159] Smith, H. M., Phillips, D. J., Sharp, I. D., Beeman, J. W., Chrzan, D. C., Haegel, N. M., Haller, E. E., Ciampi, G., Kim, H. & Shah, K. S. Electronic effects of Se and Pb dopants in TlBr. *Applied Physics Letters* **100,** 202102-202102–4 (2012).

[160] Willardson, R.K., Weber, Eicke R., Christofides, Constantinos & Ghibaudo, Gerard. *Effect of Disorder and Defects in Ion-Implanted Semiconductors: Optical and Photothermal Characterization*. (Academic Press, 1997).

[161] Jeong, J., Aetukuri, N., Graf, T., Schladt, T. D., Samant, M. G. & Parkin, S. S. P. Suppression of Metal-Insulator Transition in VO_2 by Electric Field–Induced Oxygen Vacancy Formation. *Science* **339,** 1402–1405 (2013).

[162] Wu, Z. P., Yamamoto, S., Miyashita, A., Zhang, Z. J., Narumi, K. & Naramoto, H. Single-crystalline epitaxy and twinned structure of vanadium dioxide thin film on (0001) sapphire. *Journal of Physics: Condensed Matter* **10,** L765 (1998).

[163] Picraux, S. T., Davies, J. A., Eriksson, L., Johansson, N. G. E. & Mayer, J. W. Channeling Studies in Diamond-Type Lattices. *Physical Review* **180,** 873–882 (1969).

[164] Walukiewicz, W. Amphoteric native defects in semiconductors. *Applied Physics Letters* **54,** 2094–2096 (1989).

[165] Walukiewicz, W. Mechanism of Fermi-level stabilization in semiconductors. *Physical Review B* **37,** 4760–4763 (1988).

[166] Li, S. X., Haller, E. E., Yu, K. M., Walukiewicz, W., Ager, J. W., Wu, J., Shan, W., Lu, H. & Schaff, W. J. Effect of native defects on optical properties of InxGa1−xN alloys. *Applied Physics Letters* **87,** 161905-161905–3 (2005).

[167] Li, S. X., Yu, K. M., Wu, J., Jones, R. E., Walukiewicz, W., Ager, J. W., Shan, W., Haller, E. E., Lu, H. & Schaff, W. J. Fermi-level stabilization energy in group III nitrides. *Physical Review B* **71,** 161201 (2005).

[168] Hsu, L., Jones, R. E., Li, S. X., Yu, K. M. & Walukiewicz, W. Electron mobility in InN and III-N alloys. *Journal of Applied Physics* **102,** 73705-73705–6 (2007).

[169] Finetti, M., Galloni, R. & Mazzone, A. M. Influence of impurities and crystalline defects on electron mobility in heavily doped silicon. *Journal of Applied Physics* **50,** 1381–1385 (1979).

[170] Yamaguchi, T., Taylor, S. J., Watanabe, S., Ando, K., Yamaguchi, M., Hisamatsu, T. & Matsuda, S. Explanation for carrier removal and type conversion in irradiated silicon solar cells. *Applied Physics Letters* **72,** 1226–1228 (1998).

[171] Detert, D. M., Tom, K. B., Battaglia, C., Denlinger, J. D., Lim, S. H. N., Javey, A., Anders, A., Dubon, O. D., Yu, K. M. & Walukiewicz, W. Fermi level stabilization and band edge energies in CdxZn1−xO alloys. *Journal of Applied Physics* **115,** 233708 (2014).

[172] Suh, J., Fu, D., Liu, X., Furdyna, J. K., Yu, K. M., Walukiewicz, W. & Wu, J. Fermi-level stabilization in the topological insulators Bi_2Se_3 and Bi_2Te_3: Origin of the surface electron gas. *Physical Review B* **89,** 115307 (2014).

[173] Yu, K. M. N-type doping of InGaN by high energy particle irradiation. *physica status solidi (a)* **206,** 1168–1175 (2009).

[174] McCluskey, M. D. & Haller, E. E. *Dopants and Defects in Semiconductors*. (CRC Press, 2012).

[175] Yu, P. Y. & Cardona, M. in *Fundamentals of Semiconductors* 159–202 (Springer Berlin Heidelberg, 2010).

[176] Look, D. C., Hemsky, J. W. & Sizelove, J. R. Residual Native Shallow Donor in ZnO. *Physical Review Letters* **82,** 2552–2555 (1999).

[177] Reurings, F., Rauch, C., Tuomisto, F., Jones, R. E., Yu, K. M., Walukiewicz, W. & Schaff, W. J. Defect redistribution in postirradiation rapid-thermal-annealed InN. *Physical Review B* **82,** 153202 (2010).

[178] Signorello, G., Karg, S., Björk, M. T., Gotsmann, B. & Riel, H. Tuning the Light Emission from GaAs Nanowires over 290 meV with Uniaxial Strain. *Nano Letters* **13,** 917–924 (2013).

[179] Jones, R. E., Yu, K. M., Li, S. X., Walukiewicz, W., Ager, J. W., Haller, E. E., Lu, H. & Schaff, W. J. Evidence for p-Type Doping of InN. *Physical Review Letters* **96,** 125505 (2006).

[180] Zhang, C. & Xing, D. Miniaturized PCR chips for nucleic acid amplification and analysis: latest advances and future trends. *Nucleic Acids Research* **35,** 4223–4237 (2007).

[181] Tesmer, J. R. & Nastasi, M. A. *Handbook of modern ion beam materials analysis*. (Materials Research Society, 1995).

[182] Feldman, L. C., Mayer, J. W. & Picraux, S. T. *Materials analysis by ion channeling: submicron crystallography*. (Academic Press, 1982).

[183] Yu, K. M., Walukiewicz, W., Wojtowicz, T., Kuryliszyn, I., Liu, X., Sasaki, Y. & Furdyna, J. K. Effect of the location of Mn sites in ferromagnetic Ga_{1-x}Mn_{x}As on its Curie temperature. *Physical Review B* **65,** 201303 (2002).

[184] Wong, F. J., Zhou, Y. & Ramanathan, S. Epitaxial variants of VO_2 thin films on complex oxide single crystal substrates with 3m surface symmetry. *Journal of Crystal Growth* **364,** 74–80 (2013).

[185] Fan, L. L., Wu, Y. F., Si, C., Pan, G. Q., Zou, C. W. & Wu, Z. Y. Synchrotron radiation study of VO_2 crystal film epitaxial growth on sapphire substrate with intrinsic multi-domains. *Applied Physics Letters* **102,** 11604-11604–4 (2013).